APPLIED AND EXTENDED MODELING OF OPTICAL INTERFERENCE EFFECTS TOWARDS SUM FREQUENCY GENERATION IN MULTILAYER THIN FILMS

A dissertation submitted to the faculty of the graduate school of the University of Minnesota by

Thorn Dramstad

In partial fulfillment of the requirements for the degree of Doctor of Philosophy

Aaron M. Massari, Advisor

October, 2021

ACKNOWLEDGEMENTS

Aaron, you have gone beyond the role of advisor. Your patient support, your pointed advice, your calm ambiance, and your genuine care have guided, composed, and shaped me. You accepted a student wanting to change things up, and try out this new field, and you taught me how to succeed in it. Thank you, Dr. Massari, for providing me with the resources and support to grow in the field of physical chemistry. Your example of ingenuity, initiative, and empathy have left a resounding mark with me. Let me organize your desktop.

I would like to extend thanks to the members of the Massari Group for all their support and time given answering countless questions. Isaac, you provided indispensable training. Your patience and responsiveness were requisite to my endless enquiries. Cindy, Courtney, Joel, Zhihao, Connor, and Grace, I thank you for all the conversations you provided, many with the shared goal of distraction from fruitless hours on the laser.

I would also like to acknowledge the Chemistry Department at the University of Minnesota. The many professors and faculty I have encountered during my tenure here have given me the knowledge and desire I need to succeed in my chosen field through class and conversation.

Finally, to Brittany. My warm embrace, my bright smile, my open ear, and my spicy tuna. I'm so grateful I've been able to stand next to your during this journey. Your love and faith were integral to my endeavors. Thank you for your patience, your laughter, and all the rides you've given me in the rain. A person has never been as lucky in finding a wife so amazing, kind, and beautiful.

ABSTRACT

Sum frequency generation is a powerful technique to elucidate the molecular order and orientation of interfacial molecules where a bulk media typically prevents characterization. Additionally, optical interference effects further complicate analysis of the sum frequency response as constructive and destructive interference alter the intensity of the measured signal. Quantitative assignment of the interfacial molecules requires an accounting of the optical properties of the films to solve the present interference. Performance of this analysis requires a modeling routine. Current routines struggle with performance issues including slow functionality and a lack of user friendliness. Within this work, construction of a novel fitting routine is documented. The routine uses transfer matrix formalism to describe the optical propagation of light throughout the relevant thin film systems. It is applied to resolve interfacial questions for prototypical electronic materials.

In the first chapter, the modeling is used to determine the packing of interfacial molecules as the thickness of the vibrationally active material is varied. In the second, I studied a system with a temperature-dependent packing structure. Following, the model is extended to explore the refractive indices: both their value and treatment. In Chapter 4, I offer a novel perspective by leveraging the optical inferences in a sum frequency generation experiment to solve the refractive indices, as the descriptive transfer matrix formalism is highly dependent on the complex terms. Finally, the description of the material boundary is explored, ranging from distinct to continuous, and the effects on the sum frequency signal are demonstrated in Chapter 5.

TABLE OF CONTENTS

LIST OF TABLES

LIST OF TABLES (CONT.)

LIST OF FIGURES

LIST OF FIGURES (CONT.)

LIST OF FIGURES (CONT.)

LIST OF ABBREVIATIONS

6T – α-sexithiophene

AFM – atomic force microscopy

ATR – attenuated total reflectance

BBO - β-barium borate

BP – bulk phase

DFG – difference frequency generation

DFT – density functional theory

FTIR – Fourier transformed infrared

FWHM – full width at half max

HT – high temperature

HWHM – half width at half max

IR – infrared

LT – low temperature

Nd:YAG – neodymium-doped yttrium aluminum garnet

Nd:YLF – neodymium-doped yttrium lithium fluoride

Nd:YVO4 – neodymium-doped yttrium vanadate

OFET – organic field effect transistor

OPA – optical parametric amplification

PTCDI –N,N′-dioctyl-3,4,9,10-perylenedicarboximide

QCM – quartz crystal microbalance

RMS – root mean squared

SAM – self assembled monolayer

SFG – sum frequency generation

SHG – sum harmonic generation

TF – thin film

TFP – thin film phase

Ti:Sapph – titanium sapphire

VASE – variable angle spectroscopic ellipsometry

VSFG – vibrational sum frequency generation

XRD – x-ray diffraction

CHAPTER 1: INTRODUCTION

1.1. Sum Frequency Generation

Within a stratified thin film sample there exist numerous interfaces bounded between bulk media. A perennial challenge with analysis is the separation of bulk and interfacial signals. Typical vibrational-sensing non-contact spectroscopies such as Fourier transformed infrared (FTIR) and Raman spectroscopies sample the entirety of the material, where the bulk signal is dominant. Sum frequency generation (SFG) was developed as a second-order nonlinear spectroscopic technique capable of interface-specific vibrational measurements. This capable tool offers the ability resolve quantitative information about molecular order, orientation, composition, and attributes of the two-dimensional boundaries, both at surface and buried locations within stratified thin-film systems.

The advent of sum frequency generation came shortly following the operation of the first ruby rod laser,[1] when Bloembergen and Pershan finalized a comprehensive description of sum frequency generation in 1962.[2] This theoretical basis extensively covered the dipolar contributions that satisfy Maxwell's equations in a number of systems. Following this work the development of reliable high powered lasers afforded construction of the first vibrational sum frequency generation (VSFG) spectroscopy system in 1987 by Yuen-Ron Shen at Berkeley.[3] This pioneering work in the development of optical second harmonic generation (SHG) and VSFG has since branched out to cover a breadth of topics. VSFG has been applied to biological interfaces,[4] aqueous

phase solutions,[5] and electrochemical interfaces.[6] Dynamic phase materials like liquid crystals have also gained interest from the community.[7-9] Other interesting technologies have also been extensively studied, such as catalysts,[10] semiconductors,[11-13] nanoparticles,[14] and polymers.[15] Additionally, SFG has been extended to measure electronic spectra at interfaces,[16] along with the coupling of electronic and vibrational modes.[17] The growth of the field has been assisted by advances in data processing and further description and understanding of the surface and bulk processes occurring. This thesis serves to introduce work completed in VSFG modeling and extensions of the theory to solve novel applications, such as solution of the refractive indices. Understanding of the basic theory is hence requisite and will be introduced.

1.2. Sum Frequency Theory

The sum frequency wave mixing process occurs upon the synchronous irradiation of a bounded nonlinear media with two photons. In the special case where the photons are equal in energy, SHG will occur. Upon admixing of the photons, a third at the sum frequency of the two incident sources will be emitted:

$$\omega_1 + \omega_2 = \omega_{\mathrm{SF}} \tag{1}$$

where, for a vibrational sum frequency experiment, ω_1 and ω_2 are frequencies within the visible and infrared (IR) region.[18-19] The IR excitation induces a vibrational polarization, which is followed by a typically nonresonant upconverting vibrational pulse.[20] Perturbation of a medium by an electric field, under the electric dipole approximation, exerts a force on the valence electrons leading to an induced electric dipole, which is

expanded through a power series when the impingent field is high in intensity, such as that output by a laser:

$$\mu = \mu_0 + \alpha \mathrm{E} + \beta \mathrm{E}^2 + \gamma \mathrm{E}^3 + \cdots . \tag{2}$$

The terms α, β, and γ respectively represent the first, second, and third order molecular polarizabilities, while E is the oscillating electric field.[19, 21] By extension to the macroscopic system, the induced polarization is then:

$$\mathrm{P}(t) = \varepsilon_0 (\chi^{(1)} \mathrm{E}(t) + \chi^{(2)} \big(\mathrm{E}(t)\big)^2 + \chi^{(3)} \big(\mathrm{E}(t)\big)^3 + \cdots) , \tag{3}$$

where $\chi^{(n)}$ are the n^{th} order susceptibilities, which are n+1 ranked tensors, and ε_0 is the vacuum permittivity.[21] Substitution of E with the two incident fields in the VSFG experiment leads to:

$$\mathrm{P}(t)^{(2)} = \varepsilon_0 \chi^{(2)} (\mathrm{E}_{\mathrm{IR}} \cos(\omega_{\mathrm{IR}}) \mathrm{t} + \mathrm{E}_{\mathrm{vis}} \cos(\omega_{\mathrm{vis}}) t)^2 , \tag{4}$$

when only the second-order term is considered. While removal of higher order terms is a simplification of sum frequency generation, quadrupole terms are not considered within this work. For their effects within a sum frequency experiment, the following sources are recommended.[22-24] Equation 4 can be distributed into the following terms:

$$\begin{aligned} \mathrm{P}^{(2)}(t) = \varepsilon_0 \chi^{(2)} [& \mathrm{E}_{\mathrm{IR}}^2 e^{-2i\omega_{\mathrm{IR}} t} \ldots \\ & + \mathrm{E}_{\mathrm{vis}}^2 e^{-2i\omega_{\mathrm{vis}} t} \ldots \\ & + 2\mathrm{E}_{\mathrm{IR}} \mathrm{E}_{\mathrm{vis}} e^{-i(\omega_{\mathrm{IR}} + \omega_{\mathrm{vis}}) t} \ldots \\ & + 2\mathrm{E}_{\mathrm{IR}} \mathrm{E}_{\mathrm{vis}}^* e^{-i(\omega_{\mathrm{IR}} - \omega_{\mathrm{vis}}) t}] \ldots \\ & + [\mathrm{E}_{\mathrm{IR}}^2 + \mathrm{E}_{\mathrm{vis}}^2] \end{aligned} \tag{5}$$

where the first two terms represents the SHG doubling of the respective incident sources, the third yields the sum frequency response, the fourth gives the difference frequency response (DFG), and the final term gives rise to a static DC field.[21]

Let us now consider the symmetry limits of SFG. A third-rank tensor such as $\chi^{(2)}$ has 3^3 individual elements, which in the *xyz* plane are given by all 27 possible combinations of the axes for the three beams. In any centrosymmetric media the indices are beholden to a center of inversion, such that

$$\chi_{ijk}^{(2)} = \chi_{-i-j-k}^{(2)}. \tag{6}$$

If this inversion transformation is applied to the bulk molecular polarization, the simplified form of equation 4 then becomes

$$-\mathrm{P}^{(2)}(t) = \varepsilon_0 \chi_{-i-j-k}^{(2)} (-\mathrm{E}(t))^2, \tag{7}$$

of which the induced polarization can be replaced by its original form, yielding

$$-\varepsilon_0 \chi_{ijk}^{(2)} (\mathrm{E}(t))^2 = \varepsilon_0 \chi_{-i-j-k}^{(2)} (-\mathrm{E}(t))^2. \tag{8}$$

Simplification of equation 8 imparts a final equation, which can immediately be seen to be at odds with equation 6:

$$-\chi_{ijk}^{(2)} = \chi_{-i-j-k}^{(2)}. \tag{9}$$

Thus, for both equations to hold true all three unique terms must equal zero. It is now clear that for any centrosymmetric system, all possible SFG tensor elements will be zero, providing no interfacial response.[21]

Extending the application to the fundamental noncentrosymmetric point group, C_∞, yields further insight. Consider a right circular cylinder atop a substrate defined by the Cartesian plane, where the *x* and *y* directions are aligned with the polar axes of the cylinder, and are hence equivalent, and the substrate-orthogonal *z* axis intersects the longitudinal axis. While inversion of either the *x* or *y* axis provides an identical result, the presence of the substrate prevents equality upon inversion of the *z* axis. Inspection of the 27 unique $\chi^{(2)}_{ijk}$ terms with these inversions reveals the nonzero terms.

For example, taking $\chi^{(2)}_{xyx}$ and inverting it to, $\chi^{(2)}_{-x-y-x}$, yields an equivalent response to $\chi^{(2)}_{xyx}$. Therefore this term must be zero. Conversely, treatment of $\chi^{(2)}_{xzx}$ yields no such requirement, since $\chi^{(2)}_{-x-z-x} \neq \chi^{(2)}_{xzx}$, so the term may generate an SFG response. Within the confines of C_∞ symmetry there is a reduction in the available elements to seven terms: $\chi^{(2)}_{xxz}$, $\chi^{(2)}_{xzx}$, $\chi^{(2)}_{zxx}$, $\chi^{(2)}_{yyz}$, $\chi^{(2)}_{yzy}$, $\chi^{(2)}_{zyy}$, and $\chi^{(2)}_{zzz}$. However, since the *x* and *y* axes are identical, a 90° rotation of the coordinate plane further reduces the unique nonzero terms to $\chi^{(2)}_{xxz} = \chi^{(2)}_{yyz}$, $\chi^{(2)}_{xzx} = \chi^{(2)}_{yzx}$, $\chi^{(2)}_{zxx} = \chi^{(2)}_{zyy}$, and $\chi^{(2)}_{zzz}$. However, sampling within the experimental frame is not considered on a Cartesian axis, but instead is referenced through the polarization frame, defining the oscillations of transverse light waves traveling in the *xz* plane as parallel (*s*) to the fixed surface, i.e. substrate (shown in gray in Figure 1), or completely contained within the *xz* plane (*p*).

Translation from one frame to the next is completed using a Jones vector, J:

$$\vec{e}^{\omega} = \begin{bmatrix} E_p \\ E_s \end{bmatrix}^{\omega} = J \cdot \begin{bmatrix} E_x \\ E_y \\ E_z \end{bmatrix}^{\omega} \tag{10}$$

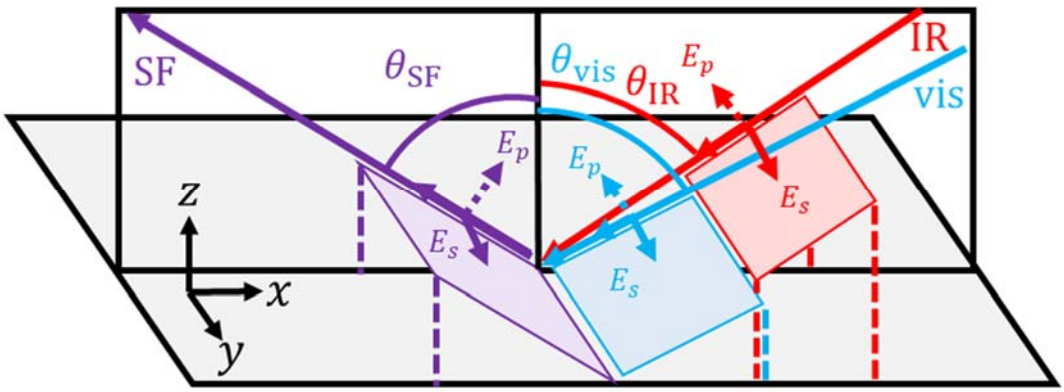

Figure 1. Representation of incident and output beams in a sum frequency experiment in the Cartesian frame with polarized components for reflection geometry.

where the electric field Jones vector ($\vec{e}^{\omega}$) for a given frequency (ω can reference any incident or sum frequency) can also be described by the individual directional components in the Cartesian plane. Likewise, for the nonlinear susceptibility term,

$$\chi_{ijk}^{(2)} \cdot J = \chi_{J}^{(2)}. \tag{11}$$

The transformation matrix is given by the following:

$$J = \begin{bmatrix} \pm cos\theta^{\omega_{sum}} & 0 & sin\theta^{\omega_{sum}} \\ 0 & 1 & 0 \end{bmatrix} \tag{12}$$

where, for the incident sources the first element is positive, and for the sum frequency output the sign is positive (negative) for transmission (reflection). While the Jones frame describes purely polarized light, a simple transform provides the Stokes vector, which can describe purely or partially polarized light.[25] The stokes vector, $\vec{s}^{\omega}$, is directly related through the following relation:

$$\vec{s}^{\omega} = A \cdot \left(\vec{e}^{\omega^*} \otimes \vec{e}^{\omega}\right). \tag{13}$$

The Kronecker product is represented by $\otimes$ and the transformation matrix to transition between the frames is

$$A = \begin{bmatrix} 1 & 0 & 0 & 1 \\ 1 & 0 & 0 & -1 \\ 0 & 1 & 1 & 0 \\ 0 & i & -i & 0 \end{bmatrix}. \tag{14}$$

Application of the Jones vector to the nonzero elements listed above for the cylindrical case affords differentiation through experiment. As each of the three beams in an SFG experiment can either be *s* or *p* polarized there are 2^3 individual scalar entries for the total $\chi^{(2)}$ response: $\chi^{(2)}_{sss}$, $\chi^{(2)}_{ssp}$, $\chi^{(2)}_{sps}$, $\chi^{(2)}_{pss}$, $\chi^{(2)}_{spp}$, $\chi^{(2)}_{pps}$, $\chi^{(2)}_{psp}$, and $\chi^{(2)}_{ppp}$. Using equation 11 these can be related back to the 7 nonzero elements:

$$\chi^{(2)}_{ssp} = \chi^{(2)}_{yyz}, \tag{15a}$$

$$\chi^{(2)}_{sps} = \chi^{(2)}_{yzy}, \tag{15b}$$

$$\chi^{(2)}_{pss} = \chi^{(2)}_{zyy}, \tag{15c}$$

$$\chi^{(2)}_{ppp} = \chi^{(2)}_{xxz} + \chi^{(2)}_{xzx} + \chi^{(2)}_{zxx} + \chi^{(2)}_{zzz}. \tag{15d}$$

It is perhaps worth noting that the above only takes into consideration the seven achiral terms. There are six additional chiral terms where $i \neq j \neq k$. These are typically treated separately, however, achiral interfacial molecules are capable of forming structures with chiral orientation. Discussion of unified treatment can be found elsewhere.[26] For the C_{∞} point group, where the *x* and *y* axis are reducible, one can see that $\chi^{(2)}_{ppp}$ contains contribution from all nonzero elements. If the axes are made unique, such as through a C_{2v} point group molecule like water where the *z* axis intersects only the oxygen atom and

all molecules are contained within the *xz* plane, then e.g. $\chi^{(2)}_{xxz} \neq \chi^{(2)}_{yyz}$ and each tensor in the polarization frame will have no relation to the others.

1.3. Propagation of Light

The previous section documents the nonlinear susceptibility of the sum frequency response. In addition, careful attention must be given to the light sources. In the simplest experiment, a single interface exists at which the sum frequency response is generated in

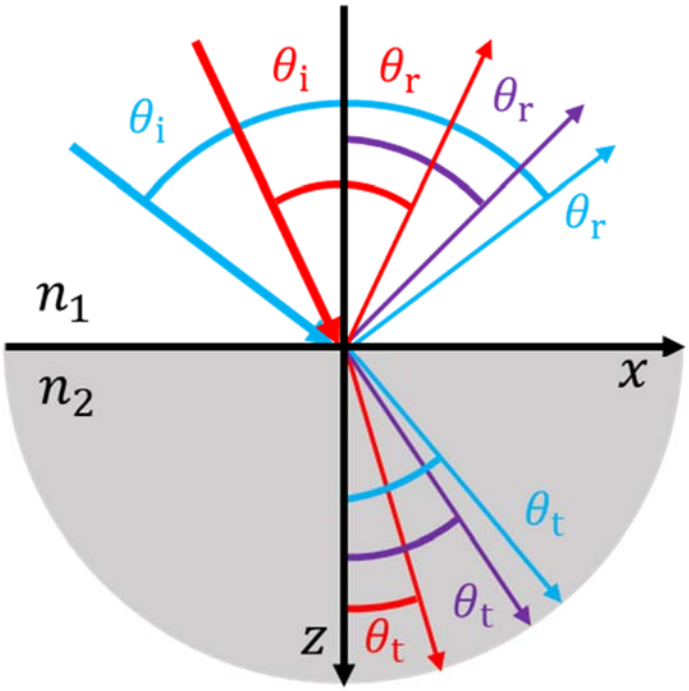

Figure 2. Incident, reflected, and transmitted light for a visible (blue) and IR (red) source generating a sum frequency response (purple) in the reflected and transmitted direction at the interface formed by materials 1 and 2 with unique refractive indices.

both directions (Figure 2). There are several results depicted in Figure 2 requiring definition. For a source incident at the angle θ_i, the angle of reflection, θ_r, or transmission, θ_t, is given by Snell's law:

$$n_1 \sin\theta_{\mathrm{i}} = n_1 \sin\theta_r = n_2 \sin\theta_t. \tag{16}$$

One can see that the reflection angle is identical to the incident angle. The refractive index of each material is given by n. It is important to note that the refractive index of a material is complex and wavelength dependent, describing the phase velocity, $\bar{n}$, and attenuation, k, or extinction coefficient, of a light source in a medium:

$$n_\omega = \bar{n}_\omega + ik_\omega. \tag{17}$$

The indices are important intrinsic properties related to the molecular dipole moments of the media. They can be commonly altered through changes in composition, temperature, and pressure,[27-28] and are of upmost importance in the understanding of optical propagation. Leveraging the indices affords application across a range of fields, from reflective and antireflective optical coatings, to eyeglasses, to forensic material identification.

The real and imaginary terms are related using a Kramers-Kronig transformation:

$$\bar{n}_\omega = 1 + \frac{2}{\pi}\,\mathrm{p.v.}\int_0^{+\infty} \frac{\omega' \kappa(\omega')}{\omega'^{,2} - \omega^2}\,\mathrm{d}\omega' \tag{18}$$

where p. v. is the Cauchy principle value, which addresses the problem that arises as $\omega \rightarrow \omega'$ by removing the interval around the resultant pole from the integration, instead using

the width limit of the interval approaching zero.[28-30] The Kramers-Kronig relationship can also be used to perform the reverse of the transformation[29]:

$$\kappa_\omega = -\frac{2}{\pi}\,\mathrm{p.v.}\int_0^{+\infty} \frac{\omega'(\bar{n}(\omega')-1)}{\omega'^{,2}-\omega^2}\,\mathrm{d}\omega'. \tag{19}$$

If the full range of integration is not available, as will be discussed in later chapters, then an offset must be added to account for absorption outside the spectral range.

Returning to Figure 2, for the system given; there will be a reflected and transmitted sum frequency response. The angle of the given response is found using the phase matching criteria,

$$n_{\mathrm{SF}}(\omega_{\mathrm{vis}}+\omega_{\mathrm{IR}})\sin\theta_{\mathrm{SF}} = n_{\mathrm{vis}}\omega_{\mathrm{vis}}\sin\theta_{\mathrm{vis}} \pm n_{\mathrm{IR}}\omega_{\mathrm{IR}}\sin\theta_{\mathrm{IR}} \tag{20}$$

which is dependent on the refractive indices of the relevant materials each beam propagates through and the angle of the incident beams normal to the interface. The positive (negative) sign references beams propagating in the same (opposite) directions along the *x* coordinate.

Finally, as light encounters a boundary, the mismatch in the adjacent refractive indices causes partial reflection and transmission of the incident source. In Figure 1, the arbitrary intensity of a given secondary beam is shown by the thickness of the vector. The total reflectance (R) defines the fraction of light reflected from a system and is related to the transmittance (T) for a specific polarization (given as an intensity term):

$$T = 1 - R. \tag{21}$$

For the complex amplitude coefficients, which are polarization-dependent, the Fresnel

reflection and transmission terms are[31]:

$$r_s = \frac{n_1\cos\theta_\mathrm{i} - n_2\cos\theta_\mathrm{t}}{n_1\cos\theta_\mathrm{i} + n_2\cos\theta_\mathrm{t}}, \tag{22a}$$

$$r_p = \frac{n_2\cos\theta_\mathrm{i} - n_1\cos\theta_\mathrm{t}}{n_2\cos\theta_\mathrm{i} + n_1\cos\theta_\mathrm{t}}, \tag{22b}$$

$$t_s = \frac{2n_1\cos\theta_\mathrm{i}}{n_1\cos\theta_\mathrm{i} + n_2\cos\theta_\mathrm{t}}, \tag{22c}$$

$$t_p = \frac{2n_1\cos\theta_\mathrm{i}}{n_2\cos\theta_\mathrm{i} + n_1\cos\theta_\mathrm{t}}. \tag{22d}$$

While the fractional components in the *s* polarized convention are simple to reconcile, the *p* polarized terms require an additional term to reach unity:

$$1 = t_s - r_s = \frac{n_2}{n_1}t_p + r_p. \tag{23}$$

Either polarization can then be related back to the total reflectance and transmittance by

$$R = |r|^2, \tag{24a}$$

$$T = \frac{n_2\cos\theta_\mathrm{t}}{n_1\cos\theta_i}|t|^2. \tag{24b}$$

Next let us consider a two interface system (Figure 3). As the fractionally transmitted internal beam encounters the second interface, it is again subject to the Fresnel-described propagation. Each subsequent internal source follows suit. This leads to an infinite series of internal reflections that will each accumulate a phase shift, ϕ, which is dependent on the angle, wavelength, and thickness, d, of the relevant layer, v:

$$\phi_v = \frac{2\pi d_v}{\lambda}n_v\cos\theta_v. \tag{25}$$

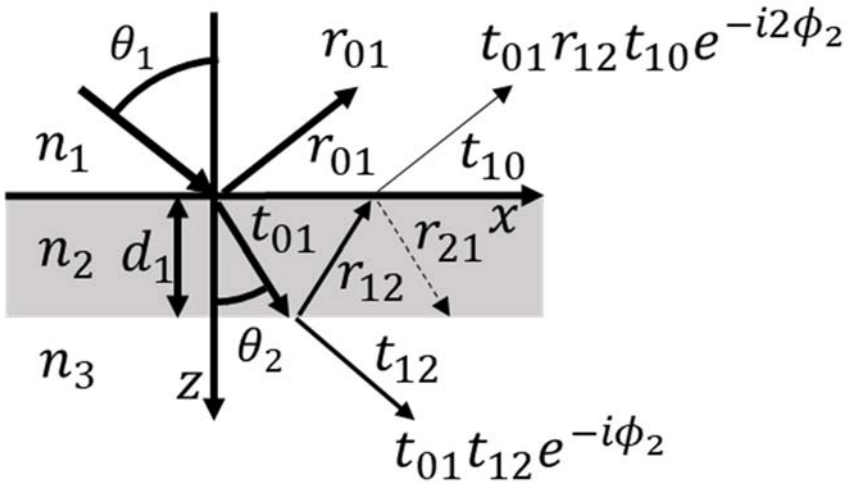

Figure 3. Propagation of light through a two interface system with fractional reflections and transmissions, where the terms for the measured output beams are given in both geometries.

For a thin film sample, where the thickness is smaller than the coherence length, L_c, presented by:

$$L_c = \frac{\lambda^2}{2\pi\Delta\lambda}, \tag{26}$$

where $\Delta\lambda$ is the spectral resolution of the detector, optical interference effects will be generated.[32] For the shorter wavelength visible and sum frequency pulses, L_c is typically greater than a micron, while for the longer IR pulse, it exceeds hundreds of microns. As the wavelength of the impinging beam decreases, the impact of the interferences will inversely increase. Observation of this phenomena has been modeled for a sum frequency experiment.[22]

Assuming thicknesses smaller than the coherence length, the measured reflectance and transmittance are now more complicated than for the single interface system (equation 24) as each now contains an infinite number of terms, and is further convoluted as more layers are added. This creates a computational dilemma requiring an approximation. Solution is of the upmost importance, as multilayer thin films have great prevalence in technology. Solar cells, transistors, and displays amongst others utilize stratified designs in operation.[33-34] In devices requiring optical input, like a solar cell, the intensity of the light reaching the solar absorber is dependent on the geometry of the material layers, which can incur optical losses due to reflection and interference. Prediction and modeling of these systems is hence important to the tuning and optimization of the operational technologies. In an SFG experiment, quantitative analysis of the output sum frequency response requires description of the interferences. In ellipsometry, the thickness and refractive indices are modeled in order to define the relevant layer system and propagation of light throughout it.

Towards a description of light propagating through a system, approaches have included the usage of amplitude ratios to determine changes in susceptibility,[11] experimental separation of layers,[35-37] and partial transfer matrix methods.[38-39] A well-known approach to this solution is the use of full transfer matrix formalism to reduce the problem to a single boundary.[12, 40] Using this formalism requires a flat, homogenous, and isotropic interface. Transfer matrix formalism is used for the solution of Maxwell's equations for light either incident on the system, or outbound in the case of a sum frequency signal. To demonstrate the impact of the interferences on the resultant sum frequency intensity signal, Figure 4 shows the change in the SFG signal intensity as the

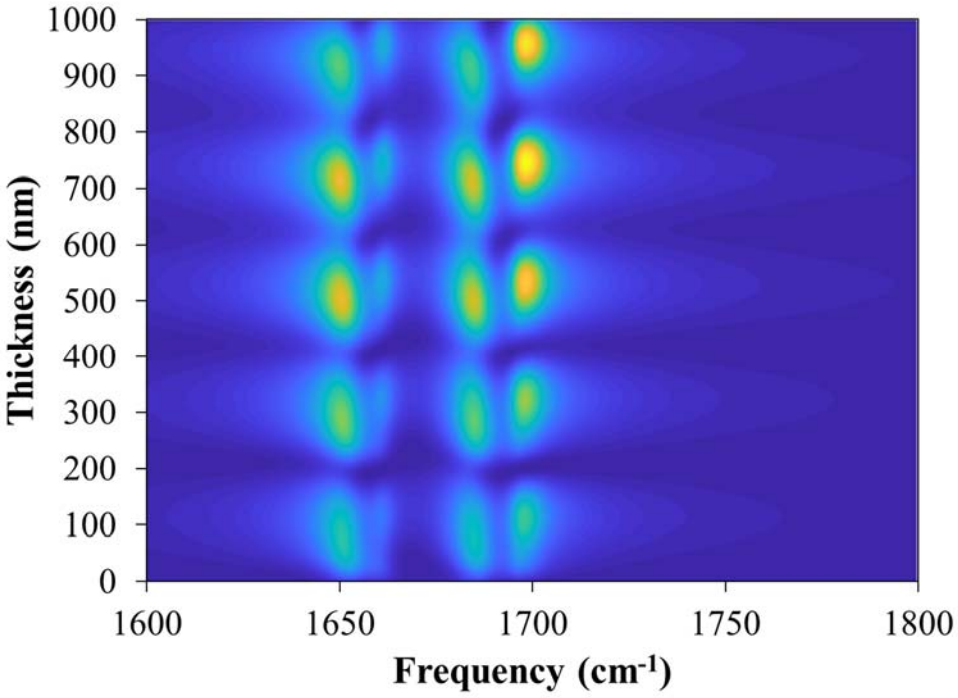

Figure 4. VSFG response as the organic layer thickness is varied.

thickness of an active organic layer deposited overtop a thermal oxide layer all on a silicon substrate for a typical vibrational response (see Chapter 4 for more information on the system). Within the simulation, the sum frequency response is held constant, so the observable oscillations shown in Figure 4 are directly resultant from the change to the phase (equation 25), which changes the optical interferences for each parameter-varied calculation. This demonstrates the necessity of a modeling routine before quantitative assignment can be confidently made.

For the employment of transfer matrix formalism toward a sum frequency experiment let us consider a multilayer thin film where only a single interfacial layer is

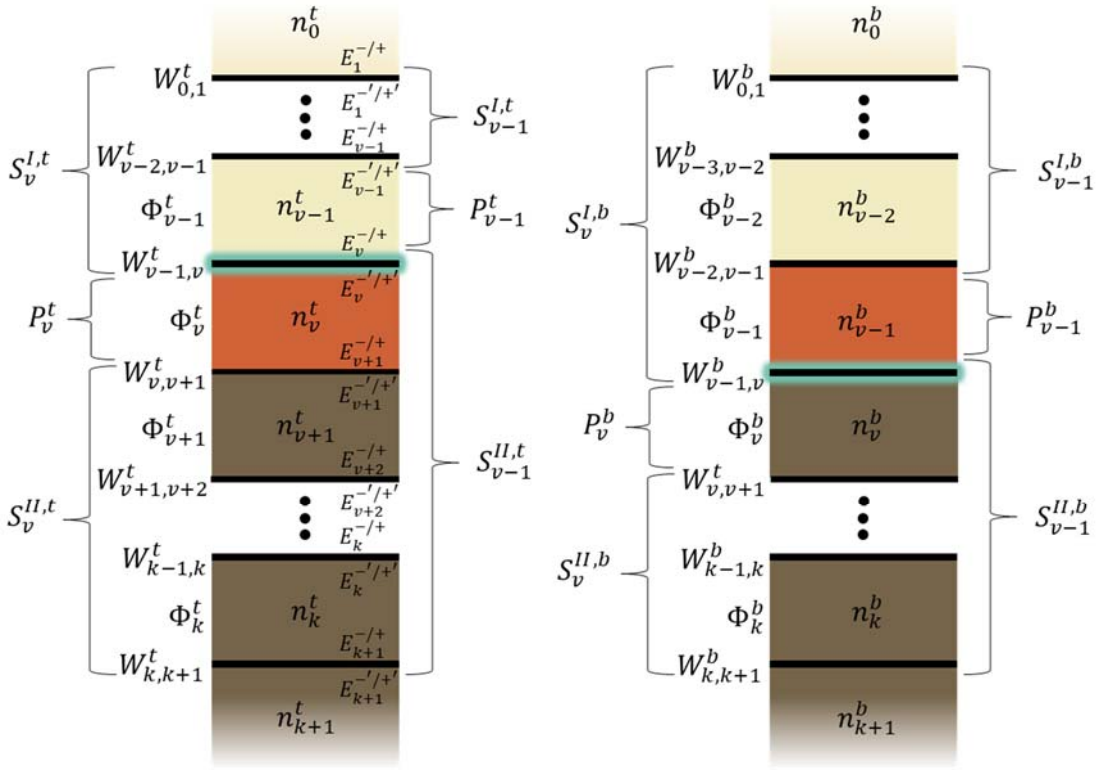

Figure 5. Interfacial definition of the described transfer matrix terms for the top and bottom interfaces of an arbitrary system consisting of a single vibrationally active layer (orange) with a general number of distinct layers above (tan) and below (brown) where the signal enhancing interfaces are highlighted in blue.

vibrationally active (Figure 5). Explanation of the system description will first be considered. The system consists of a number of layers where layer v is vibrationally active. All layers above layer v are numbered in decreasing order until the top external layer into which the incident beams are impingent, layer 0. Below the active layer, the system is additive until the external layer k out of which the signal may be measured in transmission mode. In the same vein, the system, generally described, may be probed

from the k direction and measured in transmission (reflection) mode from the 0 (k) media. When layer v is vibrationally active, resonantly enhancing the sum frequency response, there will be two interfaces where signal generation is relevant, at the top, t, and bottom, b, of the layer, which are delegated into two parts relative to the specific interface, where the individual output signals are simply summed together for the final intensity calculation. Each layer has a complex refractive index, n. The remaining terms are discussed in the following text. Finally, propagation from the k to the 0 media constitutes progression along the positive z axis.

Previous versions of a generalized modeling routine describe the active layer as a single bulk media,[12] though other literature sources have shown a continuity in the refractive indices from one media to the next (for further discussion, see Chapter 5). However, it is worth noting that under the single layer convention $A_v^t = A_{v-1}^b$ which is consistent with the usage adopted in reference 12. This reduction in terms allows for a speed up in the computations, but a separation of the media into interfacial and bulk layers would require an inequality between the terms. Moving forward they will be described as unique. There are two basic matrices generated through this method: refraction and phase.

The refraction matrices, W, are defined for each interface through the following:

$$W_{v-1,v} = \frac{1}{t_{v-1,v}} \begin{bmatrix} 1 & r_{v-1,v} \\ r_{v-1,v} & 1 \end{bmatrix} \tag{27}$$

using the Fresnel reflection and transmission terms, and are dependent on polarization.[12, 40-41] Multiplication of the refraction matrix for a given interface equates the adjacent electric fields directly above the interface to those directly below, denoted by a dash ($'$):

$$\begin{bmatrix} E_v^- \\ E_v^+ \end{bmatrix} = W_{v-1,v} \begin{bmatrix} E_v^{-\prime} \\ E_v^{+\prime} \end{bmatrix}. \tag{28}$$

The $+$ and $-$ symbolism respectively denote positive and negative traveling direction along the z axis. One can see, for an arbitrary interface with a matching refractive index on either side, such as through application of an index-matching fluid or oil immersion in forensic glass analysis, the transmission term resolves to unity, while the reflection terms become 0, thus yielding an identity matrix for W.

In a similar manner, the phase matrix, Φ, is defined using the phase accumulation formula (equation 26)[12, 40-41]:

$$\Phi_v = \begin{bmatrix} e^{-i\phi_v} & 0 \\ 0 & e^{i\phi_v} \end{bmatrix}. \tag{29}$$

Travel through a layer from the immediate underside of the top interface defining it, $E_v^{+/-}$, to the topside of the relative bottom interface $E_{v+1}^{+\prime/-\prime}$, is given by:

$$\begin{bmatrix} E_v^{-\prime} \\ E_v^{+\prime} \end{bmatrix} = \Phi_v \begin{bmatrix} E_{v+1}^- \\ E_{v+1}^+ \end{bmatrix}. \tag{30}$$

In the limit where the layer has zero thickness, Φ_v will become an identity matrix. As shown in Figure 5, the subsystem matrices, defined by S^I for the polarization dependent matrix above the vibrationally active relevant boundary and S^{II} for the subsystem below, are a collection of refraction and phase matrix terms:

$$S_v^I = \left(\prod_{i=0}^{v-2} W_{i,i+1} \Phi_{i+1} \right) W_{v-1,v}, \tag{31a}$$

$$S_v^{II} = \left(\prod_{i=v}^{k-1} W_{i,i+1}\Phi_{i+1}\right) W_{k,k+1}. \tag{31b}$$

Each subsystem is one larger in refraction matrices included than phase, requiring the additional refraction term. These terms can be used to related the electric fields from the external media to layer v:

$$\begin{bmatrix} E_1^- \\ E_1^+ \end{bmatrix} = S_v^I \begin{bmatrix} E_v^{-\prime} \\ E_v^{+\prime} \end{bmatrix}, \tag{32a}$$

$$\begin{bmatrix} E_{v+1}^- \\ E_{v+1}^+ \end{bmatrix} = S_v^{II} \begin{bmatrix} E_{k+1}^{-\prime} \\ E_{k+1}^{+\prime} \end{bmatrix}. \tag{32b}$$

S_{v-1}^I and S_{v-1}^{II} (Figure 5) are calculated in the same fashion. The subsystem terms are used to reduce the effective system to a singularly defined layer both above and below the choice layer, which is layer v when referencing the top interface, and $v+1$ regarding the bottom interface. This packaged reduction allows convenient description through newly defined reflection and transmission coefficients.

The two subsystems can be combined with the intermediary phase matrix to yield the total system transfer term:

$$S = S_v^I \Phi_v S_v^{II} = \left(\prod_{v=0}^{k-1} W_{v,v+1}\Phi_{v+1}\right) W_{k,k+1}. \tag{33}$$

S will be equivalent, whether compiled using v or $v-1$ as the relevant vibrational interface (Figure 5). Using the elements of the system transfer matrix, the reflectance or transmittance (equation 24, complex Fresnel terms given by the internal quantity of the modulus) of an incident beam into the top of the system can be modeled using

$$R_0 = \left|\frac{S_{(21)}}{S_{(11)}}\right|^2, \tag{34a}$$

$$T_0 = \frac{n_0 \cos\theta_0}{n_{k+1}\cos\theta_{k+1}}\left|\frac{1}{S_{(11)}}\right|, \tag{34b}$$

where $S_{(ab)}$ is an element of the total transfer matrix.[12, 40] Likewise, the generality of this approach allows for a beam incident upon the bottom of the sample to be modeled in the same way, where

$$R_{k+1} = \left|-\frac{S_{(12)}}{S_{(11)}}\right|^2, \tag{35a}$$

$$T_{k+1} = \frac{n_0 \cos\theta_0}{n_{k+1}\cos\theta_{k+1}}\left|\frac{|S|}{S_{(11)}}\right|. \tag{35b}$$

Though description of the incident beams can be useful when modeling an experiment such as ellipsometry, sum frequency generation instead requires a two-step process. First, light must be propagated to the relevant boundary, then the generated signal must be transferred back out. For a source incident upon the top of the system, measured in reflection mode, the necessary fractional reflection and transmission terms for the internal input and output sources are then given by[12]:

$$t_{0,I} = \frac{1}{S^I_{v,(11)}}, \tag{36a}$$

$$t_{v,I} = \frac{|S^I_v|}{S^I_{v,(11)}}, \tag{36b}$$

$$r_{v,I} = -\frac{S^I_{v,(12)}}{S^I_{v,(11)}}, \tag{36c}$$

$$r_{v,II} = \frac{S^{II}_{v,(21)}}{S^{II}_{v,(11)}}. \tag{36d}$$

At this point we will consider only the input terms, coming back to the output terms following. The fractional subystem terms from equation 36 are used to define the input internal transfer coefficients, $\tau_{0,v}$, through a geometric series, for a beam incident into the top of the system to the bottom-side of the v interface:

$$\tau^{-'}_{0,v} = \frac{t_{0,I}}{1 - r_{v,I} r_{v,II} \exp(2i\phi_v)}, \tag{37a}$$

$$\tau^{+'}_{0,v} = \tau^{-'}_{0,v} r_{v,II} \exp(2i\phi_v). \tag{37b}$$

These polarization-dependent terms are compiled in a collective matrix, f, for each direction of travel:

$$\tilde{f}^{-'}_{0,v} = \begin{bmatrix} \tau^{-',p}_{0,v} & 0 & 0 \\ 0 & \tau^{-',s}_{0,v} & 0 \\ 0 & 0 & 0 \end{bmatrix}, \tag{38a}$$

$$\tilde{f}^{+'}_{0,v} = \begin{bmatrix} \tau^{+',p}_{0,v} & 0 & 0 \\ 0 & \tau^{+',s}_{0,v} & 0 \\ 0 & 0 & 0 \end{bmatrix}. \tag{38b}$$

Finally, two more matrices are necessary. The first approximates the disparity between the interfacial and bulk refractive indices using a modified two phase model.[12] For this matrix, the denominator in the $J_{(33)}$ element is the signal generating interface, while the presence (lack) of the dash indicates reference to the bulk layer below (above) the boundary:

$$J'_v = \begin{bmatrix} 1 & 0 & 0 \\ 0 & 1 & 0 \\ 0 & 0 & \left(\frac{n_v}{\bar{n}_v}\right)^2 \end{bmatrix}. \tag{39}$$

For the general model, we will assume the interfacial refractive indices are equal to the vibrationally active layer, reducing the problem to a simple two phase model. Reexamination of the interfacial indices will be discussed in Chapter 5. The second final matrix is the required rotational Jones vector relating the Cartesian-listed transfer matrix to the polarization-listed sum frequency intensities:

$$\Pr(\theta_v) = \begin{bmatrix} \cos(\theta_v) & 0 & 0 \\ 0 & 1 & 0 \\ \sin(\theta_v) & 0 & 0 \end{bmatrix}. \tag{40}$$

With all input terms defined, the transfer matrix, $\overleftarrow{T}_{0,v}$, from above the system to interface v, can now be defined, where the left-facing arrow indicates transfer into the system:

$$\overleftarrow{T}_{0,v} = J'_v\left[\Pr(-\theta_v)\,\overleftarrow{f}^{+\prime}_{0,v} + \Pr(\theta_v)\,\overleftarrow{f}^{-\prime}_{0,v}\right]. \tag{41}$$

For the vibrational sum frequency experiment, the input term transfers the IR and visible sources inward.

Next, the necessary output terms will be listed, beginning with the internal transfer coefficients from the relevant boundary to the top of the system:

$$\tau_{v,0}^{+,p/s} = \left(\frac{t_{v-1,\mathrm{I}}^{p/s}\exp(i\phi_{v-1})}{1 - r_{v-1,\mathrm{I}}^{p/s} r_{v-1,\mathrm{II}}^{p/s}\exp(2i\phi_{v-1})}\right), \tag{42a}$$

$$\tau_{v,0}^{-\prime,p/s} = \left(\frac{t_{v,\mathrm{I}}^{p/s} r_{v,\mathrm{II}}^{p/s}\exp(2i\phi_{v})}{1 - r_{v,\mathrm{I}}^{p/s} r_{v,\mathrm{II}}^{p/s}\exp(2i\phi_{v})}\right). \tag{42b}$$

Similar to the input terms, these are culminated into a set of matrices:

$$\vec{f}_{v,0}^{-\prime} = \begin{bmatrix} \tau_{v,0}^{-\prime,p} & 0 & 0 \\ 0 & \tau_{v,0}^{-\prime,s} & 0 \\ 0 & 0 & 0 \end{bmatrix}, \tag{43a}$$

$$\vec{f}_{v,0}^{+} = \begin{bmatrix} \tau_{v,0}^{+,p} & 0 & 0 \\ 0 & \tau_{v,0}^{+,s} & 0 \\ 0 & 0 & 0 \end{bmatrix}. \tag{43b}$$

The projection matrix must be transposed for consistency, yielding:

$$\Pr(\theta_v)^T = \begin{bmatrix} \cos(\theta_v) & 0 & \sin(\theta_v) \\ 0 & 1 & 0 \\ 0 & 0 & 0 \end{bmatrix}. \tag{44}$$

The above are brought together in definition of the nonlinear Fresnel factors, L,[12, 21, 42]

$$L_v^{+} = \left[\Pr(\theta_{v-1})^T + f_{v-1,v}\Pr(-\theta_{v-1})^T\right]J_v', \tag{45a}$$

$$L_v^{-\prime} = \left[\Pr(-\theta_v)^T + f_{v,v-1}\Pr(\theta_v)^T\right]J_v, \tag{45b}$$

which requires an additional set of arrays, defined generally by:

$$f_{i,j} = \begin{bmatrix} r_{i,j}^{p} & 0 & 0 \\ 0 & r_{i,j}^{s} & 0 \\ 0 & 0 & 0 \end{bmatrix}. \tag{46}$$

These are combined to form the directional transfer terms

$$\vec{T}_{v,0}^{+/-\prime} = \vec{f}_{v,0}^{+/-\prime} L_v^{+/-\prime}. \tag{47}$$

For a field radiating from a polarized sheet, the following are necessary factors,

dependent on angle into and refractive indices of the subsequently encountered layer,

$$p_v^{+} = \frac{i2\pi\sec(\theta_{v-1})}{c\lambda n_{v-1}}, \tag{48a}$$

$$p_v^{-\prime} = \frac{i2\pi\sec(\theta_v)}{c\lambda n_v}, \tag{48b}$$

where c is the speed of light.[12, 26] Finally, the output transfer matrices can be defined,

$$\vec{T}_{v,0} = p_v^{+}\vec{T}_{v,0}^{+} + p_v^{-\prime}\vec{T}_{v,0}^{-\prime}, \tag{49}$$

which gives the solution for the sum frequency beams propagating out of the system from both the top, $\vec{T}_{v,0}^{t}$, and bottom, $\vec{T}_{v,0}^{b}$, interfaces (Figure 5).

With the input and output transfer matrices defined, we can now calculate the VSFG intensity terms for the four unique polarization combinations available to a molecule existing in a noncentrosymmetric environment:

$$I_{ssp} = \left[NR + \left(\vec{t}_{v,0,(22)}^{SFG,t}\overleftarrow{t}_{0,v,(22)}^{vis,t}\overleftarrow{t}_{0,v,(31)}^{mIR,t}\right)\chi_{ssp,v}^{(2),t} + \left(\vec{t}_{v,0,(22)}^{SFG,b}\overleftarrow{t}_{0,v,(22)}^{vis,b}\overleftarrow{t}_{0,v,(31)}^{mIR,b}\right)\chi_{ssp,v}^{(2),b}\right]^2, \tag{50a}$$

$$I_{sps} = \left[NR + \left(\vec{t}_{v,0,(22)}^{SFG,t}\overleftarrow{t}_{0,v,(31)}^{vis,t}\overleftarrow{t}_{0,v,(22)}^{mIR,t}\right)\chi_{sps,v}^{(2),t} + \left(\vec{t}_{v,0,(22)}^{SFG,b}\overleftarrow{t}_{0,v,(31)}^{vis,b}\overleftarrow{t}_{0,v,(22)}^{mIR,b}\right)\chi_{sps,v}^{(2),b}\right]^2, \tag{50b}$$

$$I_{pss} = \left[NR + \left(\vec{t}_{v,0,(13)}^{SFG,t}\overleftarrow{t}_{0,v,(22)}^{vis,t}\overleftarrow{t}_{0,v,(22)}^{mIR,t}\right)\chi_{pss,v}^{(2),t} + \left(\vec{t}_{v,0,(13)}^{SFG,b}\overleftarrow{t}_{0,v,(22)}^{vis,b}\overleftarrow{t}_{0,v,(22)}^{mIR,b}\right)\chi_{pss,v}^{(2),b}\right]^2, \tag{50c}$$

$$I_{ppp} = \left[NR + T_{xxz}^{t}\chi_{xxz,v}^{(2),t} + T_{xxz}^{b}\chi_{xxz,v}^{(2),b} + T_{xzx}^{t}\chi_{xzx,v}^{(2),t} + T_{xzx}^{b}\chi_{xzx,v}^{(2),b} + T_{zxx}^{t}\chi_{zxx,v}^{(2),t} + T_{zxx}^{b}\chi_{zxx,v}^{(2),b} + T_{zzz}^{t}\chi_{zzz,v}^{(2),t} + T_{zzz}^{b}\chi_{zzz,v}^{(2),b}\right]^2. \tag{50d}$$

The transfer terms necessary to expand equation 50d are given below:

$$T_{xxz}^{t} = \vec{t}_{v,0,(11)}^{SFG,t}\overleftarrow{t}_{0,v,(11)}^{vis,t}\overleftarrow{t}_{0,v,(31)}^{mIR,t}, \tag{51a}$$

$$T_{xzx}^{t} = \vec{t}_{v,0,(11)}^{SFG,t}\overleftarrow{t}_{0,v,(13)}^{vis,t}\overleftarrow{t}_{0,v,(11)}^{mIR,t}, \tag{51b}$$

$$T^t_{zxx} = \vec{t}^{SFG,t}_{v,0,(13)} \overleftarrow{t}^{vis,t}_{0,v,(11)} \overleftarrow{t}^{mIR,t}_{0,v,(11)}, \tag{51c}$$

$$T^t_{zzz} = \vec{t}^{SFG,t}_{v,0,(13)} \overleftarrow{t}^{vis,t}_{0,v,(31)} \overleftarrow{t}^{mIR,t}_{0,v,(31)}, \tag{51d}$$

where the bottom terms are calculated identically. The resonant response is defined using a sum of Lorentzian line-shapes over n vibrational modes,

$$\chi^{(2)} = \sum\nolimits_n \frac{-A_n}{\omega - \omega_{0,n} - i\Gamma_n}, \tag{52}$$

with an amplitude, A, frequency center, ω_0, and half width at half max of Γ.[18-19, 21] Finally, the nonresonant response is simplified using,

$$NR = \alpha e^{-i\beta}, \tag{53}$$

where α is an amplitude, and β is a phase factor.

1.4. SFG Modeling

In the following chapters, the transfer matrix formalism above will be applied to model and fit VSFG data sets. A persistent challenge when analyzing sum frequency generation is the presence of optical interference effects arising from a stratified thin film system. Experimental approaches have included attempts at reducing the effective signal to a single interface. Careful selection of material thickness can leverage the optical effects to destructively interfere the signal from a single interface.[43] Chemical effects, through the choice of substrate or over-layer,[22] or surface oxidation[44] can yield a similar result. The system can be limited to only a top interface using total internal reflection geometry, or a material thickness for the vibrationally active material exceeding the

sampling depth of the laser. Quantitative confidence can also be improved using a systematic modeling routine.

Previously, groups have applied modeling routines using different methods. Lambert and coworkers first approached the problem by treating the sum frequency response as a superposition of three unique sum frequency sources: the reflected and transmitted sum frequency responses from the top interface (air – dielectric) of an air – dielectric – metal system, and the signal generated from the dielectric – metal interface.[45] To account for internal reflections when few interfaces exist in the system, second generation modeling of the local-fields was achieved using the Airy summation formulation.[46-48] However, use of this system is made difficult upon extension of multilayer films to include a higher number of material layers. Abeles matrix formalism has been employed to solve the interference effects in this regard.[49] Finally, similar to the former, transfer matrix formalism has been taken advantage of to resolve an analytical solution to the local fields.[12, 38, 50-51] The first wide-applicability attempt using the transfer matrix formalism was created in our research group using a series of Mathematica notebook pages that were applicable to any general system with a single layer of vibrationally active material.[12, 43] This system was expanded upon for usage in an electronic SFG experiment using a Matlab routine.[50]

Through the work detailed in this dissertation, a novel sum frequency multilayer thin film fitting routine was developed. Unlike its predecessors, this routine offers an improved runtime, a graphical user interface, and previously unexplored fittable refractive indices, taking advantage of the pervasiveness of the indices throughout each equation defining the transfer matrix formalism. The fitting routine will first be used to

study material systems, elucidating the order and orientation of interfacial molecules as the layer thicknesses (Chapter 2) and deposition temperatures (Chapter 3) were altered over a range of samples. Extensions of the base routine are then explored, first through the aforementioned fittable refractive indices (Chapter 4), then through the separation of the bulk and interfacial refractive indices (Chapter 5). It is well-known that there exists a refractive continuity at the boundaries separating layers, while some material systems are even specifically designed to have a gradual change in the indices. The effects imparted by different system approaches within the model is of relevant interest.

1.5. Laser Setup

In each chapter the necessary laser information for the specific experiments described therein will be supplied, however, in the following section a general overview will be offered. Additional explanation of the optical experimental design can be found at the following literature sources.[11-12] A pictorial representation of the laser system is shown in Figure 6. The subsequently amplified seed pulse is generated through mode locking of a titanium sapphire (Ti:Sapph) oscillator (Model MTS, Kapteyn-Murnane Laboratories). The Ti:Sapph crystal is excited using a 532 nm continuous wave laser (Spectra-Physics, Millennia 5W), where the output of an optical fiber-coupled laser diode is passed through a neodymium-doped yttrium vanadate ($Nd:YVO_4$) to generate continuous wave output at 1064 nm, which is frequency doubled through SHG in a lithium triborate (LBO) crystal. Light amplification by stimulated emission in the oscillator cavity results in a train of output pulses with a full width at half max of ~50 nm

centered at 800 nm, and with a repetition rate of 93 MHz. This output is passed into a chirped pulse amplification system (Spitfire-Pro, Spectra-Physics), where it is stretched, regeneratively amplified, then compressed. The amplification occurs in a Ti:Sapph crystal that is pumped by a neodymium-doped yttrium lithium fluoride (Nd:YLF) laser (Empower, Spectra-Physics), which is itself an intracavity, diode pumped laser, switched by a fused silica acousto-optic modulator. The ultrafast Spitfire output is a ~40 fs pulse with a center at 800 nm, full width at half max of 30 nm, and repetition rate of 1 kHz. The pulse power ranges from 1.1-1.5 mW per pulse.

Half of the resultant power is sent to the VSFG experiment, first directed through an etalon (Fabry-Perot, TecOptics). The etalon is geometrically aligned to constructively transmit two pulses, with centers near 790 and 808 nm and full widths at half max of ~12-15 cm^{-1}.[52] The reflected portion is then sent into an optical parametric amplifier (OPA, OP-800C, Spectra-Physics). The input pulse is split into an amplified signal and idler set using a 3 mm thick β-barium borate (BBO) crystal. The generated signal and idler beams are sent into a $AgGaS_2$ crystal where the DFG process occurs, resulting in emission of mid-IR pulses from 1400-3500 cm^{-1}. Finally, the IR beam is directed through a half wave plate and polarizer before being reflected onto the sample stage. The transmission through the etalon is separated using a dichroic filter, and each pulse is sent through a half wave plate and polarizer. Unique treatment of the individual beams allows for two differently polarized experiments to be run simultaneously. The adjusted visible pulses are then re-overlapped, spatially and temporally, then reflected on the sample stage.

The sum frequency generation spectra were collected in reflection geometry and sent through a polarizer to remove any light polarized opposite of what is being studied. The output was passed through an adjustable slit before entering the spectrometer (1800 g/mm, Acton 2150i, Princeton Instruments) which prepared the beam for transmission into a liquid nitrogen cooled charge coupled detector (Spec-10, Princeton Instruments). System control, including blocking and unblocking of specific beams, as well as background subtraction, was performed using a home-built LabVIEW program. Backgrounds of the visible were collected with the IR beam shuttered off, then subtracted from the aggregate sum frequency response, to account for visible leakage into the detector. References were collected on a strong nonresonant sample (ZnO or Au) lacking resonant enhancement. The vibrational sum frequency signals were divided by the reference, in effect reducing the incident electric fields to a constant value across the relevant frequency range. The global thin film interference model was then used to deconvolute the interfacial signals from the total measured intensity.

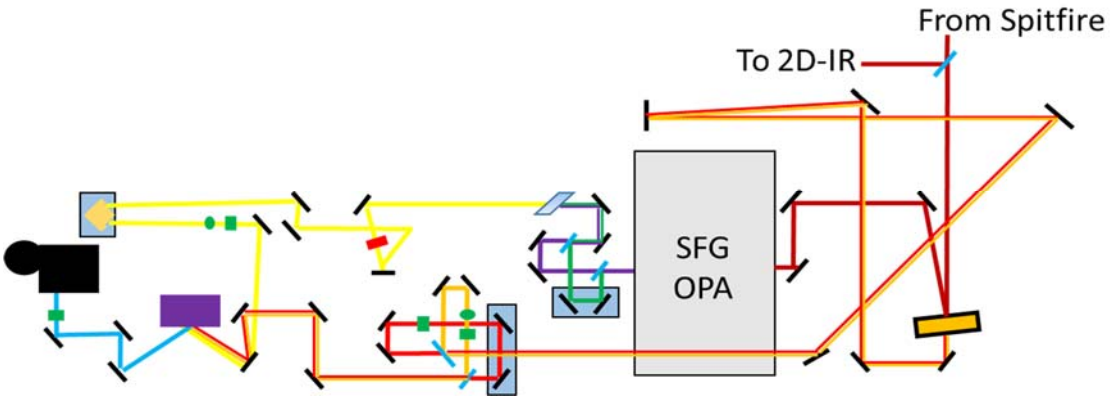

Figure 6. Experimental setup for VSFG spectroscopy system. The orange box with a black outline represents the etalon. The blue boxes with black outlines are movable mount stages. The blue trapezoid is an $AgGaS_2$ crystal. The green ovals are half wave plates, while the green boxes are polarizers. The red box is a collimating lens. The purple box is the sample holder, while the black box and circle are the spectrometer and detector, respectively. The different beams are represented maroon (800 nm), red (790 nm), orange (808 nm), green (signal), purple (idler), yellow (IR), and blue (SFG) lines.

CHAPTER 2: APPLIED MODELING TOWARDS THICKNESS-DEPENDENT PACKING IN SEXITHIOPHENE THIN FILMS

2.1. Introduction

The growth of organic thin films is complex and depends on a number of variables, including deposition rate, substrate temperature, and surface chemistry.[53] In the early stages of film growth, many molecular materials deposit in a less ordered thin-film (TF) phase that is distinct from their crystalline structure, which then converts into a crystalline bulk phase upon reaching a critical thickness.[53-60] Adding yet another layer of complexity, most organic semiconductors exhibit polymorphism and can undergo additional phase transitions between different crystalline structures during the growth process.[54, 56, 61-63] In light of the profound influence of molecular packing and order on the electronic behavior of organic films,[58, 64-67] it is not surprising that such diverse phase behavior leads to challenges in device-to-device reproducibility.

A classic example of this complexity is found in the prototypical organic semiconductor[68] α-sexithiophene (6T). 6T is extraordinarily polymorphic, exhibiting up to four distinct phases during film growth.[63, 67, 69] The most commonly observed phases are the low temperature phase (LT, α phase)[70] and TF phase[67] (β phase), while a high temperature phase (HT)[71] is also observed, where all differ in the number of molecules and relative molecular tilt per unit cell. The LT phase can orient with the long axis either perpendicular or parallel to the substrate surface.[70, 72] Brillante and coworkers showed

that phases can even coexist within the same crystallite.[55, 73] Not surprisingly, 6T film structure is controlled by substrate chemistry[61, 74-76] and deposition settings.[53, 77-78] On substrates with low interaction energies (passivated Si, glass, sapphire, quartz), during early stages of film growth at ambient temperatures, a TF phase forms with islands of 6T on the substrate where the parallel LT phase makes up the inter-island deposition.[67, 79-81] It is generally found that 6T molecules in the TF phase stand perpendicular to the substrate at room temperature or higher,[53, 61] or parallel to the substrate at liquid nitrogen cooled temperatures or on substrates with reactive surfaces.[53, 61, 77-78, 80-81] At temperatures above 100 °C, the TF phase converts to a LT crystalline phase once the film thickness exceeds a few monolayers.[53, 55, 80] However, on room temperature substrates and below, a mixture of disordered TF and LT phases was observed on SiO_2 surfaces, with the TF phase dominating the initial 2-3 monolayers and persisting even for thicker films.[53] Similar studies on glass have shown a structural change beyond 7-8 nm of deposit where lattice strain from the substrate no longer couples to the packing and the formation of the upright LT phase outnumbers the TF phase.[79]

Notably, in the applications for which 6T is of interest, such as organic field effect transistors (OFETs)[66-67, 82-83] and promising performance in organic photovoltaics,[84-85] the interfacial structure is most important. For example, in OFETs the orientation and ordering of 6T in the first 1-2 monolayers is critical to device performance.[82, 86-87] The examples cited above highlight the multidimensional parameter space that must be navigated in order to prepare 6T thin films with reproducible interfacial structure and therefore electronic properties. For this task, it is crucial to use experimental methods that are capable of characterizing the crystalline and non-crystalline structures of 6T at the

buried 6T-substrate interface. VSFG spectroscopy is one technique that can satisfy this requirement.[11, 88-90] In these measurements, an infrared and a visible laser beam are overlapped spatially and temporally at a sample and generate a third coherent beam at the sum of their frequencies.[7, 9, 91] The surface selectivity of this three wave mixing process is dependent upon the second order susceptibility, $\chi^{(2)}$, which vanishes in centrosymmetric media such as the bulk of an isotropic material. However, at material interfaces, inversion symmetry is broken leading to non-zero $\chi^{(2)}$ tensor elements and measurable sum frequency signal. When the IR laser is resonant with a molecular vibration, the interfacial spectrum is enhanced, leading to a VSFG spectrum that tracks the vibrational spectrum of the material but is only generated from material interfaces.

Many of the structural details that exist in the current literature are based on x-ray scattering,[53, 71, 92-93] polarized spectroscopies,[55, 69-70, 75, 94] and atomic force microscopy (AFM),[95-96] none of which is inherently surface specific and all of which respond differently (or exclusively) to crystalline domains. In this current chapter, I use VSFG to monitor molecular orientation at the thin film interfaces of 6T from sub-monolayer to tens of nanometers thick. The aforementioned fitting routine, structured using transfer matrix formalism (Chapter 1) is applied to circumvent the optical interferences arising in a typical measurement where the film thicknesses are less than the coherence length of the probing light. Through these interfacial measurements I was able to test whether phase transitions are indeed experienced between the molecular monolayer at the organic/dielectric and air/organic interfaces, as film growth proceeds. AFM was incorporated to gain complementary information about the topography of the outer interface (air/6T) of the thin film samples.

2.2. Experimental

Materials. 6T and the HPLC grade water used for the RCA cleaning method were used as received from Sigma-Aldrich. Hydrogen peroxide (30%) used in the cleaning procedure was obtained from Fisher Scientific and was stored in a fridge after opening. Ammonium hydroxide (28-30%) was used as received from Macron Chemicals. Hydrochloric acid (36.5-38%) was used as received from BDH Chemicals. Glass slides were purchased from Gold Seal (Cat. No. 3010).

VSFG Sample Preparation. Glass substrates were cleaned using a modified RCA cleaning method prior to organic film deposition, as described previously, resulting in a contaminant-free, hydrophilic surface.[89] 6T deposition was carried out in a home-built high vacuum organic vapor deposition chamber. The substrate holder was mounted above a RADAK I crucible furnace (Luxel Corp). Deposition was performed at an average pressure of 1×10^{-7} Torr, an average sample temperature of 182.3 °C, substrate temperature of 27 °C, and rate of 0.003 nm/s. The low rate was chosen to allow for kinetic stabilization of the deposit. A crucible loaded with 6T was heated until vaporization occurred at which point an automated shutter was engaged to expose the sample. The shutter was then moved back and forth along a 15 mm track, resulting in a sample with an expected gradient and dimensions as depicted in Figure 7. A nominally 60 nm thick region was also deposited at one end of the sample. A different set of individual samples with uniform (non-gradient) thicknesses of 20, 50, and 100 nm were also deposited with the same conditions. Mass deposition was monitored by a calibrated quartz crystal microbalance (QCM) within the deposition chamber.

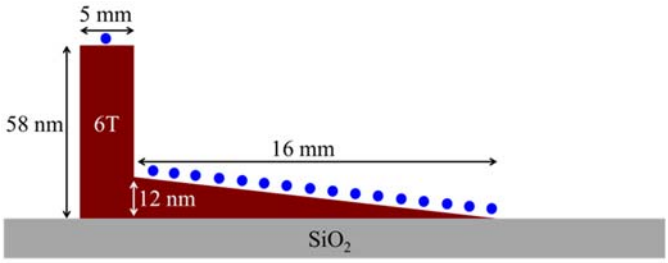

Figure 7. 6T gradient sample deposited on glass substrate. Sixteen spots were measured in 1 mm intervals down the gradient (spot 2-17). Note that drawing is not to scale.

Spectroscopic Ellipsometry. The QCM was calibrated using a set of 6T standards with absolute thicknesses determined by variable angle spectroscopic ellipsometry (VASE, J.A. Woollam Co., Inc) with three angles of incidence (65°, 70°, and 75°) at the University of Minnesota Characterization Facility. A spectral range of 800-1100 nm was measured, and the Cauchy relationship was employed to model the film thickness. Spectroscopic ellipsometry was also used to obtain the real and imaginary optical constants of a 6T thin film on a gold substrate (performed by J. A. Woollam Co., Lincoln, NE). Of note, sample thickness is dependent on molecular orientation, so listed thicknesses may not be precise since deposition was monitored by mass. Hence, thicknesses are rounded to integer values throughout (e.g. 105, 57.5, 47.5, 19.0, and 11.1 nm as measured by QCM; 100, 60, 50, 20, and 11 nm as written).

Atomic Force Microscopy. Topographic imaging was performed on a Bruker Dimension 5000 AFM in the Minnesota Nano Center using tapping mode with the tip driven in the attractive regime. A scan angle of 0°, scan rate of 1 Hz, and scan size of 5 μm × 5 μm was used. Each line scan contained 512 pixels.

Fourier Transform Infrared and Raman Spectroscopy. FTIR spectra were collected on a Thermo-Electron spectrometer (Nicolet 6700) with an average of 16 scans and a resolution of 1.0 cm^{-1}. Raman spectra were collected on a confocal Raman microscope (Witec Alpha300 R) with a UHTS300 spectrometer and DV401 CCD detector at the University of Minnesota Characterization Facility. Prior to sending the data to the detector, the light was collected and focused with a Nikon 100× objective. A diode-pumped neodymium-doped yttrium aluminium garnet (Nd:YAG) solid state laser at 532 nm coupled with an 1800 g/mm grating was used as a light source. The lateral resolution of the instrument was 250 nm and the vertical resolution was 500 nm. The spectral resolution was 0.02 cm^{-1}. Spectra were collected as the average of 10 accumulations with an integration time of 2 seconds each.

VSFG of 6T. The VSFG laser system has been described elsewhere in the literature and above in Chapter 1.[52, 97] The 20, 50, and 100 nm sample VSFG spectra were measured using the experimental apparatus described previously, which separated the visible pulses with a pulse shaper.[97] When measuring the gradient sample the visible pulses were separated using an etalon (Fabry-Perot, TecOptics), as published previously.[52] All spectra had a consistent $\chi^{(2)}$ response after fitting. Briefly, two visible pulses were separated from the laser output with center wavelengths at 790.44 nm and 808.10 nm, each with a full width at half max (FWHM) of 12 cm^{-1}. Using two visible pulses in tandem affords us the ability to run two VSFG experiments in parallel.[97] These were directed to the sample stage at a 50° angle. The mid-IR pulse was centered at 1450 cm^{-1} and directed onto the sample stage at a 60° angle. The sample was attached to a movable sample stage equipped with linear actuators for automated optimization and

experimental movements. A 200 fs time-delay of the visible beams relative to the mid-IR pulse was purposefully induced to facilitate suppression of the non-resonant background.[98-100] Reference spectra from 50 nm of ZnO deposited on glass were collected for two minutes before and after experimentation, averaged, and used to normalize any spectra collected in between to remove fluctuations in beam intensity. Data collection was performed with *ssp* and *sps* polarization combinations simultaneously with fifteen minute integration times and averaged over five frames, where, for example, *ssp* indicates the polarization of the VSFG, visible, and mid-IR beams. Spectra were fit globally to determine the interfacial $\chi^{(2)}$ for each mode by taking into account multilayer interference during propagation of all three beams.[12, 22, 43, 101] For all samples, interface 1 (outer interface) is the air/6T interface and interface 2 (inner interface) is the 6T/glass interface. SiO_2 real and imaginary refractive indices (from 1200 to 1700 cm^{-1}) were obtained by fitting experimental measurements to a polynomial equation.[102]

2.3. Results and Discussion

AFM height imaging was performed along the prepared gradient sample to observe the growth mechanism from a topographical perspective. 6T has been previously reported to grow in a Stranski-Krastanov mechanism on a range of substrates including glass.[79, 96] Prior studies have shown the initial layers of 6T deposit as a wetting layer, upon which island formation begins. The thickness and orientation of this wetting layer varies with growth conditions, such as substrate type,[69, 75, 95-96, 103-104] substrate

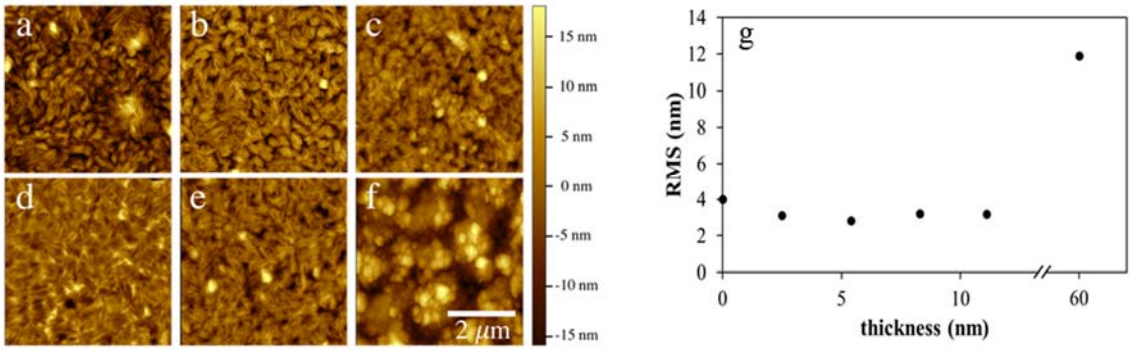

Figure 8. AFM height images (a-f) of 6T deposited on a glass slide at different thicknesses. The scale bar to the right displays relative heights. From left to right, top row (0, 2, and 5 nm) and bottom row (8, 11, and 60 nm). Root-mean-squared (RMS) roughness (g) as measured by AFM for a 1.5 X 1.5 μm square at each thickness along the gradient.

temperature,[61, 75] and deposition rate.[53, 67] Additionally, after the wetting layer reaches a critical thickness and island formation begins, the molecules comprising the wetting layer may reorganize.[69, 80, 105] Figure 8 presents AFM collected over the course of 6T film deposition for the samples studied in this work. Figures 8a – 8d show that there are minor changes in the surface topography – quantitatively the surface roughness stays nearly constant (Figure 8g) – however there is a progressive loss of distinction between the individual surface features present on the glass slide. This is consistent with the growth mechanism described above in which the first molecules wet the glass surface while retaining its topographic features. As the films become nominally thicker, at some critical thickness between 11 (Figure 8e) and 60 nm (Figure 8f) of deposited 6T, large island-like features have formed. Clearly there is a structural change experienced by 6T molecules at

the outer interface, however, the structure of the underlying 6T molecules would be of greater importance if this were to be used as a material in an electronic device. After confirming the expected growth mechanism by topographical changes at the outer interface for 6T in our samples, I then employed interfacial spectroscopic studies to determine molecular structure at the inner and outer interfaces.

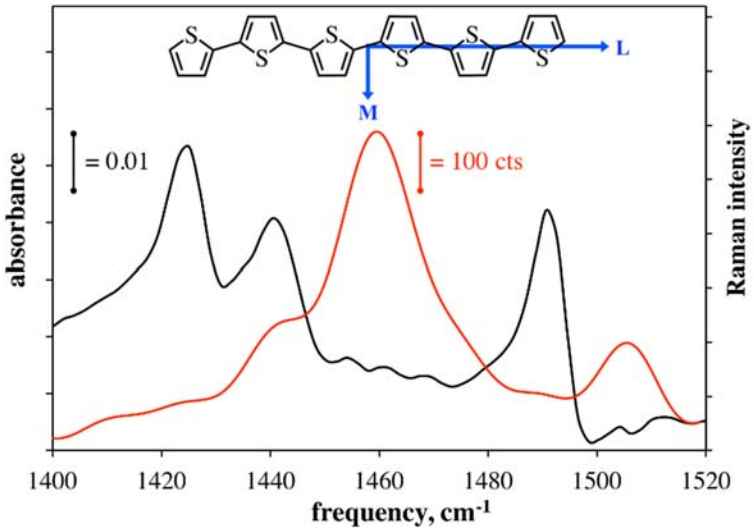

Figure 9. FTIR spectrum of 6T powder (black) and Raman spectrum of a 6T thin film sample on a silicon substrate with native oxide (red). Inset: molecular structure of 6T with arrows indicating transition dipole directions for the M and L modes.

Figure 9 shows the bulk FTIR and Raman spectra of 6T thin films. The FTIR spectrum shows three dominant peaks at 1425, 1440 and 1490 cm^{-1}, which have all been reported previously in the literature.[70, 75, 94] The 1490 cm^{-1} peak was assigned to the C=C asymmetric stretching band and the 1425 and 1460 cm^{-1} peaks to C=C symmetric stretches.[75, 94] Casado and coworkers used DFT to assign the two C=C symmetric

stretching peaks to the inner- and outer-most rings on a 6T oligomer.[106] Lang and coworkers noted that the ratio of these two peaks varied and even inverted for identically prepared samples, suggesting that they may also be sensitive to intermolecular interactions.[75] It has been reported occasionally that a weak peak at ~1455 cm^{-1} appears in the IR absorption spectrum of 6T films;[75, 107] this feature was attributed to molecules at defects and grain boundaries in polycrystalline films.[75] The Raman spectrum shows two peaks centered at 1460 and 1507 cm^{-1}, which have been assigned previously to the symmetric C=C stretch and the C=C asymmetric vibrations, respectively.[55, 70, 75, 94] A small shoulder is also visible near 1440 cm^{-1}, present in literature reports.[70] The peak widths are consistent with other reports on polycrystalline 6T films and have been attributed in part to resonant contributions of distorted molecules at grain boundaries.[70] Polarized FTIR and Raman measurements have shown that the symmetric stretches (FTIR: 1425 and 1440 cm^{-1}, and Raman: 1460 cm^{-1}) are polarized along the short, in-plane molecular axis (M) and the asymmetric stretches (FTIR: 1490 cm^{-1} and Raman: 1507 cm^{-1}) along the molecular long axis (L), as shown inset in Figure 9.[70, 75, 108]

The spectra in Figure 9 demonstrate the bulk vibrational characteristics of 6T. VSFG was implemented to compare these data to the interfacial spectra. VSFG spectra of thin film samples with three thicknesses of 6T on glass substrates were collected in two different polarization combinations (Figure 10). The data in all spectra were fit using multilayer interference to determine the central frequencies and peak shapes of the interfacial vibrational modes. The best fit parameters are shown in Tables 1-2. Due to a lack of signal, the *sps* response for the 11 nm thick sample was not fit.

Table 1. Fitting parameters for the outer and inner $\chi^{(2)}_{ssp}$ responses across all film thicknesses.

Thickness (nm)	Outer amplitude × 10^3	Inner amplitude × 10^3	Outer ν (cm^{-1})	Inner ν (cm^{-1})	Outer Γ (cm^{-1})	Inner Γ (cm^{-1})	Nonresonant amplitude × 10^3	Nonresonant phase
0.3	0.28	0.15	1457.26	1457.24	13.27	14.32	9.2	9.4
1.0	0.68	0.83	1457.14	1457.36	14.02	13.30	4.4	7.1
1.7	0.03	0.27	1457.25	1457.32	15.38	14.20	0.1	6.5
2.5	0.42	0.17	1457.18	1457.31	13.41	14.49	0.1	8.8
3.2	2.09	2.31	1457.32	1457.01	15.46	15.37	0.1	7.0
3.9	0.20	0.47	1457.32	1457.19	16.65	13.91	2.8	7.0
4.7	0.94	1.21	1457.28	1457.07	15.79	15.63	2.3	7.0
5.4	0.14	0.36	1457.23	1457.27	16.87	14.26	1.9	7.0
6.1	0.13	0.35	1457.26	1457.19	15.02	14.80	0.1	7.0
6.8	1.79	0.15	1457.48	1457.51	15.21	14.79	13.8	6.9
7.5	0.47	0.59	1457.21	1457.13	18.34	14.68	4.5	6.9
8.3	0.00	0.32	1457.45	1457.54	17.44	15.49	1.1	7.2
9.0	0.31	0.53	1457.47	1458.16	17.37	14.16	5.6	7.4
9.7	0.75	0.46	1457.42	1458.52	13.86	16.91	7.6	6.5
10.4	0.78	0.56	1457.47	1459.25	14.16	15.74	7.9	9.8
11	0.82	0.49	1457.39	1459.81	14.50	14.50	0.9	8.2
20	0.10	1.73	1457.55	1459.30	16.82	13.74	65.2	7.1
50	0.36	2.01	1457.69	1459.32	13.11	13.62	82.5	5.7
60	0.70	1.05	1457.50	1459.81	15.74	14.79	43.2	6.7
100	0.20	2.71	1457.52	1459.30	13.10	13.02	14.4	6.0

Table 2. Fitting parameters for the outer and inner $\chi^{(2)}_{sps}$ responses for film thicknesses of 20 – 100 nm for the high (1) and low (2) frequency modes.

Thickness (nm)	**20**	**50**	**60**	**100**
Outer (1) amplitude × 10^3	1.06	0.30	0.93	0.73
Outer (2) amplitude × 10^3	0.32	0.20	0.20	0.10
Inner (1) amplitude × 10^3	1.27	0.58	0.34	0.19
Inner (2) amplitude × 10^3	0.21	0.10	0.43	0.11
Outer (1) ν (cm^{-1})	1457.45	1457.51	1457.49	1457.21
Outer (2) ν (cm^{-1})	1422.01	1421.72	1422.06	1421.96
Inner (1) ν (cm^{-1})	1459.54	1459.47	1459.48	1459.46
Inner (2) ν (cm^{-1})	1428.02	1428.12	1428.04	1428.04
Outer (1) Γ (cm^{-1})	15.07	14.88	14.08	10.84
Outer (2) Γ (cm^{-1})	15.27	15.52	14.26	15.53
Inner (1) Γ (cm^{-1})	15.19	14.08	15.31	15.31
Inner (2) Γ (cm^{-1})	15.30	13.94	15.02	15.48
Nonresonant amplitude × 10^3	20.4	29.9	45.1	42.2
Nonresonant phase	6.8	6.8	6.0	5.6

For the 60 nm thick film (Figure 10a) both the *ssp* and *sps* spectra exhibit significant amplitude around 1458 cm^{-1}. As an interface specific technique, VSFG reports selectively on the interfacial vibrational spectrum, which does not always match the bulk FTIR and Raman spectra.[21] Nonetheless, the bulk FTIR and Raman spectra (Figure 9) to confirm the assignments of interfacial spectral features. Building on what has been reported by others,[70, 75] I believe that the higher frequency VSFG activity between 1457–1460 cm^{-1} is due to the C=C symmetric stretch. Unfortunately, there is no VSFG signal near 1490 cm^{-1}. The lack of activity in the asymmetric stretching region is not unprecedented, as our group has previously collected data of 6T on glass in *ppp* geometry,[97] which samples all possible molecular orientations (equation 15d), and observed no amplitude in the area.

The *sps* polarization combination samples the in-plane component of the C=C transition dipole whereas the *ssp* is a measure of the out-of-plane contribution.[21] The fact that the higher frequency symmetric stretching mode shows up in both *ssp* and *sps* polarized VSFG spectra demonstrates that the population of disordered interfacial species have the M molecular axis aligned with some in-plane and some out-of-plane orientation on average. This would be expected for a disordered population. A second lower frequency symmetric C=C peak is present in the *sps* spectrum around 1420 cm^{-1} which is greatly weakened in the *ssp* spectrum. Interpreting the 1420 cm^{-1} vibration as an inner ring M-axis mode,[106] it was concluded that a more ordered population of the interfacial 6T molecules are preferentially oriented with their short axis aligned between parallel and perpendicular to the surface. Overall, this picture is consistent with both end-to-edge (e.g. upright herringbone) and edge-to-face tilted orientations of the molecular long axis,

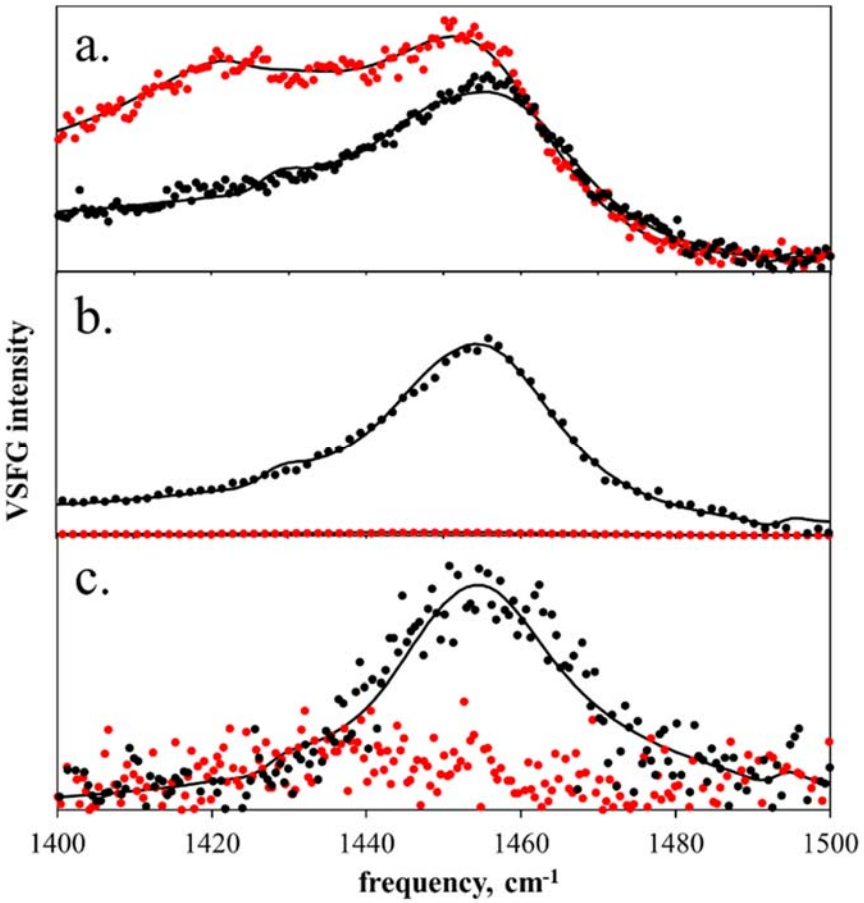

Figure 10. Experimental VSFG spectra of 6T on glass with nominal thicknesses of (a) 60 nm, (b) 20 nm, and (c) 11 nm for the *ssp* (black markers) and *sps* (red markers) polarization combinations at each thickness. Overlaid solid lines on each data set show the best fitted spectra to the data taking into account multilayer interference.

which could be differentiated by studying the L-axis modes of 6T. However, others have reported a herringbone packing orientation for bulk packing[80] and our spectra here corroborate those results. Also of note, the inner interface frequencies are higher than the

outer frequencies (Tables 1-2), which I attribute to a difference in solvation environments experienced by molecules at the two boundaries.[109]

Interestingly, when the film thickness is decreased from 60 nm to 20 nm, and further to 11 nm (Figure 10b-c) nearly all VSFG signal amplitude disappears, excepting the single higher frequency peak near 1458 cm^{-1} within the *ssp* spectrum. This indicates a change in the net orientation of the symmetric C=C vibrations at lower thicknesses and highlights the fact the interfacial molecular structure in 6T films varies with film thickness. The loss of all *sps* signal suggests the 6T molecules have adopted a fully edge-on packing arrangement with the M-axis nearly perpendicular to the substrate at both interfaces. It has previously been shown that when 6T molecules are deposited at a submonolayer thickness on silicon dioxide, the long axis orients parallel to the substrate.[80] Typically, molecular orientation for a thicker film of a couple monolayers changes to an end-on orientation; the long molecular axis (L) is perpendicular to the surface.[93, 110] Hence, a change in the packing motif for films beyond the thickness of the wetting layer is expected here.[69, 80, 105] It is possible that sheets of laying pi-stacked 6T molecules are forming, opposed to the typical standing motif.

The coarse sampling of thicknesses in the data above presents compelling evidence that interfacial structural changes occur in sub- to multi-layer 6T thin films. In an effort to systematically identify this effect, VSFG measurements were carried out on the thickness gradient sample described in Figure 7 using *ssp* and *sps* polarization combinations. The VSFG responses have a large amount of destructive interference at low coverage thicknesses, as shown in the analysis above, making it difficult to visually

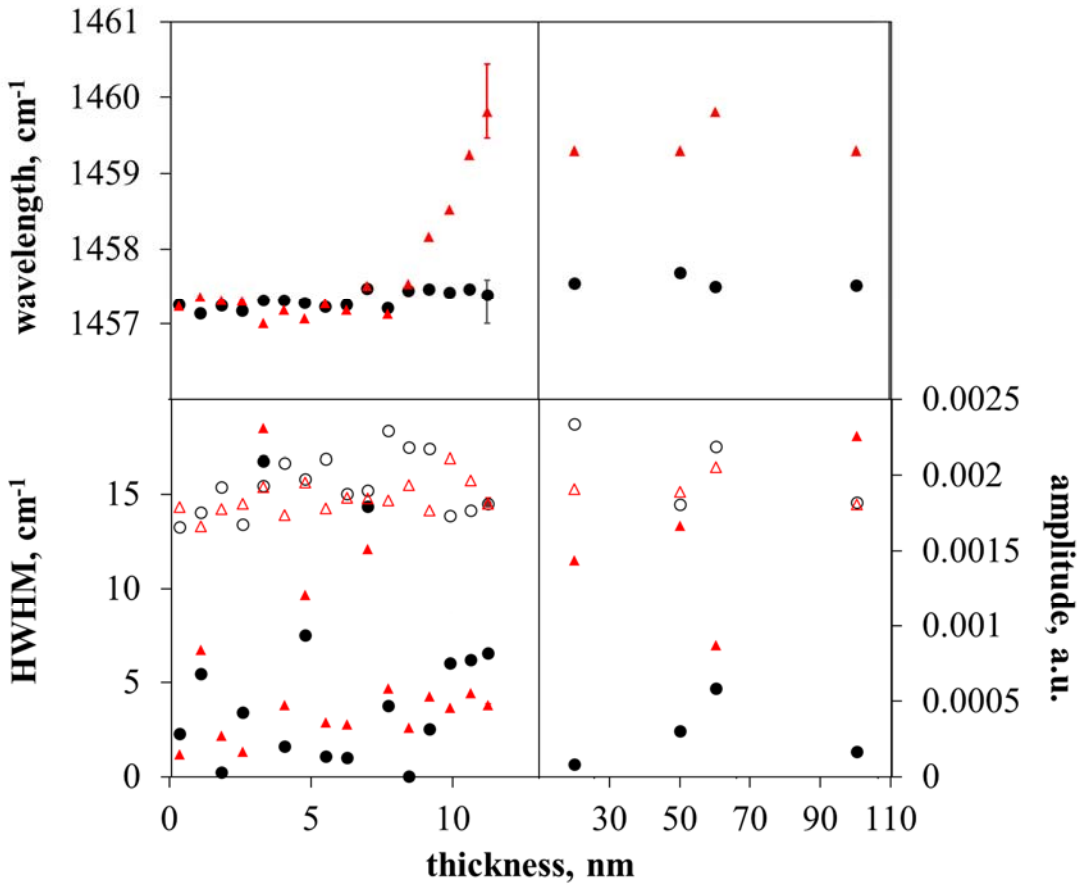

Figure 11. VSFG $\chi^{(2)}_{ssp}$ fit parameters for film thicknesses from 0.3 to 100 nm. Shown are fit parameters for a) center frequencies, b) amplitudes (solid markers) and half widths at half maximum (HWHM, open markers) for the air/6T (black circles) and 6T/SiO_2 (red triangles) interfaces.

evaluate the data. Hence, the thin film interference fitting routine is crucial to back out the interfacial $\chi^{(2)}$ responses.[12, 22, 43, 101] In all samples, the outer (air/6T) interfaces were constrained to lie between 1456.5–1475.8 cm^{-1}. Attempts to fit the data holding the buried interface constant or to let fitting parameters at both interfaces float while locked

Table 3. Original fitting values, with the upper and lower bounds supplying a 10% error, and the percent change from the original value.

Term	Value	Percent change (%)
Outer amplitude × 10^3	0.8170	
Upper bound	0.8227	0.69%
Lower bound	0.8113	0.70%
Inner amplitude × 10^3	0.4752	
Upper bound	0.4812	1.27%
Lower bound	0.4692	1.25%
Outer Γ (cm^{-1})	14.500	
Upper bound	14.601	0.70%
Lower bound	14.347	1.06%
Inner Γ (cm^{-1})	14.500	
Upper bound	14.797	2.05%
Lower bound	14.335	1.14%
Outer ν (cm^{-1})	1457.39	
Upper bound	1457.58	0.01%
Lower bound	1457.00	0.03%
Inner ν (cm^{-1})	1459.81	
Upper bound	1460.44	0.04%
Lower bound	1459.47	0.02%
Nonresonant amplitude × 10^3	0.8935	
Upper bound	1.4648	63.93%
Lower bound	NA	NA
Nonresonant phase	8.2029	
Upper bound	9.3755	14.29%
Lower bound	6.9880	14.81%

to each other were unsuccessful. This indicates that the molecular structure at the two interfaces is not the same and does not change uniformly. Thus, the frequency of the symmetric peak for the outer interface was constrained to be similar along the gradient. For the thickness range sampled in the gradient sample, *sps* response was not observed and was therefore not included in VSFG modeling.

For clarity in the following discussion, the fitting results are displayed graphically in Figure 11. Error bars are calculated for the 11 nm sample. Sum of the squares, SS, of the vertical residuals over the original and altered fits were taken:

$$SS = \sum_{\omega=1400}^{1500} |a_\omega - y_\omega|^2, \tag{54}$$

where ω is the frequency axis contained within the fit, running from 1400 to 1500 cm^{-1} in increments of 1, y_ω is a data value at frequency ω, a_ω is the data point from the fit at frequency ω. The percent error between the SS of the original fit and the altered fit was found through the following equation:

$$\text{percent error} = \frac{|SS_{original} - SS_{altered}|}{SS_{original}} \times 100\%. \tag{55}$$

Each parameter was changed individually until a percent error of 10% was reached, while the others were left with their value as solved initially by the fitting routine. The values obtained are shown in Table 3.

The most notable change to the fitted parameters is the convergence of the frequencies of the symmetric mode at lower 6T film thicknesses (Figure 11a). The C=C stretching vibrations at the air/6T interface are constant within ~0.5 cm^{-1}, even though they were not constrained that way. The 6T/dielectric C=C vibrations are higher than

those at the air/6T interface, as noted in the analysis of Figure 10. However, below a thickness of about 8 nm there is no discernable difference between the interfacial frequencies, suggesting a critical thickness below which the environment felt by 6T molecules at the two interfaces is identical. There is a slight decrease in the VSFG intensity of the *ssp* response at lower film thicknesses, but the amplitudes of the $\chi^{(2)}$ responses remain fairly consistent (Figure 11b). Our group has shown previously that multilayer interference effects can cause VSFG signals to increase and decrease in an oscillatory fashion as the film thickness imparts a variable phase shift between the inner and outer interfacial signals.[12, 22, 43, 101] Thus, it is expected that the VSFG intensity visibly decreases while the $\chi^{(2)}$ response remains unchanged.

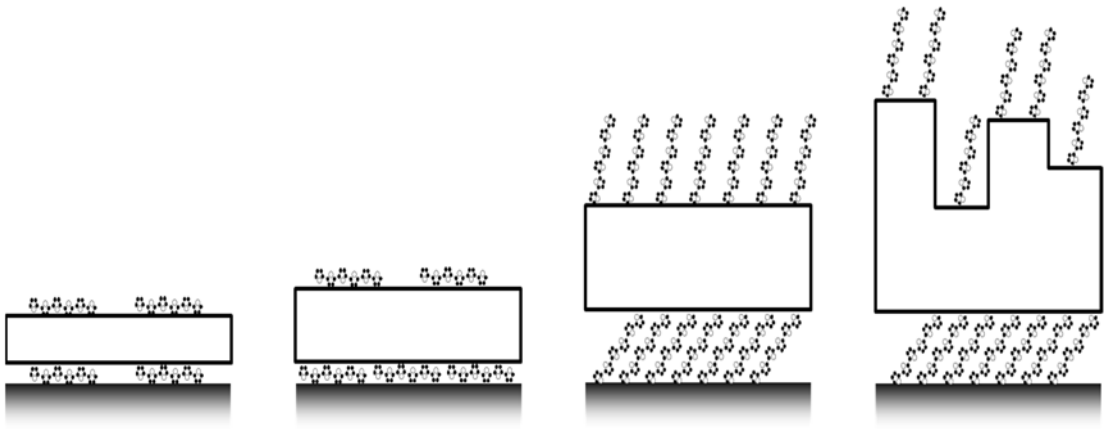

Figure 12. Representative schematics of 6T on glass at (from left to right) 8 nm, 11 nm, 20 nm, and 60 nm of deposition. The hollow shape between the boundary molecules represents the bulk VSFG inactive molecules.

One possible explanation for the data is that across all thicknesses the 6T-dielectric interactions dictate interfacial structure. Until 8 nm are deposited (just a few monolayers), the 6T molecules at the buried interface experience an identical environment as the outer molecules (Figure 12). As determined by VSFG, both sets of boundary molecules are situated with the molecular short axis perpendicular to the substrate.[80, 105] The growth mechanism up to this point and beyond to at least 11 nm is layer-by-layer, as shown by AFM. Between 8 and 11 nm of deposition the buried 6T molecules show an increase in the frequency of the C=C vibrational mode. This may be the result of a change in the packing density at the 6T-dielectric boundary (Figure 12) leading to a change in the solvation environment around the C=C vibrations. I attribute this to an interfacial phase change at this thickness range. Between 11 and 20 nm of deposition, the molecules undergo an orientation change, tilting to somewhere between edge-on and end-on. As other studies have shown, after a critical thickness is deposited the wetting layer reorganizes as intermolecular 6T forces overwhelm substrate forces.[69, 80, 105] However, as shown by the fitted *ssp* amplitudes, there is a greater *ssp* contribution at the buried interface, suggesting more edge-on character. The similarity between the orientations at both interfaces across all thicknesses would suggest a propagation of the buried interfacial packing motif throughout the rest of the sample, though it is exaggerated at the outer surface, since substrate forces are not present there. A final change occurs beyond 11 nm of deposited 6T that is consistent with Stranski-Krastanov deposition, where island formation becomes the dominant growth process, as shown by AFM (Figure 12). This is further substantiated by the much larger amplitudes at the

buried interfaces for thicker films, as the lack of the flat surface will decrease the VSFG response.

2.4. Conclusions

Despite its simplicity, the structural variability of 6T thin films is extensive. Understanding the structural and phase behavior of organic materials with nanoscopic thicknesses and microscopic dimensions is key to their successful implementation in electronic applications. Through VSFG spectroscopy it was shown that the average orientation of the 6T molecules on glass for the inner and outer interfaces is different depending on the thickness of the film. It was also shown, through using different polarization combinations, that the environment of the 6T molecules at the inner and outer interfaces are only identical at ultrathin thicknesses but differentiate upon reaching a thickness of a few molecular monolayers. In addition, the growth mechanism of 6T on glass is the Stranski-Krastanov growth transition, which was confirmed by AFM imaging.

The interfacial vibrational spectroscopy applied to 6T thin films shows that interfacial phase transitions occur beyond 8 nm thick. This observation addresses a fundamental question as to whether the buried interface dictates the outer interfacial structure, or vice versa. In many situations, the chemistry at buried interfaces is modified in attempts to impact the outer surface structure; presumably this effect is operational over a limited film thickness. The analysis in Figure 5 indicates that the 6T structure at the dielectric interface in fact converges to that of the air interface when the film

thickness falls below a threshold of 8 nm (a few molecular monolayers). One would expect the electrical performance in certain interfacial devices would also change over this thickness range. In fact this is often the case.[111] For example, polycrystalline pentacene OFETs showed a monotonic increase in charge carrier mobility up to saturation at five molecular monolayers.[83] 6T OFET performances typically maximize at lower thicknesses between two and three molecular monolayers (5 and 8 nm thick) depending on their deposition conditions.[82, 112] A common interpretation of the electrical response assumes that the buried interfacial structure is constant and a few monolayers completes the structure needed for all device transport to occur. My results in this chapter offer a more nuanced perspective that includes interfacial molecular structure during film growth and reveals that ultrathin films experience intermolecular forces across the film thickness that until a threshold film thickness enables molecules at the dielectric interface to undergo a transition independent from those at the air interface.

2.5. Acknowledgements

Partial support was received from the National Science Foundation under DMR-1611047. Portions of this work were conducted in the Minnesota Nano Center, which is supported by the National Science Foundation (NSF) through the National Nano Coordinated Infrastructure Network Award Number NNCI-1542202. Parts of this work were carried out in the Characterization Facility at the University of Minnesota, which receives partial support from the NSF through the MRSEC program. Zahra Sohrabpour assisted in completion of the project.

CHAPTER 3: APPLIED MODELING TOWARDS TEMPERATURE-DEPENDENT PACKING IN PENTACENE THIN FILMS

3.1. Introduction

Organic field-effect transistors are essential devices with a broad range of applications, including flexible displays,[113-114] flexible and printable plastic circuit boards,[115-116] radio frequency identification tags,[117] and sensors.[118] Pentacene is a promising large-area, cost-efficient, environmentally stable organic semiconductor. However, due to its low solubility at room temperature it is not amenable to commercial-processing techniques unless soluble precursors are used.[119-120] Vapor deposited pentacene thin films can achieve high charge-carrier mobilities needed for OFETs, but their performance is dependent on multiple factors including deposition process,[119, 121] phase of the deposited material,[122] impurity concentration,[123] grain size,[124] and even the method[125] and duration of storage.[126] These factors affect electrical mobility in devices by altering the orientation and ordering of pentacene molecules, making characterization of such molecular parameters an important goal for the field.

Substrate choice can be used as a control for pentacene phase and orientation.[127] When deposited on SiO_2 pentacene lies face-on until a critical number of molecules aggregate to form an island.[128] Beyond that threshold the molecules adopt some tilt

depending on the phase of the deposited film. Two major phases exist; a thin-film phase (TFP) in which the molecules stand near upright, and a bulk phase (BP) where the molecules have a greater degree of tilt.[122] Furthermore, there are two polymorphs of the bulk phase, and one can be irreversibly transformed into the other through the application of medium pressure.[129] It has been shown that devices manufactured with the TFP have a higher charge mobility than those with the BP.[122] Hence, control of phase of a deposited film is crucial for device performance. Deposition of self-assembled monolayers (SAMs) between the substrate and pentacene have been used to further increase device efficiency, as SAMs of different structure[130] and phase[131] can alter the deposition phase.

The deposition parameters also play an important role in dictating molecular structure in pentacene films. The TFP deposits at substrate temperatures near room temperature, while an increase in the substrate temperature increases the prevalence of the BP.[132] Lowering the temperature to the liquid nitrogen cooled regime results in what was initially believed to be a randomly-oriented amorphous deposit[122] but may instead be a structured face-on deposit.[133] Beyond a temperature-dependent critical thickness, the BP becomes the increasingly dominant structure.[132] Some groups have hypothesized that only the TFP nucleates at the surface of the SiO_2 substrate while the BP nucleates atop it, with the number of nucleation sites dependent on the substrate temperature.[122, 132, 134] The BP crystallites grow outwards as more layers are deposited, such that after some critical temperature-dependent thickness the BP crystallites overtake the TFP crystallites, hence the observed phase dependence on thickness. Alternatively, it has been proposed that the BP can nucleate within the first monolayer as well, forming distinct regimes of growth normal to the substrate.[126, 135]

Although there is ample data describing pentacene structure through the bulk of its thin films, there is limited research documenting the interfacial trends. The manifestation of phase behavior at interfaces is critically important to OFETs since charge transport occurs directly in this region for field-effect devices.[136] Differentiating the two mechanisms of growth described above is challenging but necessary to inform the use of pentacene in OFET applications. Vibrational sum frequency generation (VSFG) is an experimental method capable of determining molecular orientation and ordering at interfaces.[11, 88-90] In the work described in this chapter, I applied VSFG to pentacene thin films deposited at a range of deposition temperatures. X-ray diffraction (XRD) was used to confirm the formation of the characteristic TFP and BP structures, and then FTIR and VSFG spectroscopies were used to identify the vibrational features in each phase and their associated interfacial structures at different deposition temperatures.

3.2. Experimental

Materials. Pentacene was used as received from Sigma Aldrich. Pentacenequinone was purchased from TCI chemicals. Wafers were n-doped, single-side-polished, 500 μm thick Si wafers with a 100 nm thermal oxide layer (University Wafer). CaF_2 windows (A-Star) were 1 inch in diameter and 3 mm thick.

Sample Preparation. Vapor deposition of pentacene onto different substrates was performed in a home-built high-vacuum chamber. Sublimation lowers the number of impurities and improves charge mobility.[121] The substrate was heated with an Omega CN3000 power supply, and the temperature was monitored with a thermocouple attached

to the holder. The substrate holder was mounted above a crucible furnace (RADAK I, Luxel Corp). Deposition was performed at an average pressure of 6×10^{-6} Torr. A crucible loaded with pentacene powder was heated following a temperature profile of 5 °C / min until a 0.1 nm/s deposition rate was achieved (176.0 °C on average). Depositions were carried out using heated Si wafers and CaF_2 windows as substrates at various temperatures. The deposition rate and thickness were monitored by a calibrated QCM within the deposition chamber.

X-Ray Diffraction. XRD measurements were carried out with a Bruker Diffractometer (D8 Discover 2D) equipped with a graphite monochromator, a VÅNTEC-500 2D detector and a 0.8 mm collimator at the University of Minnesota Characterization Facility. Cobalt Kα radiation (λ = 1.7890Å) was used to illuminate the sample. All data were collected by scanning the X-ray incident angle (ω) from 0.5° to 10.5° with a constant diffracted angle (2θ) of 13°. Scans were performed in one frame for 900 seconds per frame at 40 kV and 35 mA. The 2D scans were converted to 1D intensity vs 2θ spectra with a resolution of 0.04° using the GADDS diffractometer software.

Fourier Transform Infrared Spectroscopy. Transmission mode spectra were collected on a Thermo-Electron Nicolet 6700 spectrometer. Attenuated total reflectance (ATR) FTIR spectra were acquired with a Thermo Scientific Attenuated Total Reflectance apparatus on the same instrument. All spectra were obtained with an average of 16 scans and a resolution of 1.0 cm^{-1}.

Vibrational Sum Frequency Generation Spectroscopy. The VSFG laser system has been described elsewhere and in Chapter 1.[97] A pair of narrow-band visible pulses

were created using a Fabry-Perot etalon (TecOptics, 12 cm^{-1} FWHM), as published previously.[52] The center frequencies of the visible pulses were tuned to 807.40 nm and 789.75 nm and separated from the laser output. The pulses were directed at the sample stage at 62° after co-alignment. The center frequency of the mid-IR pulse was tuned to 3050 cm^{-1} and directed onto the sample stage at 55°. Both the reference and the pentacene samples were attached to a vertical sample stage. ZnO with a thermal oxide layer deposited on a silicon wafer was used as a reference. This reference was collected for five frames of two minutes each in the *ppp* polarization combination, where *ppp* conveys the polarization of the VSFG, visible, and IR beams, respectively. These frames were averaged and fit with Gaussian line shapes. The Gaussian line shapes were used to normalize all other spectra to remove fluctuations in beam intensity. Five frames of 15 minutes each were collected and averaged for each pentacene sample in the *sps* and *ssp* polarization combinations. The *sps* combination samples vibrational modes oriented parallel to the substrate surface, while *ssp* probes transition dipoles oriented perpendicular. The 807.40 nm visible pulse was used to collect in *sps*, while the 789.75 nm pulse was used to collect in *ssp*. Spectra were fit using a global fitting routine that takes into account multilayer interference from signals generated at both interfaces.[12, 43]

Computational Method. Calculations were performed for pentacene and pentacenequinone molecules using Gaussian 16 software. Geometry optimization and infrared vibrational frequency calculation were carried out using both second-order Møller-Plesset theory (MP2) and density functional theory (DFT) at the unrestricted B3LYP level. The 6-31G (d, p) basis set was used for all atoms.

Atomic Force Microscopy. A Keysight 5500 scanning probe microscope was operated in contact mode using a model 9524B 90x90x8 micron scanner. The latter was freshly Z-recalibrated 3-4 days prior to this work (both Z scanner and Z sensor) using a model TGZ03 511 nm-step calibration grating from MikroMasch. The instrument was operated in closed loop X-Y. Z (type FORT from Applied Nanostructures) was used for all images reported. Surface tracking was actuated at ~10-20 nN of applied load. Height images were subsequently leveled by subtracting a fitted plane function. Z sensor measurements on subregions on film and bare-substrate (two terraces) were processed into 2-peak height histograms. Mean and standard deviation film thickness measurements were produced from this analysis as demonstrated in Figure 14.

3.3. Results and Discussion

XRD measurements were carried out on pentacene films deposited on CaF_2 and SiO_2 substrates at a range of temperatures to determine the bulk film structure. The XRD results provide information on the periodicity of the films in the direction normal to the surface. As shown inset in Figure 13 there are two sets of (00*l*) indexed reflections, where d_{001} is 15.5 Å ($2\theta \approx 6.6°$) for the TFP, and 14.5 Å ($2\theta \approx 7.1°$) for the BP.[132, 137] The (002) reflection for each phase is also apparent at higher 2θ values. Using a molecular *y* axis (Figure 13) length of 16.01 Å,[122] there is a tilt of 14.3° from upright for the TFP, and a larger tilt of 24.3° for the BP.[138-139] The (001) peaks were fit to Gaussians and the results are tabulated in Table 4. As the substrate temperature is increased during deposition, the contributions from the thermodynamically stable (001) and (002) BP peaks relative to the

TFP peaks are increased exponentially (Figure 13), a literature consistent result.[122, 132, 137]

Going from the substrate at room temperature to the substrate heated at 125 °C there was a sharp increase in the overall XRD intensity. This is likely due to an increase in the crystallinity when depositing at a higher temperature. At even higher substrate temperatures there was a significant decrease in the intensity of the XRD response, due to decreased adsorption of pentacene to the CaF_2 windows since the substrate temperature was nearing the vaporization temperature of pentacene.

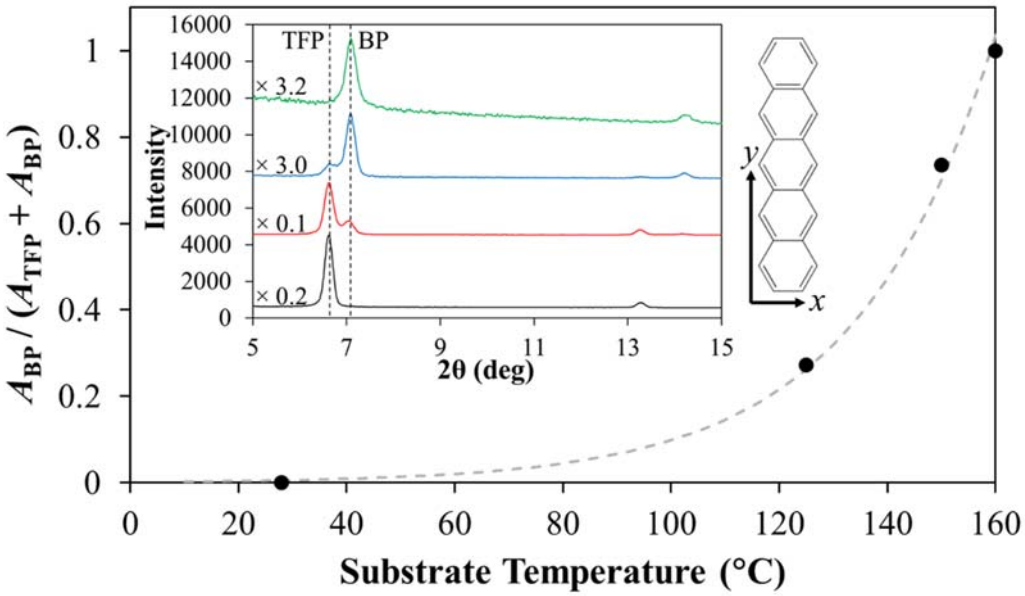

Figure 13. Area, *A*, of the (001) BP peak over the total (001) BP and TFP area fit with an exponential growth curve. *Inset plot:* XRD measurements of pentacene deposited on CaF_2 windows with substrate temperatures of 28 °C (black), 125 °C (red), 150 °C (blue), and 160 °C (green) during deposition. *Inset image:* Schematic view of pentacene with molecular axis labels.

Table 4. XRD measured standard deviation, amplitude, and area under each Gaussian for each (001) peak for samples on CaF_2 windows with different substrate temperatures during deposition.

	Thin-Film Phase			Bulk Phase		
	Amp.	**std. deviation**	**Area**	**Amp.**	**std. deviation**	**Area**
28 °C	19730	0.13	6380	0	0.00	0
125 °C	27990	0.14	10018	7801	0.19	3752
150 °C	324	0.20	162	1150	0.16	451
160 °C	0	0.00	0	1081	0.17	466

AFM measurements of film thicknesses for samples deposited at 28 °C, 125 °C, and 150 °C indicate 91, 91.5, and 53 nm, respectively, where an equal amount of material was directed at each sample; at 160 °C there was no deposition on the SiO_2 substrate due to resublimation from the substrate (Figure 14). AFM was used to determine the height difference between the substrate and the sample to solve for the true sample thickness (Figure 14). We calculated the step differences between the red highlighted boxes to be 182, 183, and 106 nm respectively for the samples deposited at substrate temperatures of 28 °C, 125 °C, and 150 °C. Deposition will be linear, so a sample with an expected thickness of 100 nm will have half the listed values above as a true thickness. For the three lower thicknesses on which there were measurable films, the trends in deposited phases on SiO_2 were the same.

FTIR spectroscopy was used to track the corresponding vibrational changes for pentacene through the bulk of the samples with respect to the phase of the deposited thin

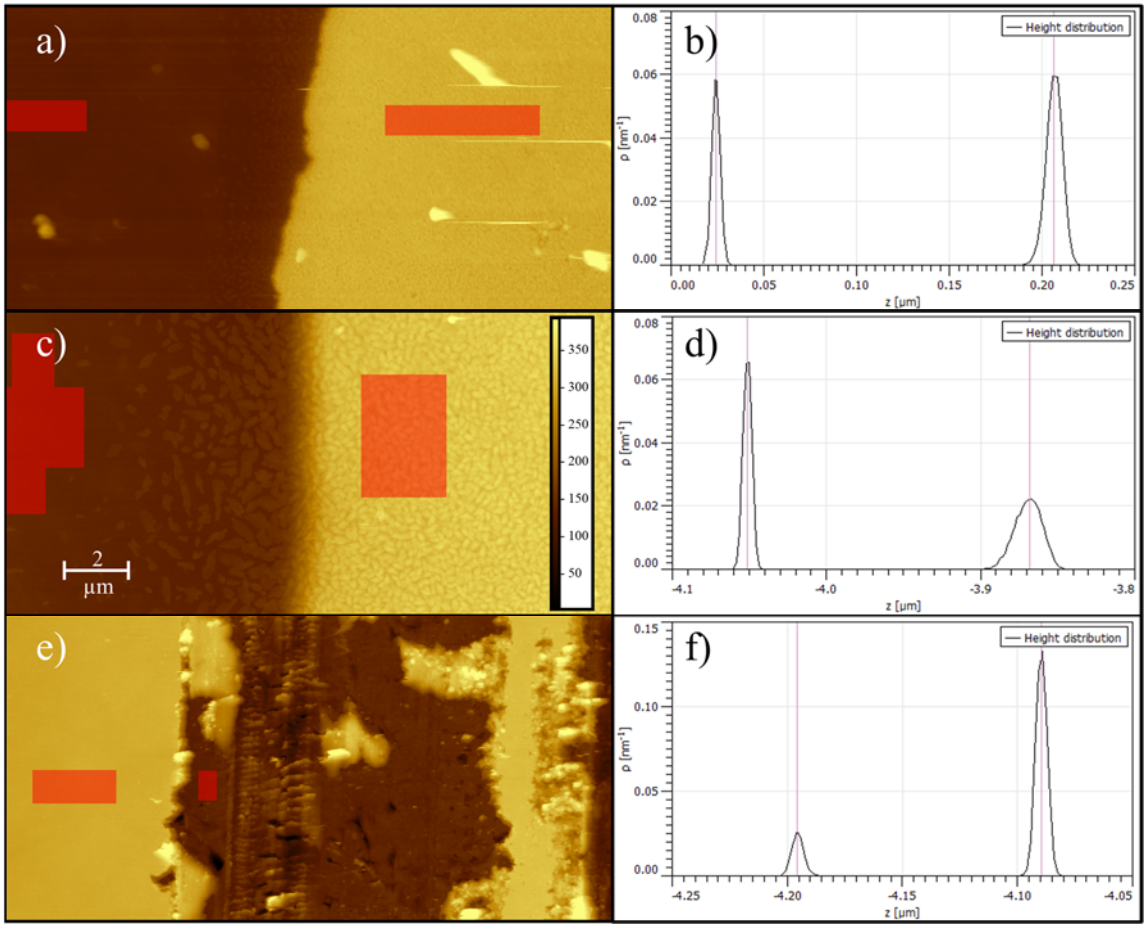

Figure 14. AFM topography images of samples with an QCM-measured deposition thicknesses of 200 nm with substrate temperatures of a) 28 °C, c) 125 °C (inset height scale for all images in nm), and e) 150 °C during deposition, and associated height distribution plots (b, d, f).

film. Commercial sources of pentacene often contain some non-negligible amount of pentacenequinone,[123, 140] and may also oxidize rapidly to this impurity in air.[141] The as-

received pentacene powder used to prepare samples in this study showed the C=O in-plane vibration at 1675 cm^{-1} and the combined C–C and C=O in-plane mode at 1615 cm^{-1} that are characteristic of pentacenequinone (Figure 15a).[142] An ATR-FTIR spectrum of pentacenequinone powder is provided in the same figure for comparison. Frequency calculations in Table 5 further support this assignment. A scaling factor of 0.9581 was applied for the theoretical calculations.[143-145]

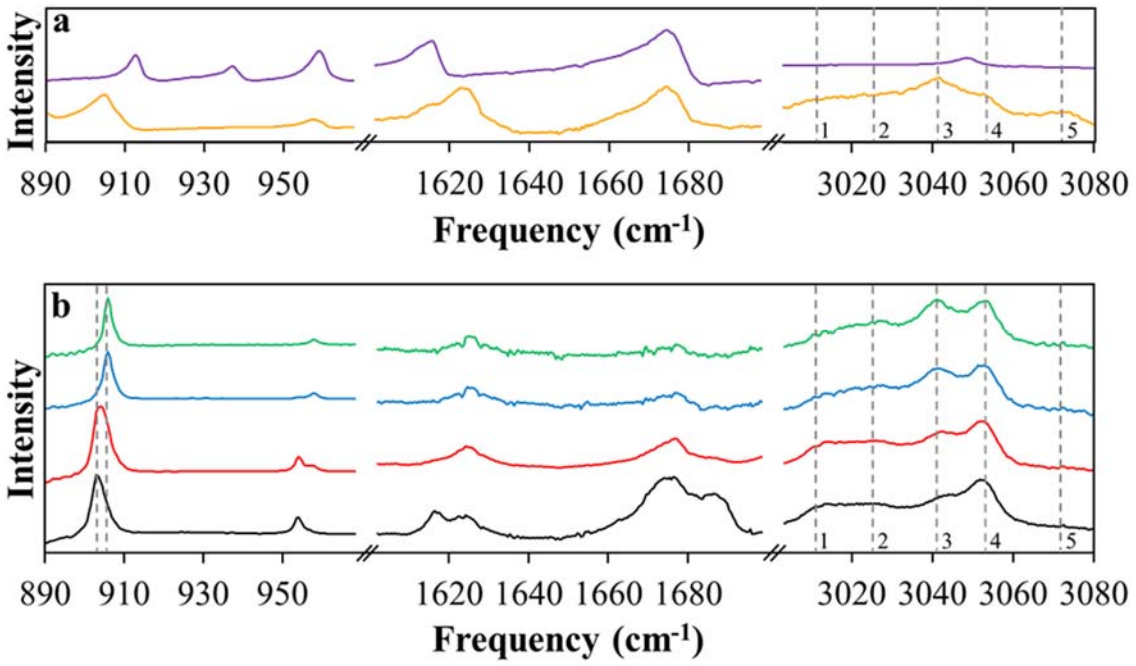

Figure 15. (a) ATR-FTIR spectra of powdered pentacene (orange) and pentacenequinone (purple). (b) FTIR transmission spectra of pentacene deposited on CaF_2 windows with substrate temperatures of 28 °C (black), 125C °C (red), 150 °C (blue), and 160 °C (green) during deposition.

Pentacenequinone is clearly present in the starting material. This is an important observation since it has been reported that pentacenequinone can lower the device performance.[146] Moreover, co-deposition of pentacenequinone can suppress the formation of the BP.[147] The FTIR spectra of pentacene films in Figure 15b are normalized to the 3052 cm^{-1} peak amplitude of the powder pentacene sample, while pentacenequinone powder is normalized to the 1675 cm^{-1} peak amplitude of the same sample, essentially

Table 5. Experimental and theoretical frequencies of pentacene and pentacenequinone vibrational modes.

	Pentacene		**Pentacenequinone**	
Mode	**Experimental Freq. (cm^{-1})**	**Theoretical Freq. (cm^{-1})**	**Experimental Freq, (cm^{-1})**	**Theoretical Freq, (cm^{-1})**
CH (*z*)	904	879.6	913	911.5
CH (*z*)	NA	NA	937	938.2
Ring str. (*y*)	NA	NA	959	977.3
CO (*x*)	NA	NA	1615	1601.7
Ring str. (*x*)	1624	1617.3	NA	NA
CO (*y*)	NA	NA	1673	1682.3
CH (*x*)	3013	3036.5	NA	NA
CH (*x*)	3027	3040.8	NA	NA
CH (*x*)		3042.5		NA
CH (*y*)	3042	3046.2	NA	NA
CH (*x*)	3053	3059.4	3046	3063.0
CH (*y*)	3072	3071.0		3074.2

showing the amount of pentacenequinone relative to pentacene. Thus, we observe a loss of pentacenequinone deposition as the substrate temperature is increased, which is as expected since pentacenequinone has a lower sublimation temperature and likely resublimes from the heated substrate. In addition, the normalized data show only a small C–H signal from pentacenequinone relative to pentacene, indicating that even at lower substrate temperatures the contribution of pentacenequinone to the vibrational spectrum in the C–H regime is relatively small.

The ring stretching modes between 1200 and 1500 cm^{-1} have been used to identify the average orientation of pentacene on a substrate,[148-149] but were not considered in this study due to low signal to noise. Prior work has utilized the C–H out-of-plane deformation vibrations (900–960 cm^{-1}) to assess the presence of the TFP and BP.[126, 150-151] It has been shown there is a blue-shift in the peaks at 905 and 956 cm^{-1} for the BP. The observed trend in this spectral region in Figure 15b is consistent with the XRD results, as there is an increase in the BP with an increase in deposition temperature. The FTIR spectra capture the associated phase changes through the bulk of the pentacene films. This consistency between XRD and the low frequency vibrations gives confidence that the high frequency aromatic C–H stretching region of the spectra (3000–3100 cm^{-1}) is representative of samples with the correct proportions of TFP and BP pentacene.

There are five distinct peaks (3012, 3026, 3042, 3052, and 3072 cm^{-1}) in the high frequency FTIR range. The vector describing the overall change in dipole that accompanies each of these modes has a particular alignment to the molecular coordinates of pentacene, which can be determined by gas-phase calculations of isolated molecules. In turn, the net orientation of these vibrational motions in pentacene films can be related

Table 6. Extremes (dark and light) of the vibrational movements for pentacene C–H modes as determined by B3LYP/6-31G (d,p). The orange arrow is the derivative of the dipole moment.

Mode	Frequency (cm^{-1})	Frame
ν_1(CH)	3013	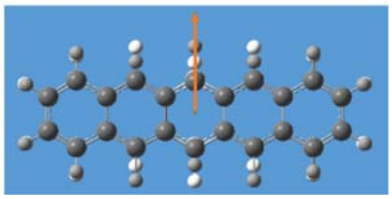
ν_2(CH)	3027	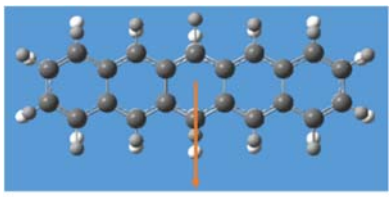
ν_3(CH)	3042	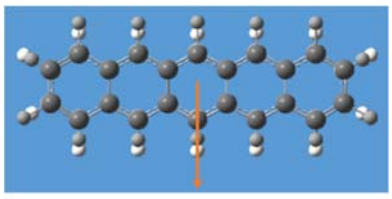
ν_4(CH)	3053	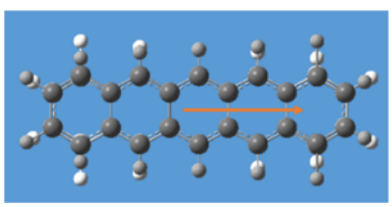
ν_5(CH)	3072	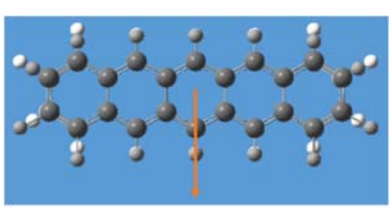

to the lab coordinate system by analyzing their intensities in the FTIR spectra. The dipole derivative vectors determined by DFT calculations are shown in Table 6 and indicate that the directionalities of the vibrations at 3012 cm^{-1}, 3026 cm^{-1}, and 3052 cm^{-1} are aligned overall with the short *x*-axis of pentacene (see Figure 13) whereas the 3042 cm^{-1} and 3072 cm^{-1} modes align to the long *y*-axis of a single molecule. These directional assignments corroborate experimental work by Hosoi and coworkers utilizing polarized FTIR measurements of standing pentacene molecules to determine the primary alignment

Table 7. FTIR peak areas of C–H vibrational modes for samples prepared on CaF_2 windows with different substrate temperatures during deposition.

Mode	Frequency (cm^{-1})	Relative peak areas			
		28 °C	**125 °C**	**150 °C**	**160 °C**
υ_1(CH) (*x*)	3012	0.19	0.19	0.13	0.10
υ_2(CH)	3026	0.28	0.30	0.29	0.30
υ_3(CH) (*y*)	3042	0.20	0.22	0.25	0.25
υ_4(CH)	3052	0.30	0.27	0.25	0.25
υ_5(CH) (*y*)	3072	0.02	0.02	0.08	0.07

of each vibrational mode with respect to the surface.[148] However, the calculated transition dipole moments are a single isolated molecule result and may not lead to trends in the ensemble averaged measurements of a pentacene thin film in Figure 15. To quantitatively analyze the pentacene films deposited at different temperatures, each high frequency spectrum in Figure 15b was fit by a sum of five Gaussians in the aromatic C–H stretching region (Table 7). The center frequencies and widths of each mode were globally shared

while the amplitudes were allowed to float. To account for differences in film thickness caused by poor adsorption at higher temperatures, the results for each spectrum were normalized to a total area of unity (example fit in Figure 16).

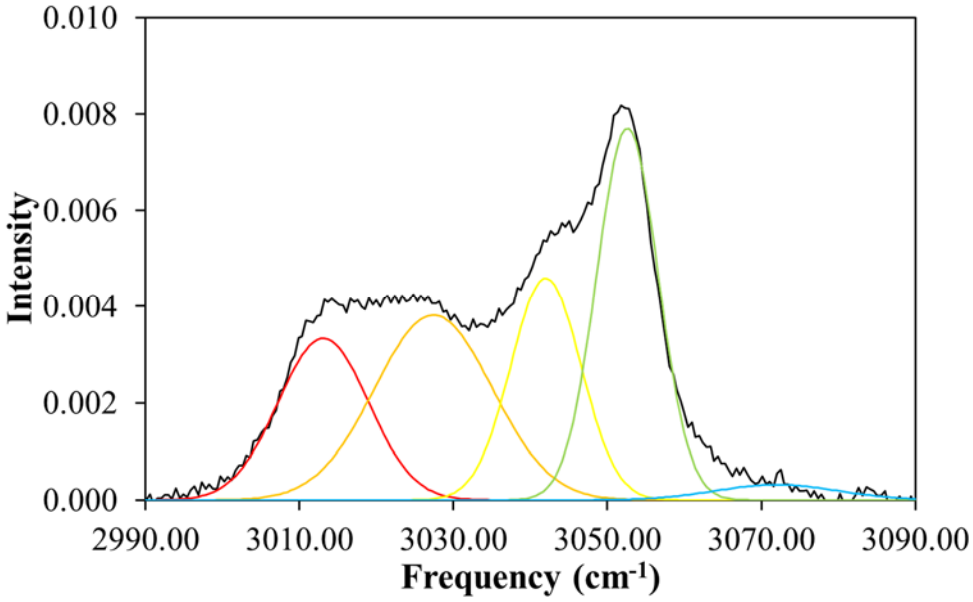

Figure 16. Example deconvolution of sample deposited at 28 °C fit using five Gaussians.

The perpendicular transmission geometry of the IR beam relative to the sample substrate in our measurements probes only dipoles oriented parallel to the substrate surface. Paired with the average tilt found through XRD, this means if a vibration is aligned within the plane of tilt then there will be an associated trend observed within the FTIR results. We see no experimental evidence of net alignment of the 3026 cm^{-1} vibrational mode as it follows no trend with change in tilt, in agreement with the literature.[39] The 3012 and 3052 cm^{-1} peaks both decrease with deposition temperature, consistent with a decreased net alignment of the molecular short axis with the film plane

as a larger proportion of BP is deposited. Conversely, the 3042 and 3072 cm^{-1} peaks display small increases with deposition temperature as would be expected for increased net alignment of the molecular long axis with the film plane. Of note, if identical measurements were performed using an ATR attachment or on a powder sample, the resulting signal may display different trends. It is the geometric limit intrinsic to the transmission experiment and the oriented structure of the molecules that allows us to view changes to a spectrum upon changes to the molecular tilt. The important point is that the CH vibrations follow the expected trends for net pentacene orientation in the TFP and BP. Thus we may use each of these peaks to identify the presence of each distinct phase within the substrate-relative geometric constraint.

XRD and FTIR spectroscopy provide measures of the relative amounts of the TFP and BP of pentacene through the entire thickness of the sample. Using VSFG spectroscopy we can obtain molecular information about pentacene molecules that reside specifically at material interfaces. VSFG is a process in which visible and infrared laser beams are spatially and temporally overlapped with one another on a sample generating a third phase-matched beam at the sum of the two frequencies.[11, 88-90] The combination of these three waves depends on the second order susceptibility, $\chi^{(2)}$, which is zero for centrosymmetric media. Hence, the bulk of an isotropic material will yield no signal, while at the interface where inversion symmetry is lost $\chi^{(2)}$ becomes non-zero. In addition, when the IR portion of the three-wave mixture covers a vibrational mode of the molecular system, there will be resonant enhancement of the VSFG signal, allowing one to obtain the interfacial vibrational spectrum of the sample independent of the bulk. Furthermore, polarization-selective VSFG allows one to characterize the relative

orientation of interfacial pentacene molecules. For example, when using the *sps* polarization combination only the IR dipoles oriented parallel to the substrate surface plane will be probed. To our knowledge, the only VSFG spectrum of pentacene recorded with an IR pulse at these frequencies was done with a single polarization combination (*ppp*) from a field effect transistor with a gate voltage of -50 V applied to generate a large non-resonant background; the spectrum showed only a negative-going feature around ~3050 cm^{-1}.[152] The results presented here yield greatly enhanced spectral information.

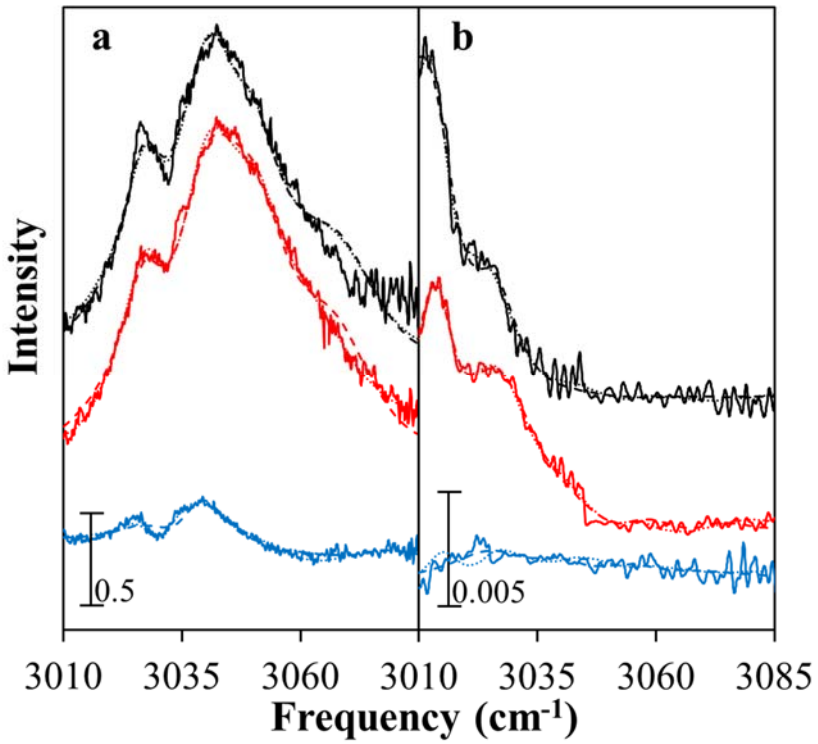

Figure 17. VSFG spectra in (a) *ssp* and (b) *sps* polarization combinations on SiO_2 with substrate temperatures of 28 °C (black), 125 °C (red), and 150 °C (blue) during deposition and the fits using the co-nucleation (dashed) and the buried TFP interface (dotted) assumption.

When using the *ssp* polarization combination (Figure 17a) I measured large peaks near 3026, and 3042, with smaller peaks at 3052 and 3072 cm^{-1}. This polarization combination is enhanced for transition dipole moments that are orthogonal to the sample plane. The lack of the 3012 cm^{-1} peak and small contribution from the 3052 cm^{-1} peak, paired with the large contributions from the others as stated above, are consistent with near-perpendicular molecules at the film interfaces. Further supporting this, the 3012 cm^{-1} peak has a large intensity in the *sps* polarization combination, which preferentially samples in-plane transition dipoles. As stated previously, two different growth mechanisms have been proposed in the literature that are shown schematically in Figure 18. In one, both phases co-nucleate at the interface; we call this the co-nucleated mechanism. In the other only the TFP exists at the buried interface while the BP deposits overtop; we call this the buried TFP mechanism. The interfacial specificity of VSFG can be used to separate these two mechanisms.

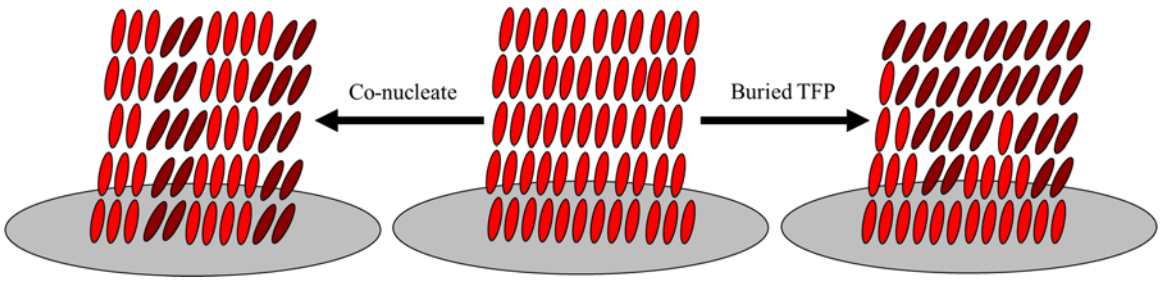

Figure 18. Proposed packing motifs of TFP (red) and BP (maroon) pentacene molecules upon an increase in temperature, where co-nucleation occurs (left) or the buried interface remains entirely composed of TFP (right).

The VSFG spectra were fit through the lens of both assumptions. The fitting procedure takes into account multilayer interference of VSFG signals generated from the inner (SiO_2/pentacene) and outer (pentacene/air) interfaces.[12, 43] The thicknesses used in the calculations were determined by AFM, and were 91, 91.5, and 53 nm respectively for the samples deposited with substrate temperatures of 28 °C, 125 °C, and 150 °C (Figure 14). To model co-nucleation, the inner and outer interfacial second order susceptibilities ($\chi^{(2)}$) were set to be equivalent for each individual sample. Modeled through Lorentzian line-shapes, they shared center frequencies, (HWHM), and amplitudes. Though the true interfacial responses may not be ideally equal, the discrepancy between them should be small enough for the fit to be acceptable without allowing variance. The frequency centers for each mode were globally shared amongst all three samples. The refractive indices were approximated by data extraction from a previous literature report.[153] The shape of the response from the *ssp* polarization combination is more dependent on the refractive indices, which may allow some room for error in the fit.[43]

Alternatively, to model the constant buried TFP interface scenario, the inner $\chi^{(2)}$ signals across all samples were set to be identical, along with the outer response from the 28 °C sample, since the XRD showed the entirety of the sample to be composed of the TFP. The outer modes were allowed to float independently from the inner modes for all samples shown to have the BP present by XRD. Finally, the frequency centers were again shared globally between all samples. The collected spectra in Figure 17 are overlaid with the fit results using both fitting approaches, while selected fitting parameters are tabulated in Table 8. Excluding the buried TFP-assumed motif fit for the *sps* spectra of

the 150 °C sample, both models resulted in acceptable fits, but the trends in the fitted parameters show a clearer story.

In the co-nucleation mechanism, increasing the temperature increases the proportions of BP that co-nucleates with TFP at the substrate surface. Within this model, we expect the 3012 cm^{-1} and 3052 cm^{-1} modes to have weak *ssp* responses that increase with temperature as the proportion of BP at the interfaces increases. This remains consistent with the FTIR peak area decrease with temperature since that measurement was probing the in-plane net alignment through the bulk while the *ssp* VSFG signal is selectively probing the out-of-plane net alignment change at the interfaces. The 3042, and to a greater extent, the 3072 cm^{-1} modes should decrease with temperature as the corresponding tilt in the interfacial molecules with the formation of the BP sequentially weakens their alignment to the surface normal. As the 3026 cm^{-1} mode showed no trends, I offer no analysis of it. Under the buried TFP mechanism, I expect the same trends but only at the outer interface. Conversely, when the *sps* data are fit under either motif, I expect a decrease in the 3012 and 3052 cm^{-1} modes, while the 3042 and 3072 cm^{-1} modes should increase.

Table 8 shows the VSFG contributions for each of the five modes at the three substrate temperatures examined. With the forced co-nucleation fit we observe the following trends in the short- and long-axis modes of the *ssp* fit. The 3012 cm^{-1} mode is exceedingly weak but increases with deposition temperature and the 3042 cm^{-1} mode decreases overall as well. The 3052 cm^{-1} mode shows the opposite trend, decreasing though it was expected to increase, while the 3072 cm^{-1} mode shows no trend. In contrast, excluding the fit parameters for the 3042 cm^{-1} mode, all vibrations in the buried TFP

Table 8. Outer and inner fitted VSFG areas for the *ssp* and *sps* spectra with substrate temperatures of 28 °C, 125 °C, and 150 °C during deposition, fit using the co-nucleation and the buried TFP interface assumption along with the expected trends going from low to high temperature.

	Mode	Inter-	Co-nucleated motif				Buried TFP interface motif			
	(cm^{-1})	face	Expected	28 °C	125 °C	160 °C	Expected	28 °C	125 °C	160 °C
i combination	3012	Outer	Decrease	4.6E-04	1.9E-04	2.8E-11	Decrease	1.3E-04	9.6E-05	7.7E-04
		Inner	Decrease	4.6E-04	1.9E-04	2.8E-11	NA	1.3E-04	1.3E-04	1.3E-04
	3026	Outer	NA	2.0E-04	4.5E-04	1.1E-04	NA	4.8E-04	4.9E-04	8.1E-05
		Inner	NA	2.0E-04	4.5E-04	1.1E-04	NA	4.8E-04	4.8E-04	4.8E-04
	3042	Outer	Increase	8.3E-06	7.9E-06	3.1E-05	Increase	1.4E-04	1.3E-05	8.5E-08
		Inner	Increase	8.3E-06	7.9E-06	3.1E-05	NA	1.4E-04	1.4E-04	1.4E-04
	3052	Outer	Decrease	4.4E-05	4.4E-05	3.7E-05	Decrease	3.2E-05	5.6E-05	1.5E-07
		Inner	Decrease	4.4E-05	4.4E-05	3.7E-05	NA	3.2E-05	3.2E-05	3.2E-05
	3072	Outer	Increase	6.9E-07	2.2E-05	3.5E-05	Increase	8.2E-05	3.6E-04	1.8E-09
		Inner	Increase	6.9E-07	2.2E-05	3.5E-05	NA	8.2E-05	8.2E-05	8.2E-05
***sps* combination**	3012	Outer	Increase	3.7E-09	8.5E-08	8.5E-07	Increase	9.2E-07	7.6E-03	1.3E-03
		Inner	Increase	3.7E-09	8.5E-08	8.5E-07	NA	9.2E-07	9.2E-07	9.2E-07
	3026	Outer	NA	1.5E-03	1.5E-03	6.6E-03	NA	1.4E-03	7.5E-04	6.3E-03
		Inner	NA	1.5E-03	1.5E-03	6.6E-03	NA	1.4E-03	1.4E-03	1.4E-03
	3042	Outer	Decrease	4.7E-03	4.7E-03	3.1E-03	Decrease	4.0E-03	6.8E-04	1.5E-05
		Inner	Decrease	4.7E-03	4.7E-03	3.1E-03	NA	4.0E-03	4.0E-03	4.0E-03
	3052	Outer	Increase	3.7E-04	1.3E-03	1.4E-04	Increase	4.8E-04	2.3E-03	1.6E-03
		Inner	Increase	3.7E-04	1.3E-03	1.4E-04	NA	4.8E-04	4.8E-04	4.8E-04
	3072	Outer	Decrease	7.1E-04	5.3E-04	5.6E-04	Decrease	6.4E-04	1.0E-06	1.1E-05
		Inner	Decrease	7.1E-04	5.3E-04	5.6E-04	NA	6.4E-04	6.4E-04	6.4E-04

model fit show the wrong or inconsistent trends with temperature at the outer interface while holding the buried interface fixed, further supporting the co-nucleation model. Moving to the *sps* fit, we find that the best fit parameters follow the expected trends for

the co-nucleation modeling. Through the lens of this motif, both the highest and lowest frequency modes follow the expected trends, while there is inconsistent change in the 3042 and 3052 cm^{-1} modes. However, when examined through the buried TFP interface, in addition to an inability to fit the highest temperature spectrum, no expected trends are observed. Thus, the data point to the co-nucleation deposition motif.

3.4. Conclusions

In the work described in this chapter, I deposited samples of pentacene with bulk systems composed of distinct phases. Using a geometrically constrained bulk spectroscopy we observed correlation between molecular tilt and signal intensity for multiple vibrational modes. Application of this resolution using an interfacial and geometric limited spectroscopy afforded the ability to elucidate the interfacial deposition motif pentacene, determining a co-nucleation theme. This information may be used in tandem with electrical measurements to draw conclusive proposals towards the charge-transfer mechanisms of films deposited across a range of substrate temperatures on devices, as the temperature plays a key role in device efficiency.

3.5. Acknowledgments

Parts of this work were carried out in the Characterization Facility at the University of Minnesota, which receives partial support from the NSF through the MRSEC program. The authors acknowledge the Minnesota Supercomputing Institute

(MSI) at the University of Minnesota for providing resources that contributed to the research results reported within this paper. URL: http://www.msi.umn.edu. Zhihao Wu and Grace Gretz assisted in completion of the project.

CHAPTER 4: EXTENDED MODELING: SOLVING THE BULK REFRACTIVE INDICES

4.1. Introduction

The refractive index is a complex-valued material property that defines how light is transmitted, absorbed, and reflected by a thin film. It has a direct relationship to the dielectric constant and thus a defining role in Coulombic forces between charged particles and the transport of wave-like particles such as electrons through a medium. Determining the refractive indices of materials is increasingly important as the science of thin films advances and spectral ellipsometry remains the quintessential technique for their determination.[154-155] Ellipsometry measures the optical interference generated within a material system by mapping the wavelength-dependent change in phase offset, Δ, and polarized amplitude ratio, Ψ, for an elliptically polarized reflected beam. The two ellipsometric variables can be calculated using the total reflectivity of a stratified thin film system, where the reflectivity terms are built using an infinite series of partial waves defined by Fresnel factors.[154-155] The experiment can be improved by charting the ellipsometric variables not only as a function of wavelength, but also incident angle using variable angle spectroscopic ellipsometry (VASE). Decades of development have rendered ellipsometry a turnkey method for contact-free solution of the absorptive and dispersive coefficients as well as film thicknesses and other material properties. Alternative methods, while certainly not as robust, have been used to resolve the optical coefficients. In principle, any spectrometer in reflection or transmission geometry paired with a high-quality polarizer can be used to determine refractive indices. To overcome

the limits polarizers impart on collection range, polarizer-free IR reflectance spectroscopy, both with a near-normal incident angle[156] and at typical system incident angles[157] has demonstrated acceptable measurement of refractive indices. Prism coupling has also been successfully applied towards their solution.[158-159]

Complex refractive indices play a key role in nonlinear spectroscopies, such as vibrational sum frequency generation. As detailed in previous chapters, VSFG probes the vibrational characteristics of interfaces and can be used to reveal structural details for molecules at the boundaries of material layers.[21] Within a stratified system, a planar slab of material always has two interfaces. The break in symmetry at these boundaries permits VSFG signals to be generated from the top and bottom of each material. Complexity arises in the propagation of these signals as a result of the layered nature of the system. The incident visible and IR pump lasers accumulate frequency-dependent phase shifts as they traverse the stratified system, which are dictated by the layer refractive indices. By definition, each interface between different materials possesses contrasting refractive indices that reflect, transmit, and refract the pump beams multiple times, leading to interference effects that alter the field amplitudes of each beam at each interface. The frequency-summed signals consist of vibrationally nonresonant contributions from all interfaces and vibrationally resonant signals from locations where material vibrations match the frequencies in the IR pump beam; signals are generated in both the transmitted and reflected phase-matched directions. The VFSG signals must then propagate across all layers and refractive boundaries, experiencing frequency- and refractive index-dependent reflection, transmission, and phase accumulation before escaping the stratified system. The resonant and nonresonant VSFG signals generated from the top and bottom

interfaces are mixed and interfered, which hinders the ability to discern the individual interfacial responses without proper modeling.

The optical interferences described above are a perennial challenge in coherent spectroscopies of thin films.[88, 160-161] Conversely, this same interference is essential in an ellipsometric measurement where an infinite geometric series of reflections is used to resolve the entanglement. This mathematical approach has been extended through transfer matrix formalism to model VSFG systems as well.[12, 22, 43, 101] In VSFG, the complex refractive indices of all bulk materials are necessary inputs to solve for the nonlinear susceptibilities, whereas in ellipsometry they are the solvable unknowns. In this chapter, I demonstrate the novel use of sum frequency generation as a proxy for ellipsometry, using the intrinsic optical interference effects as a tool to not only solve the interfacial resonant responses, but also elucidate the refractive indices of a vibrationally active material. Naturally, this introduces new adjustable parameters into the fit that must be balanced with new known variables in order to constrain a global fit to the data. I explore the sensitivity of VSFG experiments to several experimental variables (material thickness, beam angle, pump wavelength, etc.) by globally fitting simulated spectra with a shared, adjustable refractive index. The inclusion of multiple experiments, each with a different degree of optical interference by way of parameter variation, serves to increase the certainty of the output refractive indices, akin to the range of incident angles used to improve confidence in a VASE experiment.

The analysis in this work uses a mathematical fitting routine built through transfer matrix formalism for stratified systems probed in reflection geometry, as described in Chapter 1.[12, 22, 43, 101] Each set of formulas in the fitting routine is composed of the

refractive indices along with the geometric terms describing the system. Therefore any error in the refractive indices will be propagated throughout the entire system resulting in an improper fit. The complex refractive index, n, is given by equation 17 which is frequency dependent. The frequency- and polarization-dependent Fresnel factors that describe partial transmission and reflection at an interface are defined through the refractive indices and the angles of refraction, θ, in both materials comprising the interface. While the multilayer reflectivity terms important to ellipsometry are typically built using only reflectivity or a geometric approach,[28] we model our VSFG system using transfer matrix formalism, utilizing all four terms to build a matrix of refraction.[162] Both techniques also require the spatial phase offset, ϕ, to account for propagation of light (equation 25), which is then leveraged to construct the phase matrix in VSFG, the analog of Δ in ellipsometry. Combined with the matrix of refraction, these important matrices are the basis of nearly all the terms used to build the transfer matrix formalism based routine.[12, 22, 43, 101]

4.2. Experimental

In the following, I discuss several experimental methods to pair with the fitting routine for modeling the refractive indices. In each I apply a default description of the material system and resonant responses. Unless stated otherwise the simulated VSFG response is modeled by a 100 nm organic layer overtop a silicon substrate (assumed to have no lower boundaries) with a 100 nm thermal oxide layer. N,N′-dioctyl-3,4,9,10-perylenedicarboximide (PTCDI) is applied as the organic layer as it has been extensively

modeled in the past, the refractive indices have been measured using IR VASE, and the C=O stretching vibrations have good VSFG intensity.[88-89] A monochromatic visible source at 800 nm and an incident angle of 55° was used, while the IR range extended from 1600 to 1750 cm^{-1} with an incident angle of 50°. Two resonances were applied, where the buried interfacial responses were shifted from the outer. The inner responses were centered at 1652 and 1685 cm^{-1} with amplitudes of 0.1 and HWHMs of 7 cm^{-1}, while the outer responses were shifted 3 cm^{-1} higher. These values were chosen based on the experimental work presented at the end of the report. Through symmetry there is a reduction in available non-zero sampling elements in a VSFG experiment.[21] The available tensors are probed using the *ssp*, *sps*, *pss*, and *ppp* polarization combinations, where the *abc* notation signifies, in order, the polarization of the sum frequency, visible, and IR pulses.

Silicon wafers were purchased from the Minnesota Nano Center (Si, single side polished, 4”). Substrates were cleaned prior to oxidation using the well-established RCA cleaning method.[163] A Semitool ST-260D spin rinse dryer was used to dry the substrates between cleaning steps. SiO_2 films were developed using a Tylan oxidation furnace. Samples were oxidized using a steaming method (O_2 and H_2 gas) at 1000 °C for varying amounts of time, ranging from 4.5 to 48.0 minutes. Each unique oxide thickness was prepared individually. Oxide thicknesses were determined by film thickness mapping (Filmetrics, F50-EXR) using a Tungsten-Halogen light source, and measured at 25 points across each wafer. PTCDI was deposited using a home-built organic vapor deposition chamber. Deposition thickness was monitored by a QCM with a 0.45 tooling factor. 100 nm films of PTCDI were deposited at a rate of 0.1 Å/s at an average pressure of 7.4×10^{-6}

torr and temperature of 205 °C. Gold strips for nonresonant referencing were deposited in equal thickness to the PTCDI on each sample using a Temescal E-beam Evaporator. A deposition rate of 5 Å/s was used, and monitored by an inset QCM with a 0.45 tooling factor. Sections of each sample were covered before PTCDI deposition to make space for gold using Kapton polyimide tape.

The laser system has been described previously.[97] A Fabry-Perot etalon (TecOptics, 12 cm^{-1} FWHM) was used to separate the narrow-band visible pulse, centered at 807.5 nm with a HWHM of 7.36 cm^{-1} from the IR pulse.[52] The visible pulse was directed towards the sample stage at 55°. The center frequency of the mid-IR pulse was tuned to 1650 cm^{-1} and directed onto the sample stage at 50°. Samples were referenced by gold strips deposited on each sample. This reference was collected for five frames of two minutes each in the *ppp* polarization combination. References were fit by Gaussian line shapes before usage to normalize the sample spectra, which were collected for five frames of five minutes each. Fitting was performed using a global fitting routine discussed in the text.[12, 43] The sum frequency output was directed into a dispersive monochromator (Princeton Instruments, Acton 2150i) before imaging by a liquid nitrogen cooled CCD camera (Princeton Instruments, Spec-10).

4.3. Choosing the Right Variables

A number of parameters can be varied in a VSFG measurement to allow one to solve for sample refractive indices, though each is accompanied by varying degrees of experimental viability. One option is to change the parameters of an incident beam. If a

laser setup does not have collinear IR and visible beams, then either beam angle could be independently adjusted. The consequential change to the phase-matched sum frequency output would be smaller and more easily corrected if a change to the IR angle was introduced, compared to a change of the visible angle since the higher energy beam has a larger contribution to the phase-matched direction. However, even with only a change to the IR, the difficulty in this measurement still lies in the ability to replicate the pointing of the spectrometer entrance slit. The user could rotate the sample or both of the incident beams in tandem for an even greater experimental range. Yet this also requires a correction to the direction of the sum frequency output. The monochromatic visible wavelength could be used as a controlled variable to produce a set of spectra to fit for the refractive index. This would require fairly wide tunability in order to introduce enough variation in the spectral interference, and, like the beam angle variations, the phase-matching conditions of the output would need to be accommodated.

Altering the thickness of a layer in the sample rather than the incident beams requires minimal corrections to the sample stage but necessitates multiple samples. Changing the thermal oxide thickness can be easily corrected by mounting the sample on a micrometer-controlled adjustable stage, so that the surface of each sample can be consistently positioned at the overlap location of the lasers. Changes to the thickness of the vibrationally-active layer would certainly provide a useful test, however the user risks changing the bulk and interfacial structure through this process.[164-166] Finally, a vibrationally inert over-layer could be deposited on top of the active-layer, spanning a range of thicknesses as long as the over-layer does not alter the order and orientation of the vibrationally active material it is protecting. A user need not be limited to only a

single method. For example, an etalon[52] or pulse shaper[97] could be used to produce two frequency-resolved visible pulses from the regeneratively amplified pump that could both generate independent VSFG signals. A series of samples with different thicknesses could be measured, utilizing changes to both frequency and thickness in combination.

To test this I considered a model system of vibrationally-active PTCDI deposited on a layer of thermally-grown silica on a substrate of silicon. I used previously determined refractive indices and second order susceptibilities for PTCDI, SiO_2, and Si to calculate model VSFG data sets for all four polarization combinations as a function of each of the four variables described above (beam angle, visible wavelength, oxide thickness, and PTCDI thickness).[88] Figure 19 shows how the VSFG spectra change as a function of an oxide layer thickness from 0 to 1000 nm for each of the four relevant VSFG polarization combinations. Since the second order susceptibilities, $\chi^{(2)}$, (i.e. the interfacial responses) are identical across each calculation, the oscillating signal intensities are due solely to interference, which depends on the refractive indices and beam polarizations.[12, 43]

Datasets like these were generated for a range of beam angles, visible wavelengths, and PTCDI thicknesses in addition to oxide thicknesses (Figure 19) to assemble four test cases. I then replaced the PTCDI layer with a new material with adjustable refractive indices to perform the fit. The imaginary refractive index was modeled using Gaussian peaks, while the real spectrum was constructed from the imaginary using the Kramers-Kronig transformation (equation 18).[167] An additional constant offset term was added onto to the real index to account for dispersion outside the

spectral measurement window. Two peaks were used in the fit, equal to the number of C=O vibrational modes present in PTCDI. While the imaginary refractive index of

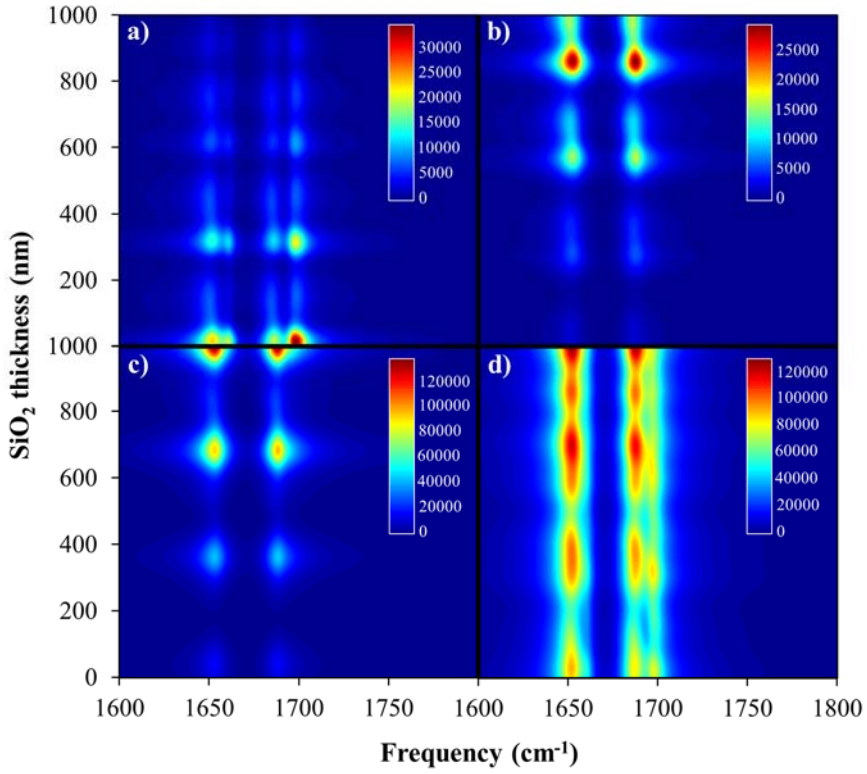

Figure 19. VSFG intensity (inset scales) as a function of oxide thickness for a sample of PTCDI over a silicon substrate with a thermal oxide layer spanning a range of thicknesses for the a) ssp, b) sps, c) pss, and d) ppp polarization combinations.

PTCDI as determined by IR VASE cannot be perfectly described with only two peaks as the true line-shapes are not required to be perfectly Gaussian, the VSFG spectra can still be fit sufficiently well. In a situation where the user lacks prior knowledge of the refractive indices it may not be intuitive to include enough peaks to perfectly trace the

true indices, and a value equal to the number of vibrational modes provides a minimalist starting approach. Finally, the resonant features in the $\chi^{(2)}$ spectrum were modeled with Lorentzian line shapes.

The cost function is solved using a bounded minimization function in Matlab.[168] This optimization utilizes the Nelder-Mead simplex algorithm to perform a search for minima.[169] The exit condition for each optimization was a set tolerance value ($1x10^{-6}$). Though search-based methods work well when many variables are present, efficiently narrowing down the search space, it is not as likely to find a local or global minima as an analytical solution. However, analytical methods are cumbersome, at times exceeding feasibility. Within the routine there is some flexibility afforded to each parameter as the number of variables leads to a multi-modal minima distribution as the parameters are correlated and may compensate for each other. A difference between the true and fitted offset value can potentially be accommodated by changes to the nonlinear susceptibility descriptors. Therefore, globalizing variables across a wider and larger range of input spectra can lower the overall error. I examined each of the following two methods using a parameter range viable within the limits of our own laboratory setup. I first attempted to fit independently the simulated VSFG data for each polarization combination. Within the given fit for a unique polarization, each sample shared the Lorentzian $\chi^{(2)}$ parameters. This is an idealized simulation, and collected experimental results in the laboratory setting may have too much system variance to be fit in such a manner. In the second method, all four polarization combinations were fit in tandem, allocated a single set of refractive indices for all polarizations, while the $\chi^{(2)}$ responses were unique for each

polarization combination. The starting guesses and constraints for each approach are shown in Table 9 for both the resonant and index terms.

Table 9. Starting guesses, and upper and lower constraints for the center frequency, ν (cm^{-1}), the amplitude, a, and the HWHM, Γ (cm^{-1}), for the lower, l, and higher, h, frequency modes for the inner and outer resonant responses and refractive indices

		Parameters		
		Guess	**Upper**	**Lower**
Resonant Terms	ν_l	1653.00	1665.00	1640.00
	a_l	0.050	1.000	0.000
	Γ_l	10.00	15.00	5.00
	υ_h	1687.00	1700.00	1675.00
	a_h	0.050	1.000	0.000
	Γ_h	10.00	15.00	5.00
Indices Terms	$\nu_{n,l}$	1660.00	1670.00	1650.00
	$a_{n,l}$	0.200	1.000	0.000
	$\Gamma_{n,l}$	5.00	15.00	2.00
	$\upsilon_{n,h}$	1695.00	1705.00	1685.00
	$a_{n,h}$	0.200	1.000	0.000
	$\Gamma_{n,h}$	5.00	15.00	2.00
	offset	1.50	2.00	1.00

Case 1: Variations in Incident Beam Angles

To begin, I tested variations in the angle of the sample relative to both collinear incident beams. Within our lab we utilize reflection geometry, so all experiments herein will be modeled respectively. The test spans the incident angles from 50° to 65° with a unit change of 5° between spectra, which is within the typical range for a VSFG

reflection geometry experiment. The real and imaginary components of the fitted refractive indices for each polarization combination are shown overlaid with the "true" components determined by IR VASE in Figure 20. While the *ppp*, *ssp*, and *pss* provided good matches to the κ spectral shape, only the *ppp* had an η offset close to the true value. It is important to recognize that the n and $\chi^{(2)}$ fitting parameters were optimized to best fit the simulated VSFG spectra, not the ellipsometric η and κ values. Hence, the fact that the spectra are reminiscent of the starting index spectra highlights that their features are necessary to reproduce the VSFG spectra and cannot be simply compensated by changes in $\chi^{(2)}$ parameters.

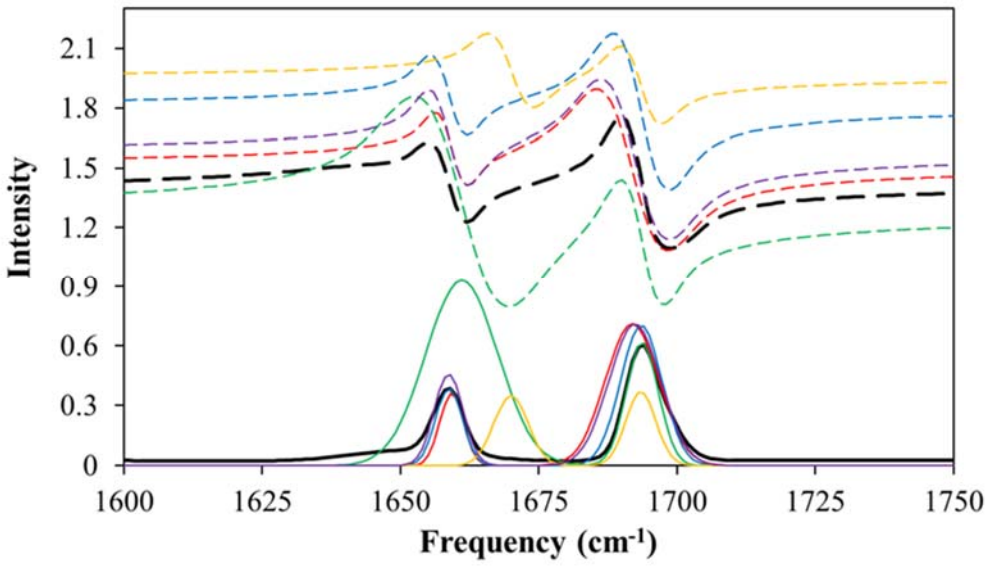

Figure 20. Real (dashed) and imaginary (solid) refractive indices of PTCDI (black) and the arbitrary material using the *ppp* (red), *ssp* (blue), *sps* (green), *pss* (orange) polarization combinations, while the results from the tandem fit are shown in purple.

Table 10. For the beam angle experiment, the optimized parameter values for the center frequency, ν (cm^{-1}), the amplitude, a, and the HWHM, Γ (cm^{-1}), for the lower, l, and higher, h, frequency modes for the inner, b, and outer, t, resonant responses and refractive indices for the four polarization combinations fitted individually and with a shared set of refractive indices, along with the sum of the residuals squared for the real and imaginary components.

		Individual				**Global**				
		ppp	***ssp***	***sps***	***pss***	***ppp***	***ssp***	***sps***	***pss***	**tandem**
Resonant Terms	ν_l^t	1656.00	1655.77	1655.24	1654.41	1653.43	1653.67	1655.46	1655.04	-
	a_l^t	0.118	0.117	0.092	0.094	0.110	0.134	0.081	0.103	-
	Γ_l^t	7.90	12.52	7.06	6.79	6.08	5.08	5.75	6.76	-
	υ_h^t	1686.57	1687.32	1687.92	1687.75	1686.27	1686.42	1683.46	1687.90	-
	a_h^t	0.097	0.082	0.093	0.109	0.104	0.127	0.051	0.106	-
	Γ_h^t	5.52	5.00	6.83	7.02	6.16	5.01	7.71	6.73	-
	ν_l^b	1651.62	1652.08	1652.60	1655.01	1654.95	1652.64	1651.98	1650.52	-
	a_l^b	0.093	0.157	0.109	0.142	0.091	0.104	0.112	0.078	-
	Γ_l^b	5.98	6.46	6.92	10.48	5.82	5.86	7.49	7.61	-
	υ_h^b	1685.22	1685.22	1684.98	1683.66	1687.23	1685.27	1686.71	1682.72	-
	a_h^b	0.126	0.167	0.104	0.021	0.103	0.102	0.145	0.056	-
	Γ_h^b	8.15	6.47	7.08	5.08	7.14	6.52	6.71	7.10	-
Indices Terms1	$\nu_{n,l}$	1659.25	1658.78	1661.11	1670.00	-	-	-	-	1657.82
	$a_{n,l}$	0.363	0.386	0.932	0.350	-	-	-	-	0.490
	$\Gamma_{n,l}$	2.50	2.83	7.62	3.60	-	-	-	-	3.74
	$\upsilon_{n,h}$	1691.90	1693.53	1693.72	1693.46	-	-	-	-	1693.04
	$a_{n,h}$	0.713	0.704	0.615	0.370	-	-	-	-	0.602
	$\Gamma_{n,h}$	5.64	4.41	3.44	3.21	-	-	-	-	4.86
	offset	1.51	1.80	1.28	1.95	-	-	-	-	1.46
Resids.	κ	1.13	0.34	5.85	1.94	-	-	-	-	0.83
	η	2.66	23.95	8.51	46.12	-	-	-	-	4.84
	$\eta + \kappa$	3.79	24.30	14.36	48.07	-	-	-	-	5.68

In Table 10**,** the squares of the residuals between the true and fitted indices are summed as a measure of how well the refractive index measured by ellipsometry is recovered by globally fitting VFSG data. Also shown are the results to the resonant fits. Since the real component is calculated from the imaginary, then added to a fittable offset, a lower residual sum for the κ value indicates a closer alignment with the spectral shape of both terms, while the residuals for the η value are also impacted by the offset position of the real spectra. All VSFG spectra were fit incredibly well, however, there was some variance of error in refractive indices with polarization. As mentioned previously, we do not expect a perfect fit without additional peaks in the imaginary spectrum. Isolating the IR VASE-measured indices and fitting them with just two Gaussian peaks, the lowest error possible for the imaginary spectra is 0.14, while the Kramers-Kronig transformed imaginary with an offset of 1.41 results in 0.06 for a minimum of the residuals for the real spectra, so the best fit cannot have a sum of residuals squared of zero.

The remaining polarization combinations had varied displacements from the true value, ranging from 1.28 for *sps* to 1.95 for *pss* (Table 10). A mismatch in the added offset term increases the overall error, as seen in the η residuals. Changes in this offset can have a large effect on the VSFG intensity output, so this term should not be overlooked. The excellent performance of the *ppp* fit may be because the *ppp* signal has contributions from four $\chi^{(2)}$ tensor elements while the remaining three polarization combinations are only described by a single element. The *ppp* polarization combination offers experimental advantages as well. Overall, the *ppp* response is usually the most intense of all the available polarization combinations. This increases the signal to noise, yielding cleaner, more easily fit spectra. Additionally, the projection of the *p* polarized IR

pulse onto the *z* axis within the vibrationally active interfacial sheet is more sensitive to the refractive angle, which is itself dependent on the indices. The second optimization method was also employed, using all four polarization combinations in tandem to fit the refractive indices. This resulted in a low error output similar to the *ppp* optimization, although the individual *ppp* polarization still performed better in this first case.

Case 2: Variations in Visible Beam Frequency

Many VSFG setups employ a tunable visible laser beam that offers another means to systematically vary the sum frequency response. In the second case, I simulated the spectra using a range of 790 to 805 nm with a change of 5 nm between spectra, and then fitted the spectra globally using the individual polarization combination and tandem methods described above. The resulting real and imaginary refractive index spectra for both methods are overlaid on the ellipsometrically determined spectra in Figure 21. Qualitatively, there is a smaller spread in the real spectra obtained from the fit, but worse agreement in the imaginary spectra compared to the true spectra.

Again, I used the sum of residuals squared to quantify the goodness of fit. The κ summed residual values in each test are lower than the resulting errors in Case 1 (Table 11), however, the solution to the offset term in η again had a large variability, spanning from 1.08 for *ppp* to 1.52 for *ssp*. Additionally, I observed significant errors in the resonant terms, for example, the fitted amplitude for the lower frequency mode at the top interface (7×10^{-4}) is near-zero in the *ssp* fit, relative to the true value of 0.1 (Table 11). The placement of the fitted resonant peaks when approached through both methods was

not always consistent, at times resulting in an outer center frequency shifted lower than the inner, opposite of the simulated trend.

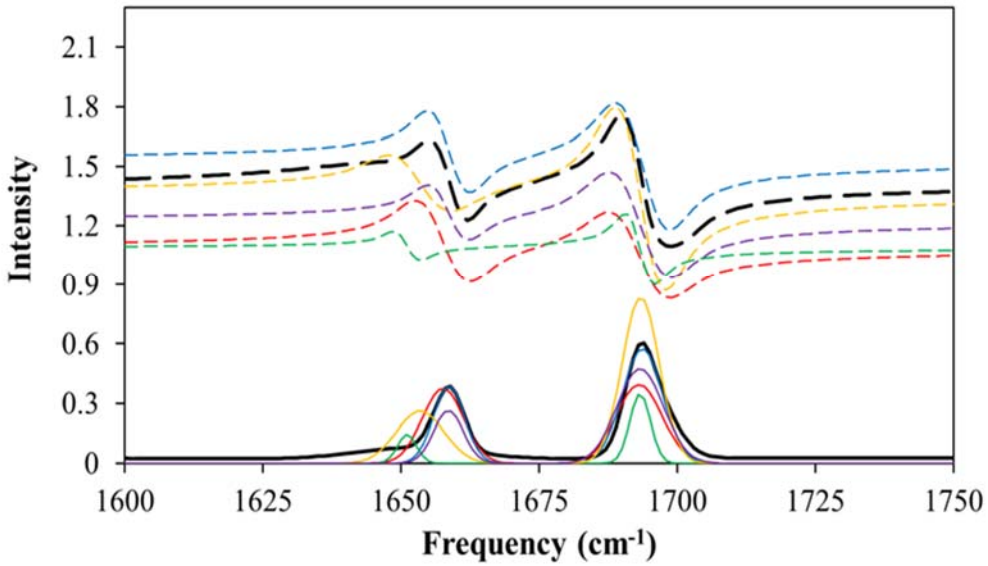

Figure 21. Real (dashed) and imaginary (solid) refractive indices of PTCDI (black) and the arbitrary material using the *ppp* (red), *ssp* (blue), *sps* (green), *pss* (orange) polarization combinations, while the results from the tandem fit are shown in purple.

Case 3: Variations in underlying oxide thickness

The next simulations explored changes made to the samples rather than the input beams. First, I simulated VSFG spectra for a series of samples with a variable oxide thickness beneath the vibrationally active PTCDI layer, spanning from 50 to 200 nm in 50 nm increments. The fit was approached with the assumption that a change in the oxide thickness would not change the oxide surface interactions with PTCDI, which could lead

Table 11. For the visible wavelength experiment, the optimized parameter values for the center frequency, ν (cm^{-1}), the amplitude, a, and the HWHM, Γ (cm^{-1}), for the lower, l, and higher, h, frequency modes for the inner, b, and outer, t, resonant responses and refractive indices for the four polarization combinations fitted individually and with a shared set of refractive indices, along with the sum of the residuals squared for the real and imaginary components.

		Individual				**Global**				
		ppp	***ssp***	***sps***	***pss***	***ppp***	***ssp***	***sps***	***pss***	**tandem**
Resonant Terms	ν_l^t	1653.94	1654.00	1654.82	1654.43	1653.53	1649.54	1650.75	1654.74	-
	a_l^t	0.082	0.067	0.085	0.111	0.106	0.001	0.154	0.101	-
	Γ_l^t	6.19	10.15	8.38	6.86	6.12	5.49	14.84	7.31	-
	υ_h^t	1686.65	1682.30	1683.09	1687.01	1685.50	1683.26	1687.17	1687.75	-
	a_h^t	0.080	0.038	0.027	0.097	0.097	0.012	0.050	0.104	-
	Γ_h^t	5.59	5.01	7.26	7.27	6.96	5.00	5.01	6.83	-
	ν_l^b	1652.42	1652.42	1652.61	1661.38	1657.00	1652.72	1653.03	1653.67	-
	a_l^b	0.060	0.117	0.117	0.026	0.056	0.068	0.097	0.120	-
	Γ_l^b	5.71	6.08	6.63	7.27	6.08	5.88	5.80	7.03	-
	υ_h^b	1687.68	1684.76	1686.22	1689.39	1686.32	1684.97	1686.10	1684.54	-
	a_h^b	0.071	0.116	0.158	0.125	0.067	0.067	0.194	0.087	-
	Γ_h^b	9.74	5.50	6.92	5.06	5.12	5.01	12.15	9.83	-
Indices Terms	$\nu_{n,l}$	1657.61	1658.70	1651.13	1653.50	-	-	-	-	1658.62
	$a_{n,l}$	0.375	0.386	0.145	0.261	-	-	-	-	0.264
	$\Gamma_{n,l}$	4.36	3.30	2.03	5.10	-	-	-	-	3.17
	$\upsilon_{n,h}$	1693.11	1693.73	1693.29	1693.40	-	-	-	-	1693.30
	$a_{n,h}$	0.393	0.574	0.347	0.834	-	-	-	-	0.473
	$\Gamma_{n,h}$	4.90	4.29	2.21	3.95	-	-	-	-	4.94
	offset	1.08	1.52	1.09	1.36	-	-	-	-	1.22
Resids.	κ	0.41	0.18	1.83	0.90	-	-	-	-	0.37
	η	16.59	2.08	17.40	1.11	-	-	-	-	5.58
	$\eta + \kappa$	17.00	2.26	19.24	2.00	-	-	-	-	5.95

to changes in $\chi^{(2)}$, so each of the resonant fitting parameters was still shared globally within each polarization combination. In general, the fitted indices show exceptional agreement with the true values in Figure 22, with the most faithful recreation of the indexed line shape and the most accurate η offset values, especially in the *ppp* and *pss* fits. Furthermore, there was little deviation of the $\chi^{(2)}$ resonant parameters from their true values. Table 12 confirms that the fitted η and κ spectra are quantitatively better than the fits obtained by varying beam parameters. Here we see that the *ppp* and *pss* combinations give very good agreement with the ellipsometric index spectra and the tandem fit is the best overall.

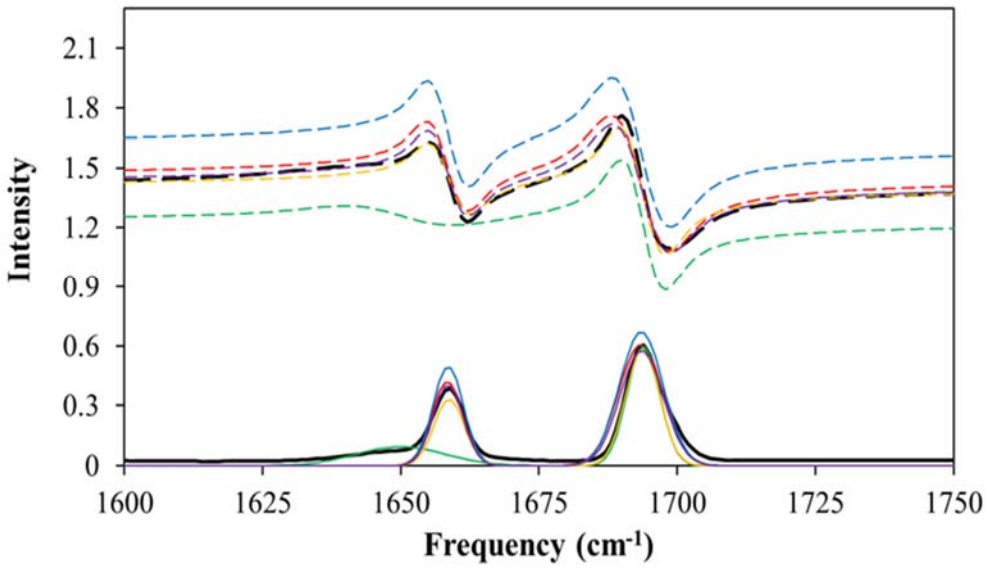

Figure 22. Real (dashed) and imaginary (solid) refractive indices of PTCDI (black) and the arbitrary material using the *ppp* (red), *ssp* (blue), *sps* (green), *pss* (orange) polarization combinations, while the results from the tandem fit are shown in purple.

Table 12. For the oxide thickness experiment, the optimized parameter values for the center frequency, ν (cm^{-1}), the amplitude, a, and the HWHM, Γ (cm^{-1}), for the lower, l, and higher, h, frequency modes for the inner, b, and outer, t, resonant responses and refractive indices for the four polarization combinations fitted individually and with a shared set of refractive indices, along with the sum of the residuals squared for the real and imaginary components.

		Individual				**Global**				
		ppp	***ssp***	***sps***	***pss***	***ppp***	***ssp***	***sps***	***pss***	**tandem**
Resonant Terms	ν_l^t	1654.51	1654.88	1654.64	1655.01	1654.68	1654.93	1654.97	1654.96	-
	a_l^t	0.109	0.127	0.101	0.100	0.105	0.100	0.093	0.098	-
	Γ_l^t	7.44	6.33	7.12	7.02	7.26	6.59	7.64	6.96	-
	υ_h^t	1687.26	1686.80	1687.86	1687.98	1687.34	1686.92	1687.52	1687.99	-
	a_h^t	0.104	0.128	0.101	0.099	0.102	0.103	0.062	0.103	-
	Γ_h^t	7.28	6.87	7.04	6.97	7.37	7.06	5.03	7.19	-
	ν_l^b	1652.85	1652.39	1652.06	1652.03	1652.70	1652.32	1652.81	1652.48	-
	a_l^b	0.097	0.128	0.099	0.100	0.095	0.099	0.102	0.114	-
	Γ_l^b	6.03	6.44	6.93	7.09	6.31	6.51	6.81	7.86	-
	υ_h^b	1684.86	1684.40	1685.05	1684.98	1684.94	1684.44	1685.52	1685.63	-
	a_h^b	0.096	0.122	0.100	0.100	0.095	0.097	0.168	0.084	-
	Γ_h^b	6.04	6.09	7.02	7.05	6.17	6.27	10.59	5.82	-
Indices Terms	$\nu_{n,l}$	1658.42	1658.58	1650.01	1658.75	-	-	-	-	1658.53
	$a_{n,l}$	0.421	0.497	0.095	0.332	-	-	-	-	0.403
	$\Gamma_{n,l}$	3.30	3.23	9.50	3.22	-	-	-	-	3.19
	$\upsilon_{n,h}$	1693.39	1693.49	1693.87	1693.73	-	-	-	-	1693.56
	$a_{n,h}$	0.606	0.671	0.599	0.581	-	-	-	-	0.577
	$\Gamma_{n,h}$	4.71	4.62	3.45	3.59	-	-	-	-	4.57
	offset	1.45	1.61	1.23	1.40	-	-	-	-	1.42
Resids.	κ	0.24	0.33	0.69	0.26	-	-	-	-	0.20
	η	0.42	6.30	5.55	0.08	-	-	-	-	0.11
	$\eta + \kappa$	0.65	6.63	6.23	0.34	-	-	-	-	0.31

Case 4: Variations in vibrationally-active layer thickness

Finally, I simulated changes in the VSFG-active organic layer thickness. Similar to the oxide alteration, I assume no change to the interfacial packing as the material layer is changed. The fitted refractive index spectra are overlaid on the ellipsometric spectra in Figure 23. There is generally good agreement between the spectra, although there is clearly more of a spread in the fitted spectra for the real components. This is borne out in the summed residuals squared in Table 13, which are generally very low but show a jump in the real portion of the *pss* fit. Interestingly, although *pss* fails to approximate the offset value similar to the other polarizations, the resonant fit parameters are still close to the true values (Table 13). Similar to Case 1, *ppp* and tandem fits had the lowest errors.

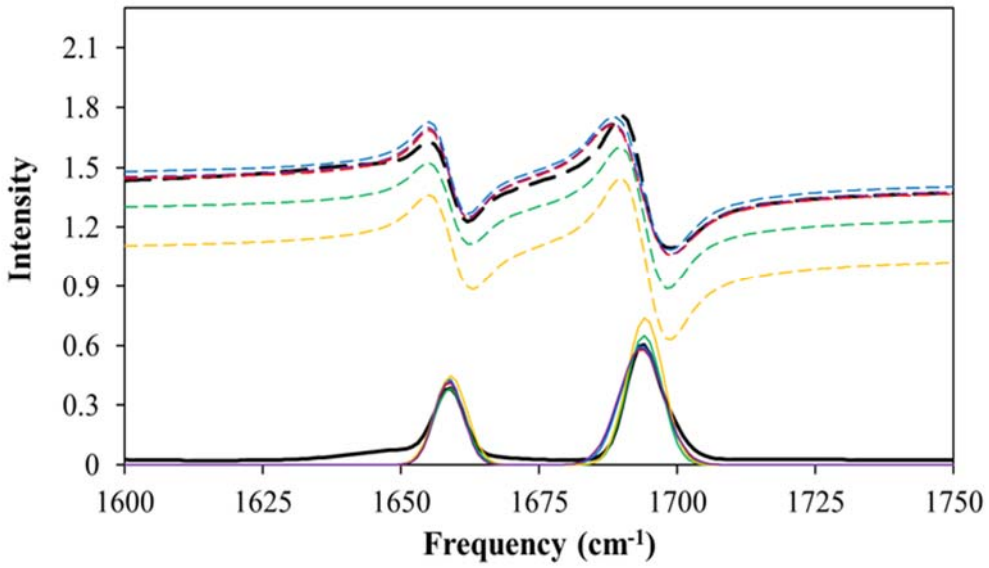

Figure 23. Real (dashed) and imaginary (solid) refractive indices of PTCDI (black) and the arbitrary material using the *ppp* (red), *ssp* (blue), *sps* (green), *pss* (orange) polarization combinations, while the results from the tandem fit are shown in purple.

Table 13. For the organic thickness experiment, the optimized parameter values for the center frequency, ν (cm^{-1}), the amplitude, a, and the HWHM, Γ (cm^{-1}), for the lower, l, and higher, h, frequency modes for the inner, b, and outer, t, resonant responses and refractive indices for the four polarization combinations fitted individually and with a shared set of refractive indices, along with the sum of the residuals squared for the real and imaginary components.

		Individual				**Global**				
		ppp	***ssp***	***sps***	***pss***	***ppp***	***ssp***	***sps***	***pss***	**tandem**
Resonant Terms	ν_l^t	1655.03	1655.02	1655.04	1655.03	1655.02	1655.09	1655.04	1655.03	-
	a_l^t	0.100	0.104	0.099	0.100	0.101	0.100	0.104	0.100	-
	Γ_l^t	6.76	6.39	7.01	7.01	6.77	6.42	7.37	7.02	-
	υ_h^t	1687.47	1686.97	1688.00	1687.99	1687.48	1686.87	1687.99	1687.95	-
	a_h^t	0.099	0.105	0.100	0.100	0.100	0.101	0.098	0.100	-
	Γ_h^t	6.94	6.65	6.99	6.99	6.95	6.59	6.86	6.92	-
	ν_l^b	1652.31	1652.34	1652.00	1651.97	1652.32	1652.37	1651.88	1652.05	-
	a_l^b	0.100	0.104	0.100	0.102	0.100	0.101	0.101	0.103	-
	Γ_l^b	6.97	6.68	7.03	7.07	6.93	6.75	7.11	7.30	-
	υ_h^b	1684.65	1684.46	1685.02	1685.05	1684.68	1684.37	1685.04	1685.42	-
	a_h^b	0.095	0.099	0.100	0.101	0.096	0.095	0.097	0.095	-
	Γ_h^b	6.28	6.24	6.99	7.01	6.33	6.12	6.75	6.95	-
Indices Terms	$\nu_{n,l}$	1658.66	1658.61	1658.78	1658.99	-	-	-	-	1658.64
	$a_{n,l}$	0.416	0.432	0.385	0.447	-	-	-	-	0.422
	$\Gamma_{n,l}$	3.08	3.10	3.33	3.44	-	-	-	-	3.09
	$\upsilon_{n,h}$	1693.46	1693.57	1693.98	1694.17	-	-	-	-	1693.47
	$a_{n,h}$	0.582	0.599	0.651	0.740	-	-	-	-	0.587
	$\Gamma_{n,h}$	4.71	4.45	3.74	3.84	-	-	-	-	4.68
	offset	1.41	1.44	1.27	1.07	-	-	-	-	1.42
Resids.	κ	0.22	0.21	0.19	0.28	-	-	-	-	0.22
	η	0.12	0.29	2.96	17.76	-	-	-	-	0.13
	$\eta + \kappa$	0.34	0.50	3.15	18.05	-	-	-	-	0.36

4.4. Experimental Application

Throughout the four cases that were explored above, I observed no clear trends in the error of the individual polarizations, though it can be said that the tandem fits resulted in consistently low error values in relation to the individual best performers of each experiment. Consequently, whenever possible multiple polarization combinations should be used in tandem to experimentally fit the refractive indices of a material. It was observed that the errors in the fitted refractive indices were consistently better for Cases 3 and 4 when the sample layer thicknesses were varied. The origin of this improvement is most certainly that the spectral differences that can be achieved with the film thicknesses available in most laboratories are greater than those achieved with beam properties. The more distinct the VSFG spectra are as a parameter is varied, the more constrained the fitting parameters will be to end at the global minimum.

To simulate the datasets for these four cases, within a given polarization combination the resonances were unchanged but the transfer matrices were not fixed. The total intensity, I, of a polarized VSFG signal is proportional to the square of all summed products of each interfacial response, $\chi_v^{(2)}$, and their corresponding transfer matrix, T_v, plus the nonresonant response (equations 50-51). In this nomenclature, v is the active planar interface formed by the vibrationally active material the surrounding media (Figure 5). Each total transfer matrix is equal to the product of the individual transfer

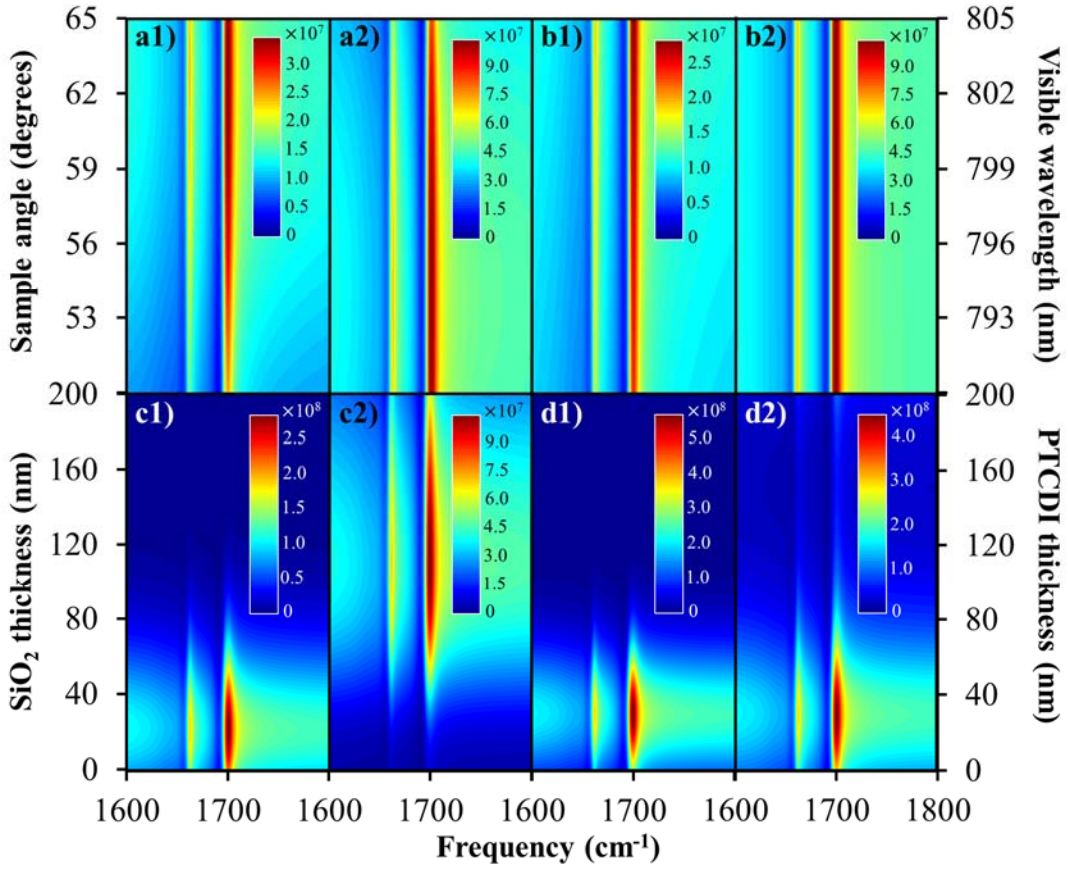

Figure 24. Top (1) and bottom (2) transfer matrix intensity (inset scales) for the *ssp* experiment of sample angle (a), visible wavelength (b), oxide thickness (c), and organic thickness (d).

matrices for each beam and each beam transfer matrix term calls upon specific matrix elements for different polarization combinations. Full discussion of elemental selection can be found in equations 50-51. These transfer matrices are built using the refraction and phase matrices discussed in Chapter 1. I hypothesized that the amount of change between the transfer matrices as a parameter is varied within a given experiment was inversely related to the amount of error in the optimization. To visualize this, I calculated the total

transfer matrix at each interface in each experiment, and multiplied it with its complex conjugate to place it in real space, allowing visualization of the changes. In Figure 24, the transfer matrices from both interfaces in the *ssp* models are shown for each experiment. Qualitatively, the changes between transfer matrices as the material thicknesses are varied are much larger than the relative changes as the visible wavelength is scanned. As a result, the thickness experiments to have the lowest error, indicating correlation between the magnitude of variations in the transfer matrix and the quality of the fitted refractive indices.

With the range of oxide thicknesses proven to be the most effective simulation above, along with the experimental ease provided by the measurement with our setup, I chose to mimic the test experimentally. Oxide films were grown thermally onto the substrates across a range of 59 through 330 nm, and measured in *ppp* and *ssp*. The *sps* and *pss* had a signal to noise value too low to assist the optimization. Though the true IR VASE determined indices have been used in the simulations, the resolution of the VSFG instrument (through use of an etalon to shape the visible spectrum to a HWHM of 7.36 cm^{-1}) alters the line-shape of each resonant response. Thus, the Gaussian IR VASE real and imaginary spectra were convolved with a Lorentzian line-shape to match our spectral resolution. The refractive indices were modeled by a Lorentzian line shape during the optimization. The convolved and fitted indices are shown in Figure 25. When fitting, the amplitudes were allowed to be unique for each data set, while the widths and frequency centers were shared globally within each individual polarization combination. Laser flux, polarization-dependent optical losses, and sample inconsistencies may yield discrepancies between data sets that would impart unnecessary error with too many

shared values forced upon it. Additionally, description of each polarization combination was unique, as molecular organization can lead to varying nonlinear susceptibilities since ordered vibrational modes may have different responses for different combinations. The parameters are listed in Table 14.

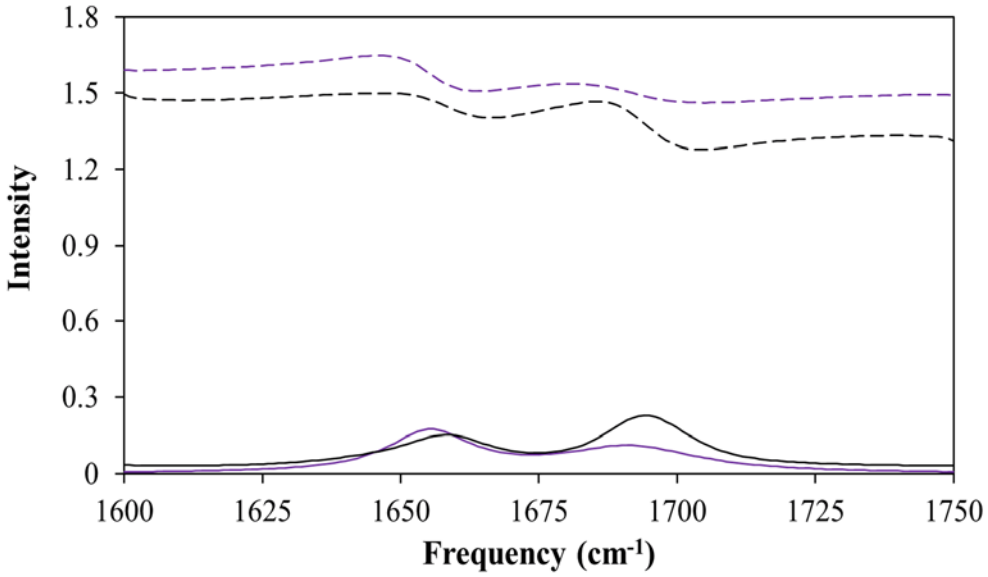

Figure 25. Real (dashed) and imaginary (solid) refractive indices of PTCDI convoluted with a Lorentzian (black) and the experimental fit (purple).

While the residuals are low (κ = 0.37, η = 2.63), we still observe differences in the refractive index spectra. The lower frequency mode is nearly identical to the convolution, though the higher frequency mode is lower in both amplitude and frequency. While the differences may be minimized through the addition of more samples and

Table 14. For the proof-of-concept experiment, the optimized parameter values for the center frequency, ν (cm^{-1}), the amplitude, a, and the HWHM, Γ (cm^{-1}), for the lower, l, and higher, h, frequency modes for the inner, b, and outer, t, resonant responses and refractive indices for the four polarization combinations fitted individually and with a shared set of refractive indices, along with the sum of the residuals squared for the real and imaginary components.

		Individual		**Global**		
		ppp	***ssp***	***ppp***	***ssp***	**tandem**
Resonant Terms	ν_l^t	1654.00	1656.00	1652.00	1652.29	1655.75
	a_l^t	0.010	0.100	0.000	varied	varied
	Γ_l^t	10.00	15.00	5.00	7.19	6.53
	υ_h^t	1686.00	1688.00	1684.00	1685.31	1687.99
	a_h^t	0.010	0.100	0.000	varied	varied
	Γ_h^t	10.00	15.00	5.00	5.69	6.25
	ν_l^b	1654.00	1656.00	1652.00	1652.18	1652.16
	a_l^b	0.010	0.100	0.000	varied	varied
	Γ_l^b	10.00	15.00	5.00	9.82	5.07
	υ_h^b	1686.00	1688.00	1684.00	1688.00	1685.00
	a_h^b	0.010	0.100	0.000	varied	varied
	Γ_h^b	10.00	15.00	5.00	5.03	7.48
Indices Terms	$\nu_{n,l}$	1655.50	1658.00	1653.00	-	-
	$a_{n,l}$	0.100	1.000	0.000	-	-
	$\Gamma_{n,l}$	12.00	20.00	5.00	-	-
	$\upsilon_{n,h}$	1692.50	1695.00	1690.00	-	-
	$a_{n,h}$	0.100	1.000	0.000	-	-
	$\Gamma_{n,h}$	12.00	20.00	5.00	-	-
	offset	1.50	2.00	1.00	-	-
Resids.	κ	1654.00	1656.00	1652.00	1652.29	1655.75
	η	0.010	0.100	0.000	varied	varied
	$\eta + \kappa$	10.00	15.00	5.00	7.19	6.53

polarization combinations, there may be innate differences between the bulk indices, and the planar interfacial sheet. The continuity of the refractive indices at the 2D boundary permits values with the character of both materials comprising it.[170-174] In theory, VSFG could provide an unparalleled tool to resolve the refractive indices at the buried planar sheet without the need for optically thin films, though more data sets than presented here would likely be necessary to perform a confident optimization. This measurement could be realized by altering the fitting routine, separating the bulk refractive index from the interfacial sheets.

4.5. Conclusions

In this chapter, I have presented a novel method for determination of the refractive indices. While the results are not as sensitive or accurate as those provided through ellipsometry, the technique offers the potential solution of the indices at the planar interfacial sheets, a means inaccessible to ellipsometry. Through simulation, we found a series of samples with a change in the oxide thickness provided the highest sensitivity to the refractive indices, best matching the line shape and offset value. When applied to experimental data, the resultant fit, while some differences were present, still had a similar shape. A wider collection range, inclusion of more polarization combinations, or a mixture of several geometric or sample changes could increase the dependency on the refractive indices while fitting, likely improving the fit.

4.6. Acknowledgements

Thank you to JA Woollam for discussion of common usage line shapes in IR VASE. Portions of this work were conducted in the Minnesota Nano Center, which is supported by the National Science Foundation through the National Nanotechnology Coordinated Infrastructure (NNCI) under Award Number ECCS-2025124. Work was assisted by Zhihao Wu.

CHAPTER 5: EXTENDED MODELING: IMPACT OF THE INTERFACIAL REFRACTIVE INDICES

5.1. Introduction

The optical properties of thin films are responsible for a wide-array of technologies and applications. Careful understanding of the interfaces formed by materials in layered stacks is of great importance. Often the refractive indices at a material boundary are assumed to be discrete. Certainly, the previous chapters document usage of a modeling program assuming just that. However, the electric and magnetic fields are required to vary continuously at interfaces between materials, and in accordance, the refractive index should also rapidly vary. Furthermore, many relevant technologies utilize nanoscale graded-index films to achieve tunable and efficient optical properties. These can include monolayer assemblies such as organized phospholipids, metals, or small organic molecules, layered nano-films, or 3D surface structures.

Spectroscopic ellipsometry finds abundant usage in resolution of thickness, material properties, and refractive index of films. However, difficulty arises in the solution of ultrathin films; at atomic and molecular scales the thicknesses and refractive indices become strongly correlated.[175] Further complication can arise when the thickness of the interfacial region defined by two adjacent layers is relevant to the total system thickness. Modeling applications can be leveraged to approximate the gradient. Much work has gone into the understanding of the SiO_2/Si interface using ellipsometry. For example, Kalnitsky was able to fit experimental data by modeling the interface with a

series of stratified sublayers, grading the refractive index across a variety of transition thicknesses.[174] When measuring silica films with oxide thickness between 1.5 and 7.5 nm, an interfacial region of ~1 nm was resolved.[175-176] Others have observed identical trends.[170, 177-178] Similar changes in the refractive index of Al_2O_3 films have been observed.[172]

Intentional manipulation of propagating light through layered assemblies has found success in many optical markets. These often utilize SAMs with refractive indices between the surrounding media. Others opt for graded index films with compositional changes or a nano-layering structure, where material concentration is changed throughout some depth. For example, by fluctuating the O_2 flow during SiO_xN_y deposition while the N_2 bombardment rate is held constant, one can continuously change the stoichiometry, and by extension, the refractive indices.[179-180] Titania deposition parameters can yield similar results.[173] Using oblique angle deposition with different layer ratios of TiO_2 and SiO_2, Kuo and coworkers found the inclusion of a high number of multilayer stacks with a graded-index profile demonstrated high transmission values.[181] Lensing can be optimized using 3D structures, such as towards efficient optical coupling between a silicon chip and optical fiber.[182] Nanopinnacles, or "moth-eye" parabolic structures can achieve superior antireflection properties and find use in a range of optical technologies.[183-185] These structures promote continuous refraction, or bending of the light, opposed to reflection.[33] While moth-eye structures generally do not allow internal reflections, the layered assemblies can require a thin film treatment of the layers to account for interference effects.

Modeling of these graded index films or continuous interfaces requires extension beyond the simple Fresnel terms. As considered through a sum frequency lens applying the previously discussed fitting routine (Figure 5), for the simple interface present between two bulk materials where one is a nonlinear media, the general modeling system would include an interfacial region. The different conventions available to describe the interfacial region are of great importance, as the dipolar sum frequency response is generated exclusively from these interfaces. Discussion is presented below documenting these approaches. For an interstitial layer, like a vibrationally active SAM deposited between two bulk materials, one could forego the bulk nonlinear layer, instead allocating the entirety of the active medium thickness to the continuous interfacial region. Arbitrary graded index structures can employ a model to describe the variation of the index by dividing an inhomogeneous medium into a series of homogenous sublayers.[179, 186] Each layer is treated with its own dielectric constant. Homogeneity is among the assumptions when using transfer matrix formalism, and segregation of the heterogeneity into a number of discrete homogeneous layers with a continuous grade may function as an approachable work-around. Within the initial work completed here I focus on the simple interface formed between two adjacent materials.

Discussion of theory, both through SHG and SFG, has often given a nod to the continuity, proposing an interface with distinct refractive indices, or even offering an integral over the transition region.[22, 26] In practice the polarized sheet is often infinitesimally thin and approximated using the macroscopic bulk dielectric constants of the neighboring semi-infinite contacting media.[7, 12, 187] When set as equivalent to either surrounding media, the problem is effectively reduced down to a two phase model (each

"phase" is a bulk medium). If the interfacial indices are unique, the problem defines a modified two phase model. When studying SAMs using SHG, Eisert treated the data using a three phase model (the third being the interface treated as a proper layer), a two phase model, and a macroscopic local field corrected two phase model. The base treatment with a simple two phase model showed best agreement.[188] Others still have taken different approaches towards the treatment of the interface as unique. Foregoing the infinitesimally thin interfacial layer model in favor of a three phase thin film model, Wang found that simply averaging the surrounding indices to arithmetically calculate the interfacial indices supplied good agreement with data.[189] This approach acknowledges the ability of the interfacial region to produce internal reflections. McGilp described amphiphilic Langmuir-Blodgett films with a three phase model[190] following the derivation of Zhang.[191] This approach assigns the nonlinear interfacial layer an isotropic linear dielectric constant. Taking it a step further, Munn and Shabat concluded that overestimation of the local field factors using Langmuir-Blodgett films can occur if the interfacial monolayer is not further subdivided into multiple layers.[192]

However, this is still simplifying the potential anisotropic local field effects arising from the transitional monolayer. Using liquid crystals, Shen theorized that treatment of the sheet with a macroscopic model fails to fully define a monolayer, and requires microscopic local field factors.[7, 9] Properties such as dipole screening effects are dependent on the structure of the interfacial monolayer.[193] As noted by Zheng when using a microscopic molecular optics approach, if an interfacial film is thin enough it will not have any significant effect on the macroscopic reflection and transmission coefficients, and thus a three-layer model where the submonolayer or monolayer interface is treated as

a layer is not applicable. This treatment can be applied to a second interfacial monolayer as well.[193] One might even assume a third layer would not likely provide any meaningful change to the linear macroscopic dielectric constant, thus, it may be ignored, through this derivation. Microscopically, the Fresnel terms can be adjusted by the local field factors, where the effective dielectric constant of the interface is equal to a ratio of both the parallel and perpendicular anisotropic local field factors.[26, 193] The parallel component is identical for the *x* and *y* directions, while the perpendicular component accounts for the *z* direction. This formulation leads to treatment of the interface instead as a modified microscopic two-phase system, where the interface is impactful, and given a unique effective dielectric constant which need not be an average of the surrounding media.

Examination of the literature shows an extensive range of disagreement in the treatment of the interface, where different systems appear to require different approaches. Thus, the following pages document my initial work towards a unification of the reported disparity within a general modeling routine. This chapter will serve as a collection of observations when using transfer matrix formalism to treat the interfacial refractive index continuity as a series of discrete layers within the sum frequency generation experiment, simulating the two phase result, along with the three phase, four phase, etc. while considering different interfacial thicknesses. Extrapolation between the integer phase outputs would provide the approximate values to a modified-phase experiment. Affording the routine a fittable parameter (which could also be set to a constant), where the new term identifies the integer or non-integer phase value, would provide a routine capable of handling any system. This extension will be completed using the aforementioned modeling routine with changes discussed below. The simulations presented herein are

devised to address a simple vibrationally active interface between two materials, but could be extended to model sum frequency generation of graded-index films or any monolayer assembly as well.

5.2. Model Description

The modeling program used in this work has been described previously in Chapter 1, and is constructed using transfer matrix formalism. Within the chapter, the interfacial boundaries formed by the vibrationally active material and surrounding materials are split by an increasing number of vibrationally active layers, where the refractive index is graded across it. The general geometry is displayed in Figure 26. The transfer and phase matrices are similar in build to the system borne out in Figure 5. There are several points of discussion in Figure 26. First, for the general $N \geq 3$ inter-layer system shown here (though $N \in \{0,1, \dots, \infty\}$ is allowed), there are $N + 1$ iterations necessary to sample all interfaces adjoined by a vibrationally active layer. The upper interfacial region, u, is iterated over from the top-down, while the lower region, l, is iterated from the bottom-up. Thus, for iteration $m = N + 1$ both boundaries formed by the central vibrationally active bulk layer will be transferred to, where the sum frequency signals will be generated and transmitted back out. The linear refractive index gradient across the upper interfacial region for the top transfer matrix system is applied using the following for each layer, x:

$$n_{u_x} = n_{v-1} + x\left(\frac{n_v - n_{v-1}}{N+1}\right). \tag{56}$$

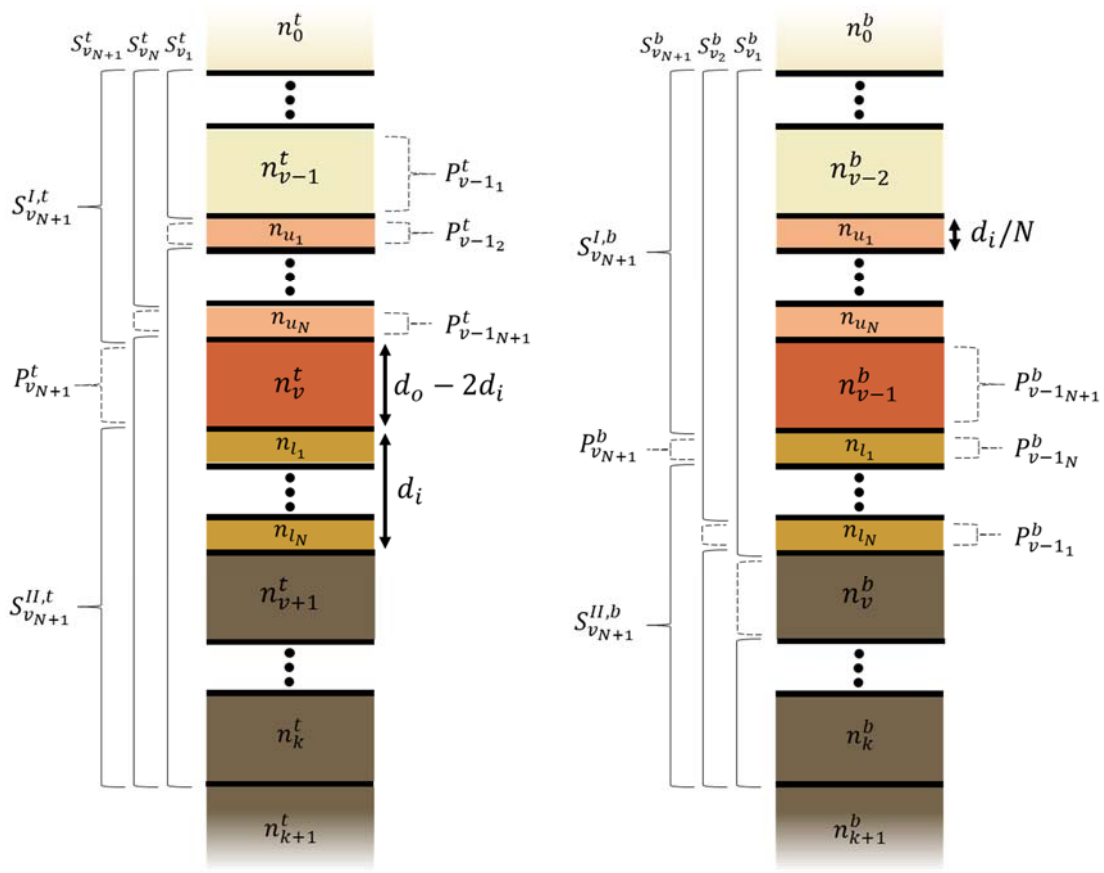

Figure 26. Interfacial definition of the described transfer matrix terms for the top and bottom interfaces of an arbitrary system consisting of a single vibrationally active layer (orange) with a general number of distinct layers above (tan) and below (dark brown) where the vibrationally-active interface is split into N discrete layers.

The interfaces formed by non-vibrationally-active layers are not split and graded within this work. Their presence may affect the nonresonant background, but no background is afforded in any simulations presented. The thickness of the interfacial region, d_i, is an adjustable parameter within the model. Any depth given to the boundaries is taken from the main vibrationally active layer, d_o, preserving the total

thickness of the stack (i.e. 100 nm active layer with 0 nm boundaries vs 90 nm active layer with 5 nm boundaries). The thickness of a single layer within the split interfacial section is then d_i/N. This presents two special cases that are non-intuitive. In the first, $N = 0$ while $d_i > 0$. With no splitting of the interface, the entirety of the region will retain its original character, being treated as a simple two phase system. This yields an identical result in all cases to $N = 0$ and $d_i = 0$. In the second, $N > 0$ while $d_i = 0$. There are a series of refractions then occurring over null space, akin to the infinitesimally thin interfacial assumption. Though this case is merely an approximation, we retain the data points as the region between 0 and 1 nm is of interest and the trend between them is mathematically preserved as the model considers all boundaries to be 2D, thus requiring no thickness.

Design of the system used to model the impact of the interfaces is similar to that used in Chapter 4, where the top media is air, the active layer is PTCDI, and the bottom layer is a silicon substrate with a thermal oxide layer on top. The PTCDI and SiO_2 layers within the base model are set to 100 nm each, while any thickness given to the boundaries is removed from the PTCDI layer. The incident beams are input at angles of 55° for the visible and 60° for the IR source. Unless stated otherwise, monochromatic input sources were used where the IR source was set to 1750 cm^{-1}, and the visible source was placed at 800 nm. Nonlinear susceptibilities were modeled by two peaks at each interface, where the center frequencies were set to 1650 and 1700 cm^{-1}, the amplitudes to 1, and the half widths at half max to 10 cm^{-1}. No shift was imparted between the interfacial signals, and no nonresonant response was included. Finally, all measurements were simulated in reflection geometry.

5.3. Results and Discussion

First, I examined the impact of the number of interfacial layers (N) as the frequency is scanned. This was done through the complex reflection and transmission terms described by equation 36 for the total system, S. Of note, when considering the total system, any iteration value, m, will yield an identical response as the subsystem terms will vary, but their accumulation negates the layer selection. The thickness of the interfacial region (d_i) is set to 5 nm. Shown by Figure 27, there is a meaningful dependence on the frequency and number of layers used to split apart the interface. The frequencies selected were chosen due to the available solved refractive indices for PTCDI.

As the interface is split, going from the two phase model ($N = 0$) to $N > 0$ values for the $N + 2$ phase models, there is a change in the measured response. Additionally, at higher frequencies within the visible region, the amount of change is even greater. When examining the reflection terms, for the IR frequencies, an increase from the two phase to the three phase model ($N = 0$ to 1) yields a percent change typically around <1%, while the visible frequencies are between 1 and 50%. For the $N = 1$ to 2, IR frequencies have a typical percent change between 0.0002 and 0.03%, while the visible frequencies display a change of 0.03 to 0.35%. The change going between subsequent terms decreases further, in a near exponential fashion. For the transmission terms, the changes are even less. Thus, for the total system picture, only the addition of a single interfacial layer is crucial, as anything further may put unnecessary strain on the computation since the change in

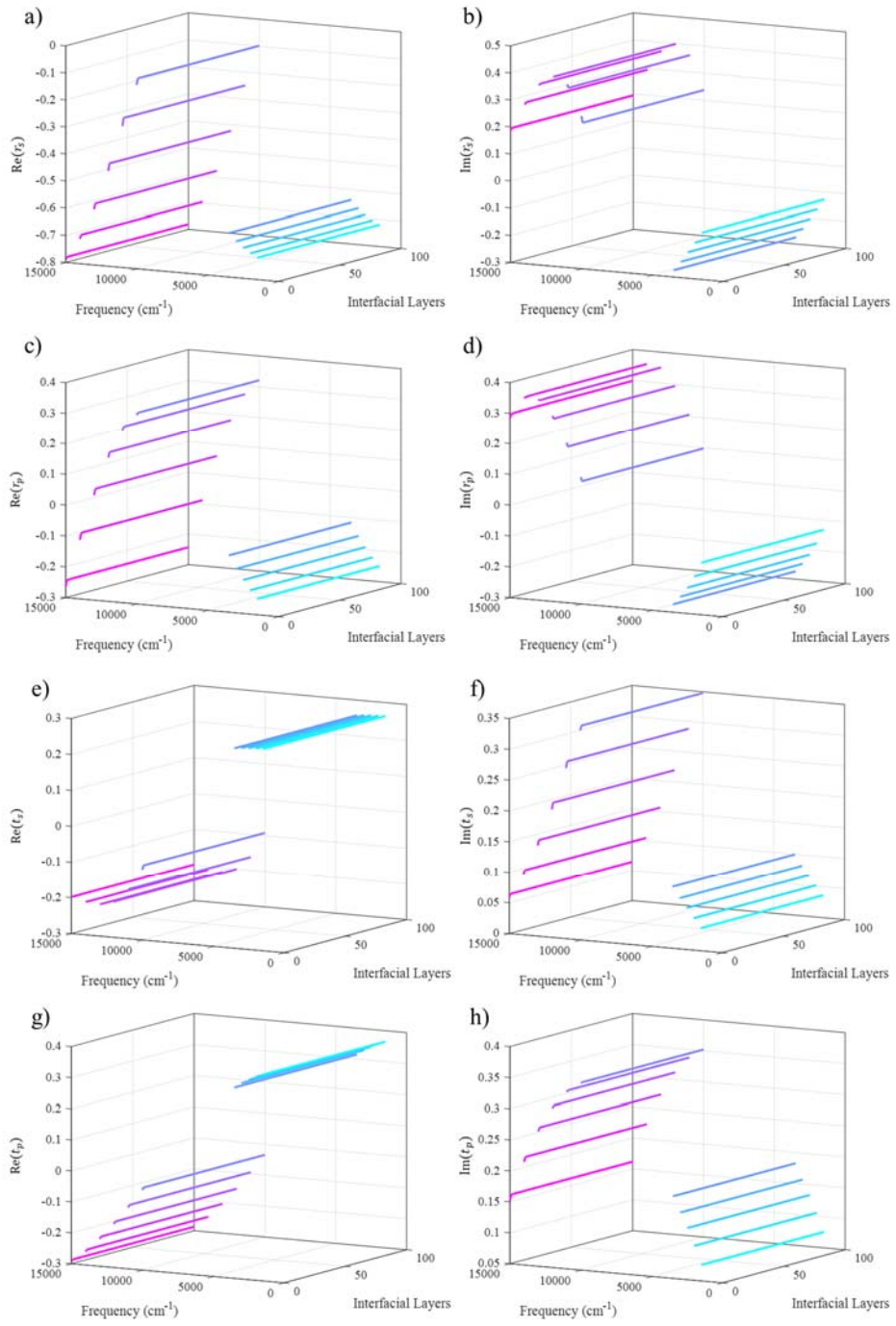

Figure 27. Real (a,c,e,g) and imaginary (b,d,f,h) reflection (a-d) and transmission (e-g) values for an s (a-b,e-f), and p (c-d,g-h) polarized input beam. Frequencies used are (from blue to purple) 1500, 2000, 2500, 3000, 3500, 10000, 11000, 12000, 13000, 14000, and 15000 cm^{-1}.

results is negligible. Additionally, treatment of the interfacial region in the area between the two and three phase models is of the upmost importance. I posit that extrapolation between the two points will yield the possible outcomes for a modified two phase model, though examination and determination of the curve connecting the two will be reserved for future studies.

Further, there is a clear dependence on the polarization selected. Interestingly there is a large-scale oscillation as the frequency is scanned, in both the real and imaginary responses. Going forward a baseline frequency off-resonance will be used (1750 cm^{-1}). While on-resonance the trends would be present, but to different extents and even directions. Through typical modeling, ellipsometric calculations assume a discrete boundary ($N = 0$). As Figure 27 shows, under the lens of transfer matrix formalism, there could be an impactful, but still small change if at least a single median layer is included. To better understand the overall impact of thickness on change, the same approach was utilized.

Similar to the scan over frequency, there is a distinct dependence on the thickness of the graded interface, but only a small dependence on the number of layers comprising it, excluding the $N = 0$ to 1 change (Figure 28). When moving from the base two phase model to an interfacial region with any $N > 0$, there is a change to the response that increases with thickness in a nearly linear fashion. Additionally, for a change from $N = 1$ to 2 and beyond, the deviations become less negligible with thickness as well. For $d_i = 0$ nm, there is no phase depenotdence as the phase matrices (Φ) reduce to identity matrices at the limit of 0 thickness. Thus, the refraction matrices (W) accumulate to yield an

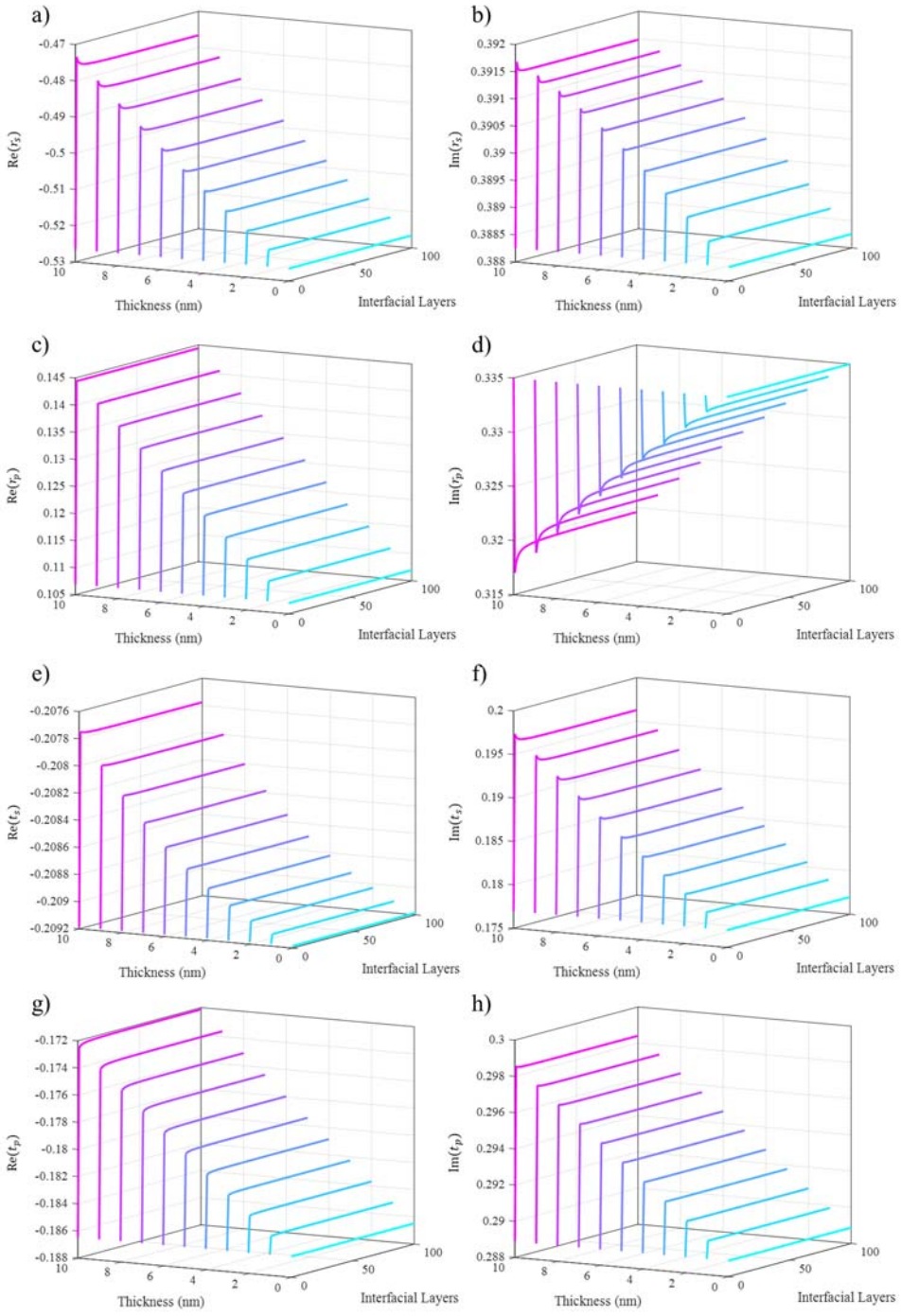

Figure 28. Real (a,c,e,g) and imaginary (b,d,f,h) reflection (a-d) and transmission (e-g) values for an s (a-b,e-f), and p (c-d,g-h) polarized input beam. Thickness used are (from blue to purple) 0-10 nm with increments of 1 nm.

identical output to the refraction across the discrete layer where $N = 0$, so there is no change to the total system value as the number of interfacial layers is changed. As will be shown, this result is exclusive to the consideration of the total system only. The amount of change for each parameter variation is dependent on the polarization and the geometry of the measurement (reflection vs transmission) as well.

Returning to the ellipsometry measurement mentioned previously, one can see how the discrete boundary approximation is entirely applicable for graded interfaces spanning smaller thicknesses approaching several monolayers. For example, PTCDI has a length of ~30 Å at its longest point.[194] Even without accounting for tilt when packing, consideration of an interface comprised of a single upright monolayer still places the approximation within an acceptable range. However, treatment of the sum frequency generation experiment requires transfer of the incident beams to the active interfaces, and the ensuing transfer of the generated sum frequency response to the external media, so the impact of the change may be larger than would be observed in an ellipsometric calculation.

I next examine the total system transfer (T) terms for the top and bottom interfaces using $T_{v_m} = \vec{t}^{SFG}_{v_m,0}\overleftarrow{t}^{vis}_{0,v_m}\overleftarrow{t}^{mIR}_{0,v_m}$ where the specific elements of each internal transfer matrix are given in equations 50-51, for m of $N + 1$ iterations (Figure 26). The real and imaginary responses as a function of total interfacial layer thickness and number of intermediary layers are shown in Figure 29. Within the set of figures, the objects are comprised of a series of differently colored planes, where each one is meant strictly for visual assistance. All $N + 1$ points for each thickness are contained within the relevant

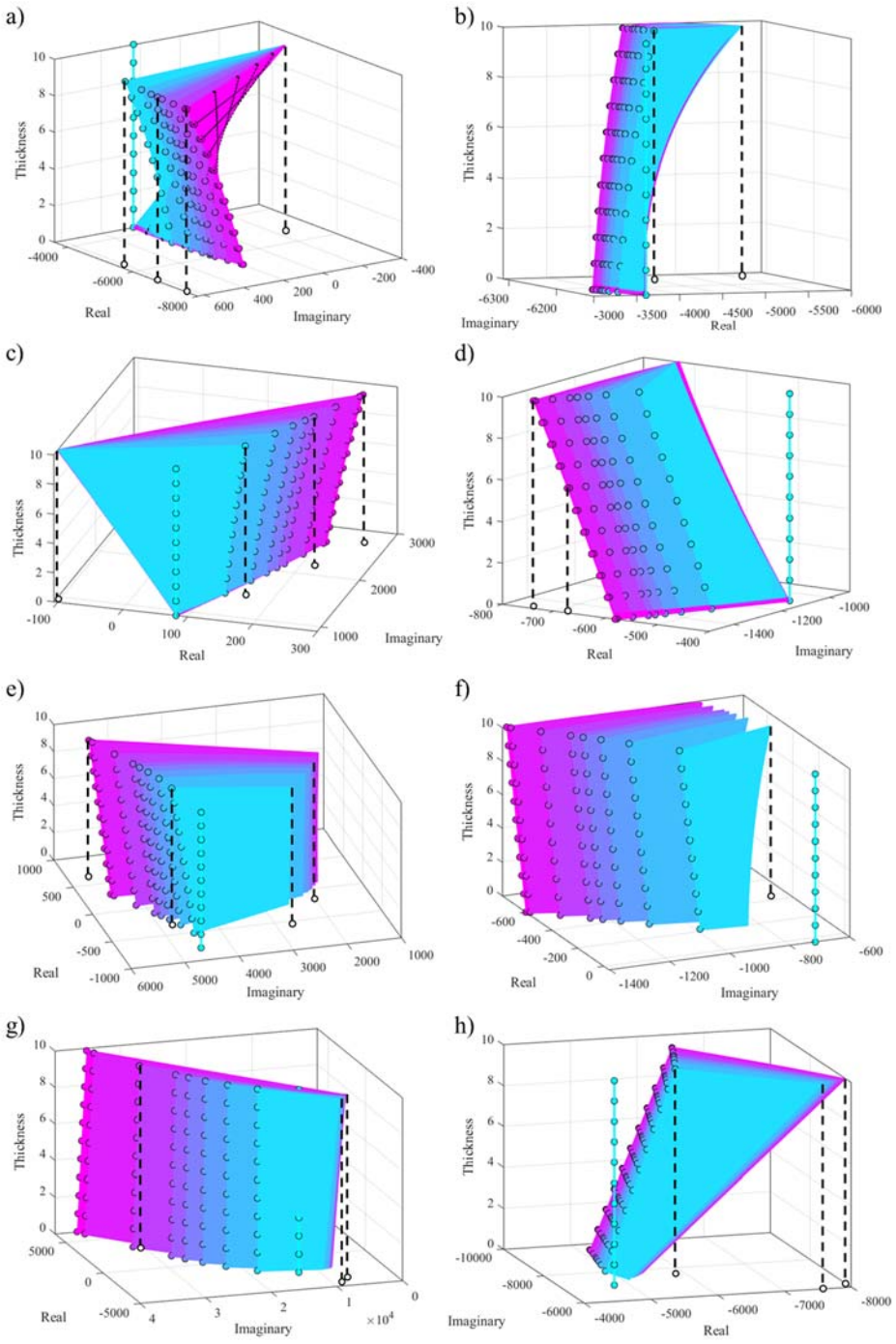

Figure 29. Top (a,c,e,g) and bottom (b,d,f,h) transfer matrices for the *ssp* (a-b), *sps* (c-d), *pss* (e-f), and *ppp* (g-h) polarization combinations. Number of interfacial layers, N, used are (from blue to purple) 0, 1, 2, 3, 4, 5, 10, 50, and 100, where the iteration 1 is shown by the circle markers. Black lines are provided for visual assistance.

plane, while the iteration $m = 1$ for each thickness is visualized by markers. The base model case, where $N = 0$ is provided as well for comparison in each spectra.

Figure 29a conveys the response for the top interface when measured in *ssp* geometry. The gridlines overlaid on the back of the 100 intermediary layer plane are provided to visually convey the surface curvature. The shape of the plot is analogous to a magazine being both twisted and splayed open. There are several immediate takeaways shown by the figure. First, as one moves across the plane for a given thickness (variation in m), there is a large importance on the choice of the active interface being transferred to and from. This begets the question, which iteration should be selected for an experimental SFG calculation, or should they all be used? This question will be addressed later in this chapter. Second, as one moves through the *z* axis (variation in d_i), it becomes apparent that the choice of the interfacial region thickness is also impactful on the outcome. To further assist visualization of this, the dotted black lines show the displacement between the 0 and 10 nm thicknesses, with the white markers capping the lines showing the *xy* location of the connected points. Third, as the number of interfacial layers is increased while the thickness is held at 0 nm, unlike the total system terms (Figures 27-28) there is a change in the result. Finally, going from $N = 0$ to 1 there is again a very large change relative to the change incurred upon further increases to the number of median layers for most thicknesses, highlighting the importance of interfacial treatment.

Generally, the above observations are consistent for both the top and bottom interfaces within each polarization combination. There are also several observable trends amongst all polarization combinations. Notably, the magnitude of change in both real and

imaginary space for the transfer matrix at the lower interface is smaller in each case, relative to the upper interface. This may be due, in part, to the smaller disparity in the refractive indices of PTCDI and SiO_2 versus PTCDI and air.[22, 101, 171] Previous studies using SHG when the indices of the materials used were proximal also reported little effect when the interface was considered unique from the surrounding media.[171] The geometry of the system will also play a role in the importance of the interface. I am assuming identical interfacial thicknesses in these simulations, though that may not be the case. The treatment of the interface, through selection of N, may also not be identical at each interface, though we are allocating each an identical value. Returning to Figure 29, for each transfer matrix plot at each N, the total displacement across the complex space between iterations $m = 1$ and $m = N + 1$ increases with d_i. This furthers the recurrent observation that proper treatment of the boundary increases in importance as the boundary thickness is increased. Finally, for the *ssp* and *sps* calculations iteration $m = N + 1$ when $d_i = 0$ is nearly identical regardless of N.

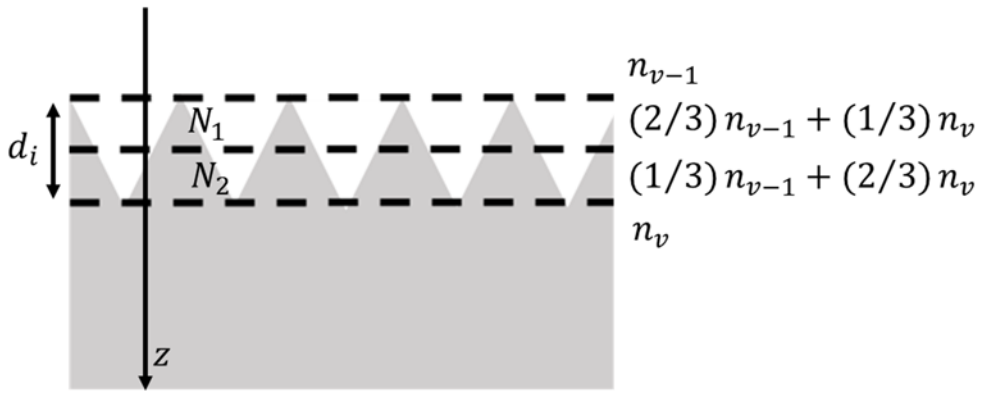

Figure 30. Geometry of 2D islands joining two layers with distinct refractive indices.

Returning to the question posed previously, how should the difference in the transfer matrices as the stack is iterated across be rectified? Certainly, one could select only a single mediary layer for transfer and signal generation. However, as each layer is composed of the vibrationally active material, this approach would be erroneous. Though the transfer matrix formalism requires a flat surface, consider the effect of the following on the general refractive index of each layer. If two adjacent layers are defined not by a discrete boundary, but instead a series of triangular connections (Figure 30) then the total refractive indices of any layer with N number of total interfacial layers, while the thickness of the layers is d_i/N will scale as shown in the figure. This geometry is similar to the three dimensional nanopinnacles employed in many graded index technologies.[183-185] This will result in an identical trend to the pattern drafted by equation 56. Furthermore, when examining this system through the lens of sum frequency generation, only the distinct chevron boundary separating the two materials will generate a response. The length of the boundary is equivalent within each layer, so each should receive equal weight. Hence, moving forward the results from each simulation will be averaged over all $N + 1$ iterations.

In the following set of figures, the polarization-dependent spatial average across all iterations is plotted as a function of d_i and N for the real and imaginary components of the transfer matrices at each interface (Figures 31-32). The markers provided in select *ppp* scans are placed at the $N = 0$ position within each thickness for visual assistance. As shown by the overall trends, the change going from $N = 0$ to 1 is quite important, however, for all polarization combinations there is an exponential-like drop-off in the impact of further increases in N. When plotting the slopes of one point to the next, for the

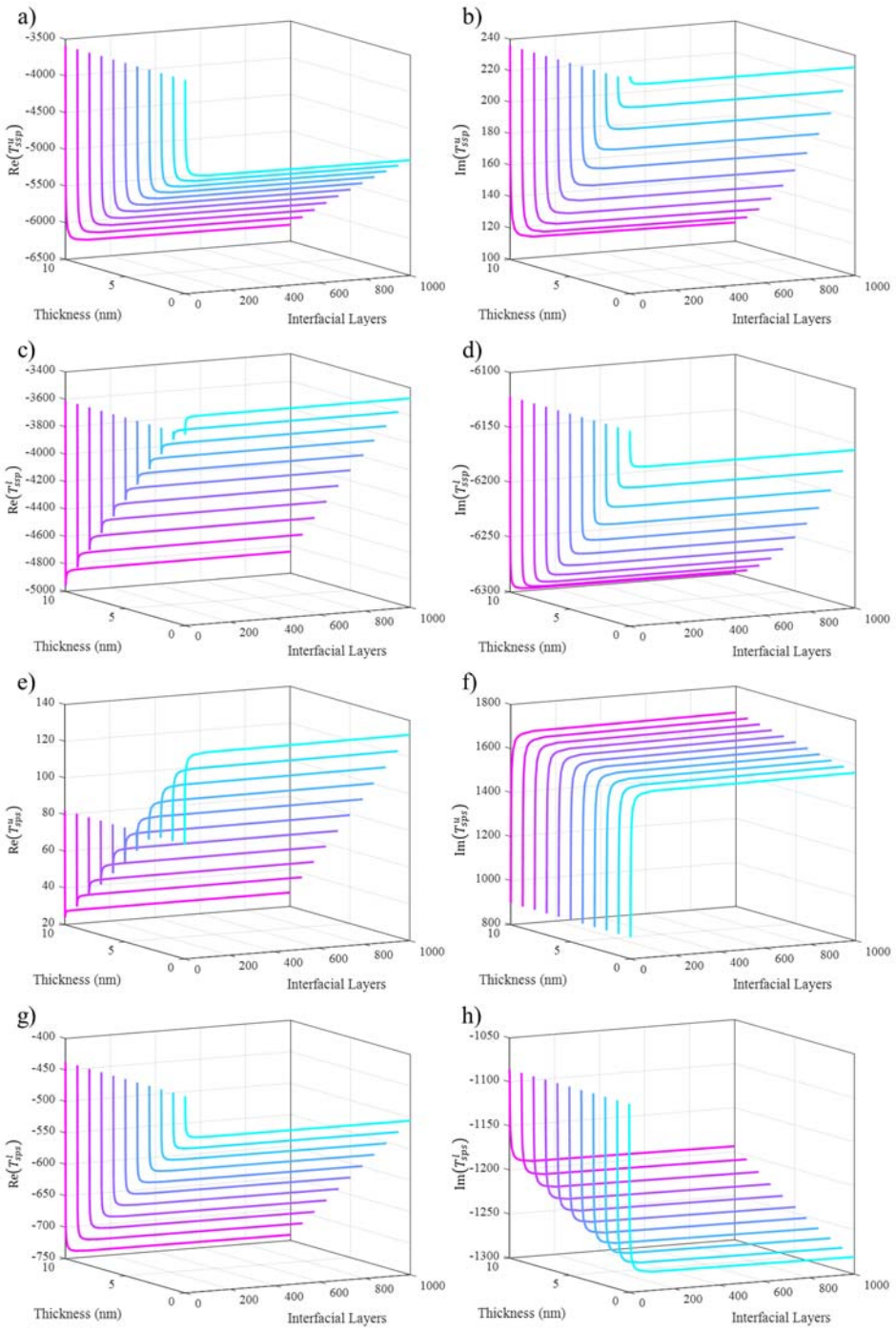

Figure 31. Average real (a,c,e,g) and imaginary (b,d,f,h) components for the iterated *ssp* (a-d) and *sps* (e-h) transfer matrices at the upper (a-b,e-f) and lower (c-d,g-h) interfaces. Thickness used are (from blue to purple) 0-10 nm with increments of 1 nm.

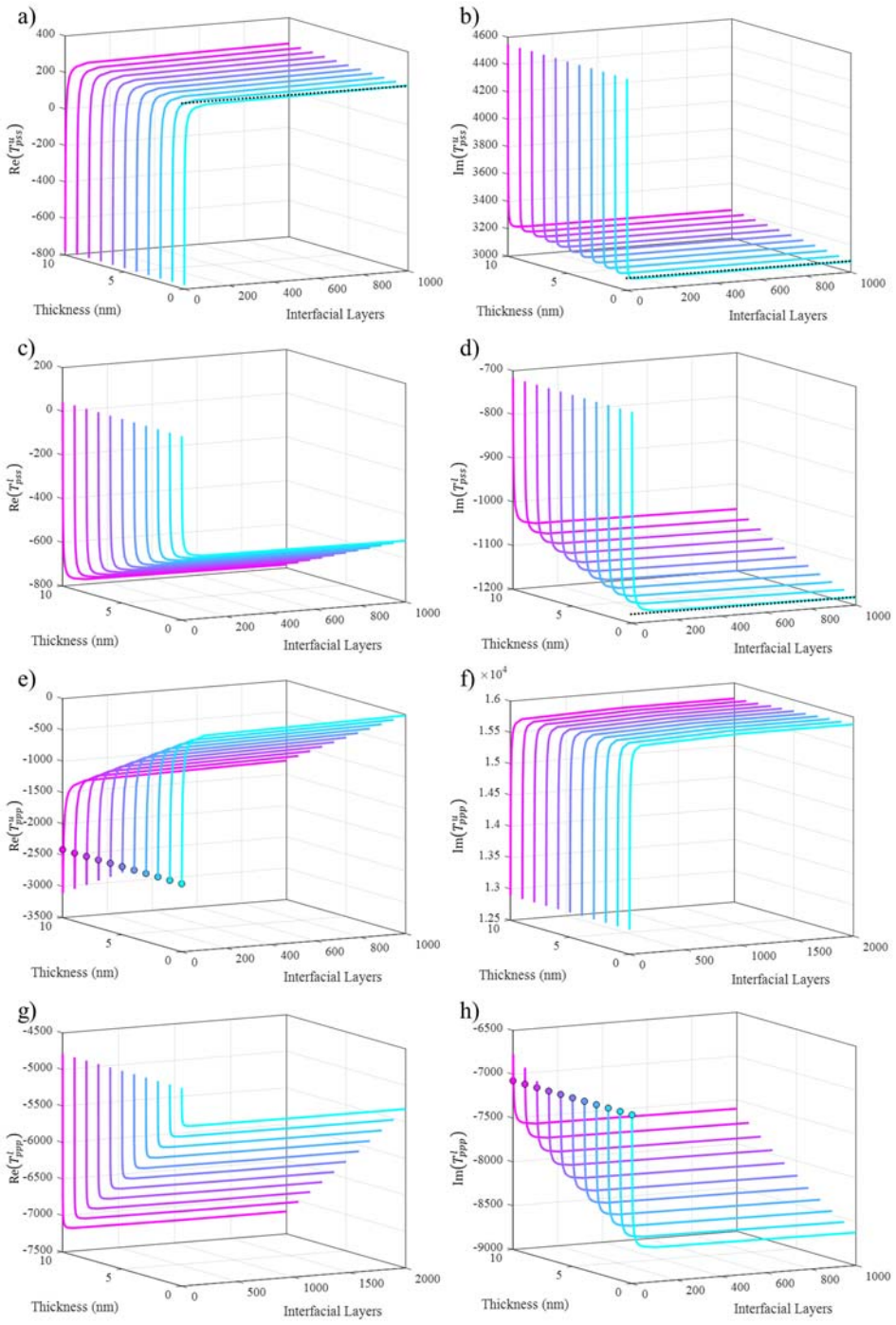

Figure 32. Average real (a,c,e,g) and imaginary (b,d,f,h) components for the iterated *pss* (a-d) and *ppp* (e-h) transfer matrices at the upper (a-b,e-f) and lower (c-d,g-h) interfaces. Thickness used are (from blue to purple) 0-10 nm with increments of 1 nm.

$N = 50$ to 100 data points for each plot, the magnitude of the slopes for the upper interface are between 0.0006 – 1, being greatest for the *ppp* setup. For the lower interface the slopes are between 0.003 – 0.2, for both the real and imaginary responses. These results suggest that for all combinations excluding *ppp* the computation need not exceed 50 interfacial layers, reducing the overall time spent iterating through the model as the returns are negligible.

When accumulating the above terms into the total SFG intensity, each interfacial transfer matrix is multiplied against the nonlinear susceptibility. These results are summed then squared in accordance with equations 50-51. Figure 33 houses the VSFG responses for each polarization combination as both d_i and N are varied. The dashed line tracing the peak of the $N = 100$ lines for each thickness is present for both resonant modes to help visualize the change relative to the solid lines, which are flat. As shown by each figure, the largest change in any dimension occurs going from $N = 0$ to 1, as expected. Following suit from Figure 32, as N approaches higher values, there is still appreciable change to the spectra when using *ppp* geometry. Finally, we also observe an impact on d_i, however it is less impactful for all polarization combinations other than *ppp*.

There are two adjustable parameters included in this method, N and d_i. The SFG results show much less change in the outcome as d_i is varied relative to the variation incurred upon a modification in N. Ultimately, these adjustable parameters could be included as fittable terms in the program, however, with the minute differences provided through d_i, the returns may not be worth the inclusion of another unknown variable. Thus, it may be beneficial to include d_i only as a known variable, setting it somewhere

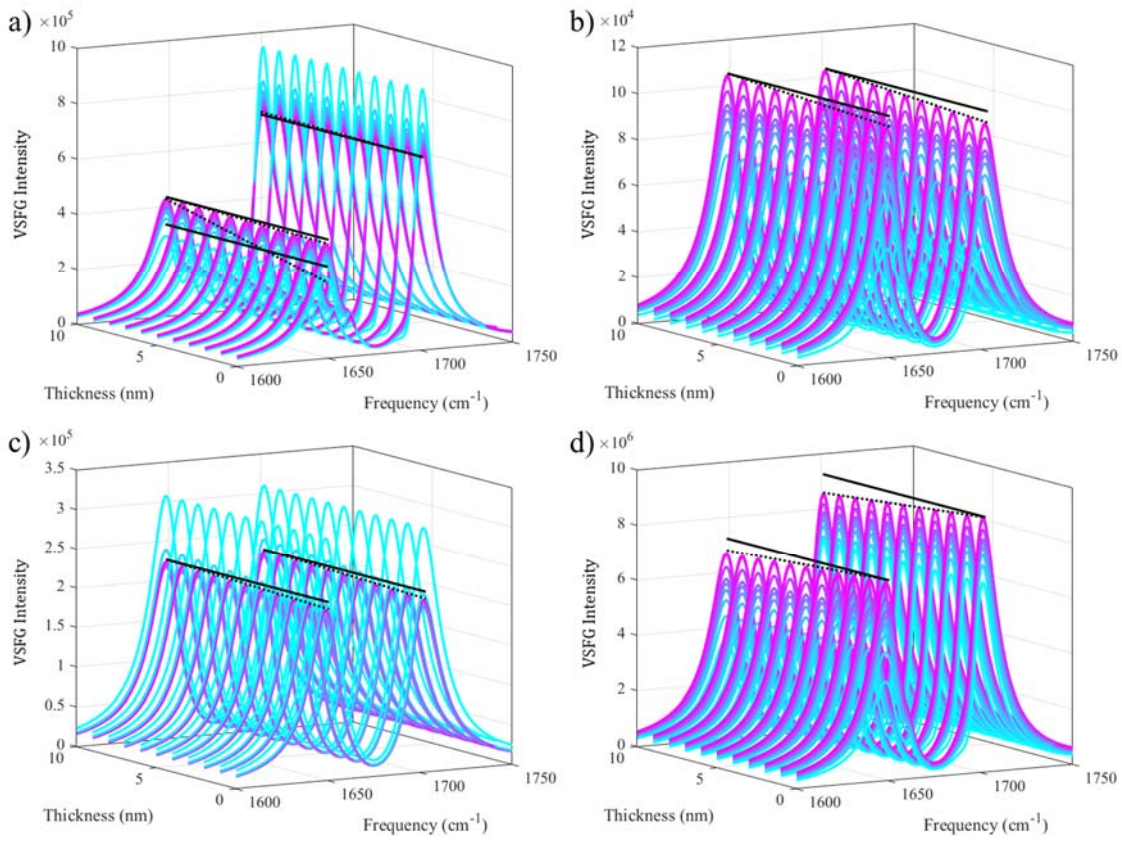

Figure 33. Sum frequency generation intensity for the *ssp* (a), *sps* (b), *pss* (c), and *ppp* (d) polarization combinations. Number of interfacial layers, N, used are (from blue to purple) 0, 1, 2, 3, 4, 5, 10, 50, and 100. Black lines are provided for visual assistance.

near the expected interfacial thickness, or to an arbitrary value if the thickness has not been determined. This is especially relevant for all polarization combinations exempting *ppp*. N would be set to a floating parameter with a minimum of zero, and a maximum of around 10-50. As shown by the models presented in this chapter, calculation beyond the suggested values becomes increasingly time ineffective. The optimization would attempt to minimize the value of N while fitting it alongside the nonlinear susceptibility terms. Further work would focus on the differentiation between modified multilayer phase

models and inclusion of the approaches within the routine. Similar to Chapter 4, multi-collection experiments, with some variable changed (material thickness, beam angle, etc.) paired with the fitting of multiple polarization combinations in tandem may yield the best results for a more confident solution to N. Further, the general design of such a system would also allow for N to be locked at a single value, providing treatment through either a multi-phase system, or a modified system following extended definition of the non-integer area.

5.4. Conclusions

Consideration of the vibrationally active interfaces with continuous, variable, or graded linear refractive indices through the lens of transfer matrix formalism provides a variety of impact. One must consider the thickness of the interfacial region, the number of layers included in the interfacial regime, and the frequency of the optical sources involved. In addition, different layers in the interfacial stack will yield different results, and a spatial average over all iterations is necessary. While inclusion of multiple medial layers has little impact of the total system reflection and transmission terms, the SFG experiment can be significantly altered. Application of the proposed fitting variables could provide a general unified system capable of treating modified or straightforward multi-phase systems.

REFERENCES

1. Maiman, T. H., Simulated Optical Radiation in Ruby. *Nature* **1960,** *187*, 493-494.
2. Bloembergen, N.; Pershan, P. S., Light Waves at the Boundary of Nonlienar Media. *Physical Reviews* **1962,** *128*, 606-622.
3. Zhu, X. D.; Suhr, H.; Shen, Y. R., Surface Vibrational Spectroscopy by Infrared-visible Sum Frequency Generation. *Phys. Rev. B* **1987,** *35*, 3047-3050.
4. Yan, E. C. Y.; Fu, L.; Wang, Z.; Liu, W., Biological Macromolecules at Interfaces Probed by Chiral Vibrational Sum Frequency Generation Spectroscopy. *Chem. Rev.* **2014,** *114*, 8471-8498.
5. Nihonyanagi, S.; Yamaguchi, S.; Tahara, T., Ultrafast Dynamics at Water Interfaces Studied by Vibrational Sum Frequency Generation Spectroscopy. *Chem. Rev.* **2017,** *117*, 10665-10693.
6. Rey, N.; Dlott, D., Studies of Electrochemical Interfaces by Broadband Sum Frequency Generation. *J. Electroanal. Chem.* **2017,** *800*, 114-125.
7. Wei, X.; Hong, S. C.; Zhuang, X.; Goto, T.; Shen, Y. R., Nonlinear Optical Studies of Liquid Crystal Alignment on a Rubbed Polyvinyl Alcohol Surface. *Phys. Rev. E* **2000,** *62* (4), 5160-5172.
8. Araoka, F.; Isoda, M.; Miyajima, D.; Seo, I.; Oh-e, M.; Aida, T.; Takezoe, H., Polar Dynamics at a Functional Group Level: Infrared-Visible Sum-Frequency Generation Study on Polar Columnar Liquid Crystals. *Advanced Electronic Materials* **2017,** *3* (3), 1600503.
9. Zhuang, X.; Miranda, P. B.; Kim, D.; Shen, Y. R., Mapping Molecular Orientation and Conformation at Interfaces by Surface Nonlinear Optics. *Phys. Rev. B* **1999,** *59* (19), 12632-12640.
10. Li, X.; Rupprechter, G., Sum Frequency Generation Spectroscopy in Heterogeneous Model Catalysis: A Minireview of CO-Related Processes. *Catalysis Science and Technology* **2021,** *11*, 12-26.
11. Anglin, T.; O'Brien, D.; Massari, A., Monitoring the Charge Accumulation Process in Polymeric Field-Effect Transistors via in Situ Sum Frequency Generation. *J. Phys. Chem. C* **2010,** *114*, 17629-17637.
12. O'Brien, D. B.; Massari, A. M., Modeling Multilayer Thin Film Interference Effects in Interface-Specific Coherent Nonlinear Optical Spectroscopies. *J. Opt. Soc. Am. B* **2013,** *30* (6), 1503-1512.
13. Wan, Q.; Galli, G., First-Principles Framework to Compute Sum-Frequency Generation Vibrational Spectra of Semiconductors and Insulators. *Phys. Rev. Lett.* **2015,** *115*, 246404.
14. Humbert, C.; Noblet, T.; Dalstein, L.; Busson, B.; Barbillon, G., Sum-Frequency Generation Spectroscopy of Plasmonic Nanomaterials: A Review. *Materials* **2019,** *12*, 836.
15. Zhang, C., Sum Frequency Generation Vibrational Spectroscopy for Characterization of Buried Polymer Interfaces. *Appl. Spectrosc.* **2017,** *71* (8), 1717-1749.
16. Tahara, T.; Yamaguchi, S., Precise Electronic $\chi^{(2)}$ Spectra of Molecules Adsorbed at an Interface Measured by Multiplex Sum Frequency Generation. *J. Phys. Chem. B* **2004,** *108* (50), 19079-19082.

17. Deng, G. H.; Qian, Y.; Zhang, T.; Han, J.; Chen, H.; Rao, Y., Two-Dimensional Electronic-Vibrational Sum Frequency Spectroscopy for Interactions of Electronic and Nuclear Motions at Interfaces. *PNAS* **2021,** *118* (34), e2100608118.
18. Boyd, R., *Nonlinear Optics*. 3rd ed.; Academic Press: 2008.
19. Shen, Y. R., *The Principles of Nonlinear Optics*. John Wiley and Sons: Hoboken, New Jersey, 1984.
20. Velarde, L.; Wang, H. F., Unified Treatment and Measurement of the Spectral Resolution and Temporal Effects in Frequency-Resolved Sum-Frequency Generation Vibrational Spectroscopy (SFG-VS). *PCCP* **2013,** *15*, 19970-19984.
21. Lambert, A.; Davies, P.; Neivandt, D., Implementing the Theory of Sum Frequency Generation Vibration Spectroscopy: A Tutorial Review. *Applied Spectroscopy Reviews* **2005,** *40* (2), 103-145.
22. O'Brien, D. B.; Massari, A. M., Experimental Evidence for an Optical Interference Model for Vibrational Sum Frequency Generation on Multilayer Organic Thin Film Systems. II. Consideration for Higher Order Terms. *J. Chem. Phys.* **2015,** *142*, 024704.
23. Mori, W.; Wang, L.; Sato, Y.; Morita, A., Development of Quadrupole Susceptibility Automatic Calculator in Sum Frequency Generation Spectroscopy and Application to Methyl C-H Vibrations. *J. Chem. Phys.* **2020,** *153*, 174705.
24. Shen, Y. R., Revisiting the Basic Theory of Sum-Frequency Generation. *J. Chem. Phys.* **2020,** *153*, 180901.
25. Simpson, G. J., Connection of Jones and Mueller Tensors in Second Harmonic Generation and Multi-Photon Fluorescence Measurements. *J. Phys. Chem. B* **2016,** *120*, 3281-3302.
26. Wang, H.-F.; Velarde, L.; Gan, W.; Fu, L., Quantitative Sum-Frequency Generation Vibrational Spectroscopy of Molecular Surfaces and Interfaces: Lineshape, Polarization, and Orientation. *Annu. Rev. Phys. Chem.* **2015,** *66*, 189-216.
27. Jellison, G. E.; Burke, H. H., The Temperature Dependence of the Refractive Index of Silicon at Elevated Temperatures at Several Laser Wavelengths. *J. Appl. Phys.* **1986,** *60*, 841-843.
28. Tompkins, H. G., *A User's Guide to Ellipsometry*. Academic Press, Inc: San Diego, CA, 1993.
29. Hickey, M. C.; Akyurtlu, A.; Kussow, A. G., Relationship between the Kramers-Kronig Relations and Negative Index of Refraction. *Phys. Rev. A: At. Mol. Opt. Phys.* **2010,** *82*, 055802.
30. Sai, T.; Saba, M.; Dufresne, E. R.; Steiner, U.; Wilts, B. D., Designing Refractive Index Fluids Using the Kramers-Kronig Relations. *Faraday Discuss.* **2020,** *223* (136-144).
31. Fresnel, A., *Oeuvres Complètes d'Augustin Fresnel*. de Senarmont, H. Verdet, E. Fresnel, L.: Paris, 1866; Vol. 1.
32. Cobet, C.; Oppelt, K.; Hingerl, K.; Neugebauer, H.; Knör, G.; Sariciftci, N. S.; Gasiorowski, J., Ellipsometric Spectroelectrochemistry: An in Situ Insight in the Doping of Conjugated Polymers. *J. Phys. Chem. C* **2018,** *122*, 24309-24320.
33. Moffitt, S. L.; Schelhas, L. T.; Melkote, S.; Toney, M. F., *Multifunctional Optical Coatings and Light Management for Photovoltaics*. Ginley, D., Fix, T., Eds.: Elsevier: Amsterdam, Netherlands, 2019.

34. Lin, Y. H.; Li, W.; Faber, H.; Seitkhan, A.; Hastas, N. A.; Khim, D.; Zhang, Q.; Zhang, X.; Pliatsikas, N.; Tsetseris, L.; Patsalas, P. A.; Bradley, D. D. C.; Huang, W.; Anthopoulos, T. D., Hybrid Organic-Metal Oxide Multilayer Channel Transistors with High Operational Stability. *Nature Electronics* **2019,** *2*, 587-595.
35. Gautam, K. S.; Schwab, A. D.; Dhinojwala, A.; Zhang, D.; Dougal, S. M.; Yeganeh, M. S., Molecular Structure of Polystyrene at Air/Polymer and Solid/Polymer Interfaces. *Phys. Rev. Lett.* **2000,** *85*, 3854-3857.
36. Harp, G. P.; Gautam, K. S.; Dhinojwala, A., Probing Polymer/Polymer Interfaces. *J. Am. Chem. Soc.* **2002,** *124* (27), 7908-7909.
37. Li, G.; Dhinojwala, A.; Yeganeh, M. S., Interference Effect From Buried Interfaces Investigated by Angular-Dependent Infrared-Visible Sum Frequency Generation Technique. *J. Phys. Chem. C* **2011,** *115*, 7554-7561.
38. Sipe, J. E., New Green-Function Formalism for Surface Optics. *J. Opt. Soc. Am. B* **1987,** *4* (4), 481-489.
39. Wilson, P. T.; Briggman, K. A.; Wallace, W. E.; Stephenson, J. C.; Richter, L. J., Selective Study of Polymer/Dielectric Interfaces with Vibrationally Resonant Sum Frequency Generation via Thin-Film Interference. *Applied Physical Letters* **2002,** *80*, 3084-3086.
40. Troparevsky, M. C.; Sabau, A. S.; Lupini, A. R.; Zhang, Z., Transfer-Matrix Formalism for the Calculation of Optical Response in Multilayer Systems: From Coherent to Incoherent Interference. *Opt. Express* **2010,** *18* (24), 24715-24721.
41. Knittl, Z., *Optics of Thin Films*. Wiley: 1976.
42. Shen, Y. R., Optical Second Harmonic Generation at Interfaces. *Annu. Rev. Phys. Chem.* **1989,** *40*, 327-350.
43. O'Brien, D. B.; Massari, A. M., Simulated Vibrational Sum Frequency Generation from a Multilayer Thin Film System with Two Active Interfaces. *J. Chem. Phys.* **2013,** *138* (15), 154708.
44. Motti, S. G.; Cardoso, L. S.; Gomes, D. J. C.; Faria, R. M.; Miranda, P. B., Probing Device Degradation and Electric Fields in Polymeric Field-Effect Transistors by SFG Vibrational Spectroscopy. *J. Phys. Chem. C* **2018,** *122*, 10450-10458.
45. Lambert, A. G.; Neivandt, D. J.; Briggs, A. M.; Usadi, E. W.; Davies, P. B., Interference Effects in Sum Frequency Spectra from Monolayers on Composite Dielectric / Metal Substrates. *J. Phys. Chem. B* **2002,** *106*, 5461-5469.
46. McGall, S. J.; Davies, P. B.; Neivandt, D. J., Interference Effects in Sum Frequency Vibrational Spectra of Thin Polymer Films: An Experimental and Modeling Investigation. *J. Phys. Chem. B* **2004,** *108*, 16030-16039.
47. Tong, Y.; Zhao, Y.; Li, N.; Osawa, M.; Davies, P. B.; Ye, S., Interference Effects in the Sum Frequency Generation Spectra of Thin Organic Films. I. Theoretical Modeling and Simulation. *J. Chem. Phys.* **2010,** *133*, 034704.
48. FitzGerald, W.; Jena, K. C.; Hore, D. K., Effects of Single-Source Multiple Beam Interference in Vibrational Sum Frequency Generation Spectroscopy. *J. Mol. Struct.* **2015,** *1084*, 368-373.
49. Azam, M. S.; Cai, C.; Hore, D. K., Selective Probing of Thin-Film Interfaces Using Internal Reflection Sum Frequency Spectroscopy. *J. Phys. Chem. C* **2019,** *123*, 23535-23544.

50. Cotton, D. E.; Moon, A. P.; Roberts, S. T., Using Electronic Sum-Frequency Gneration to Analyze the Interfacial Structure of Singlet Fission-Capable Perylenediimide Thin Films. *J. Phys. Chem. C* **2020,** *124*, 11401-11413.
51. Cotton, D. E.; Roberts, S. T., Sensitivity of Sum Frequency Generation Experimental Conditions to Thin Film Interference Effects. *J. Chem. Phys.* **2021,** *154*, 114794.
52. Prichett, I. G.; Massari, A. M., Simplified Sum Frequency Generation Using a Narrow Free-Spectral-Range Etalon. *Opt. Lett.* **2018,** *43* (19), 4747-4750.
53. Lorch, C.; Banerjee, R.; Frank, C.; Dieterle, J.; Hinderhofer, A.; Gerlach, A.; Schreiber, F., Growth of Competing Crystal Phases of α-Sexithiophene Studied by Real-Time in Situ X-ray Scattering. *J. Phys. Chem. C* **2015,** *119* (1), 819-825.
54. Bouchoms, I.; Schoonveld, W. A.; Vrijmoeth, J.; Klapwijk, T. M., Morphology Identification of the Thin Film Phases of Vacuum Evaporated Pentacene on SiO_2 Substrates. *Synth. Met.* **1999,** *104* (3), 175-178.
55. Brillante, A.; Bilotti, I.; Albonetti, C.; Moulin, J. F.; Stoliar, P.; Biscarini, F.; Leeuw, D. M., Confocal Raman Spectroscopy of α-Sexithiophene: From Bulk Crystals to Field-Effect Transistors. *Adv. Funct. Mater.* **2007,** *17* (16), 3119-3127.
56. Jones, A. O. F.; Chattopadhyay, B.; Geerts, Y. H.; Resel, R., Substrate-Induced and Thin-Film Phases: Polymorphism of Organic Materials on Surfaces. *Adv. Funct. Mater.* **2016,** *26* (14), 2233-2255.
57. Petit, M.; Hayakawa, R.; Wakayama, Y.; Chikyow, T., Early Stage of Growth of a Perylene Diimide Derivative Thin Film Growth on Various Si(001) Substrates. *J. Phys. Chem. C* **2007,** *111* (34), 12747-12751.
58. Dürr, A. C.; Koch, N.; Kelsch, M.; Rühm, A.; Ghijsen, J.; Johnson, R. L.; Pireaux, J. J.; Schwartz, J.; Schreiber, F.; Dosch, H.; Kahn, A., Interplay Between Morphology, Structure, and Electronic Properties at Diindenoperylene-Gold Interfaces. *Phys. Rev. B* **2003,** *68* (11), 913.
59. Kowarik, S.; Gerlach, A.; Sellner, S.; Schreiber, F.; Cavalcanti, L.; Konovalov, O., Real-Time Observation of Structural and Orientational Transitions during Growth of Organic Thin Films. *Phys. Rev. Lett.* **2006,** *96* (12), 125504.
60. Mattheus, C. C.; de Wijs, G. A.; de Groot, R. A.; Palstra, T. T. M., Modeling the Polymophism of Pentacene. *J. Am. Chem. Soc.* **2003,** *125* (20), 6323-6330.
61. Ivanco, J.; Krenn, J. R.; Ramsey, M. G.; Netzer, F. P.; Haber, T.; Resel, R.; Haase, A.; Stadlober, B.; Jakopic, G., Sexithiophene Films on Clean and Oxidized Si(111) Surfaces: Growth and Electronic Structure. *J. Appl. Phys.* **2004,** *96* (5), 2716-2724.
62. Riera-Galindo, S.; Tamayo, A.; Mas-Torrent, M., Role of Polymorphism and Thin-Film Morphology in Organic Semiconductors Processed by Solution Shearing. *ACS Omega* **2018,** *3* (2), 2329-2339.
63. Della Valle, R. G.; Venuti, E.; Brillante, A.; Girlando, A., Are Crystal Polymorphs Predictable? The Case of Sexithiophene. *J. Phys. Chem. A* **2008,** *112* (29), 6715-6722.
64. Delgado, M. C. R.; Kim, E.-G.; da Silva, D. A.; Bredas, J.-L., Tuning the Charge-Transport Parameters of Perylene Diimide Single Crystals via End and/or Core. *J. Am. Chem. Soc.* **2010,** *132* (10), 3375-3387.

65. Dimitrakopoulos, C. D.; Malenfant, P. R. L., Organic Thin Film Transistors for Large Area Electronics. *Adv. Mater.* **2002,** *14* (2), 99-115.
66. Horowitz, G.; Hajlaoui, M. E., Mobility in Polycrystalline Oligothiophene Field-Effect Transistors Dependent on Grain Size. *Adv. Mater.* **2000,** *12* (14), 1046-1050.
67. Servet, B.; Horowitz, G.; Ries, S.; Lagorsse, O.; Alnot, P.; Yassar, A.; Deloffre, F.; Srivastava, P.; Hajlaoui, R.; Lang, P.; Garnier, F., Polymorphism and Charge Transport in Vacuum-Evaporated Sexithiophene Films. *Chem. Mater.* **1994,** *6*, 1809-1815.
68. da Como, E.; Loi, M. A.; Murgia, M.; Zamboni, R.; Muccini, M., J-Aggregation in α-Sexithiophene Submonolayer Films on Silicon Dioxide. *J. Am. Chem. Soc.* **2006,** *128* (13), 4277-4281.
69. Egelhaaf, H. J.; Bäuerle, P.; Rauer, K.; Hoffmann, V.; Oelkrug, D., UV/Vis and IR Spectroscopic Studies on Molecular Orientation in Ultrathin Films of Polythiophene Model Compounds. *J. Mol. Struct.* **1993,** *293*, 249-252.
70. Horowitz, G.; Bachet, B.; Yassar, A.; Lang, P.; Demanze, F.; Fave, J. L.; Garnier, F., Growth and Characterization fo Sexithiophene Single Crystals. *Chem. Mater.* **1995,** *7*, 1337-1341.
71. Siegrist, T.; Fleming, R. M.; Haddon, R. C.; Laudise, R. A.; Lovinger, A. J.; Katz, H. E.; Bridenbaugh, P.; Davis, D. D., The Crystal Structure of the High-Temperature Polymorph of α-Hexathienyl (α-6T/HT). *J. Mater. Res* **1995,** *10* (9), 2170-2173.
72. Moser, A.; Salzmann, I.; Oehzelt, M.; Neuhold, A.; Flesch, H. G.; Ivanco, J.; Pop, S.; Toader, T.; Zahn, D. R. T.; Smilgies, D. M.; Resel, R., A Disordered Layered Phase in Thin Films of Sexithiophene. *Chem. Phys. Lett.* **2013,** *574*, 51-55.
73. Brillante, A.; Bilotti, I.; Biscarini, F.; Della Valle, R. G.; Venuti, E., Polymorphs of α-Sexithiophene Probed by Lattice Phonon Raman Microscopy. *Chem. Phys.* **2006,** *328*, 125-131.
74. Koini, M.; Haber, T.; Berkebile, S.; Koller, G.; Ramsey, M. G.; Resel, R.; Oehzelt, M., Growth of Sexithiophene Crystals on Cu(110)and Cu(110)-(2x1)O Stripe Phase - The Influence of Surface Corrugation. *J. Cryst. Growth* **2009,** *311* (5), 1364-1369.
75. Lang, P.; Hajlaoui, R.; Garnier, F.; Desbat, B.; Buffeteau, T.; Horowitz, G.; Yassar, A., IR Spectroscopy Evidence for a Substrate-Dependent Organization of Sexithiophene Thin Films Vacuum-Evaporated onto SiH/Si and SiO_2/Si. *J. Phys. Chem.* **1995,** *99* (15), 5492-5499.
76. Taima, T.; Shahiduzzaman, M.; Ishizeki, T.; Yamamoto, K.; Karakawa, M.; Kuwabara, T.; Takahashi, K., Sexithiophene-Based Photovoltaic Cells with High Light Absorption. *J. Phys. Chem. C* **2017,** *121* (36), 19699-19704.
77. Schwabegger, G.; Djuric, T.; Sitter, H.; Resel, R.; Simbrunner, C., Morphological and Structural Investigation of Sexithiophene Growth on KCl(100). *Cryst. Growth Des.* **2013,** *13* (2), 536-542.
78. Simbrunner, C., Epitaxial Growth of Sexi-Thiophene and Para-Hexaphenyl and its Implications for the Fabrication of Self-Assembled Lasing Nano-Fibres. *Semicond. Sci. Technol.* **2013,** *28* (5), 53001.
79. Derrien, T. L.; Lauritzen, A. E.; Kaienburg, P.; Hardigree, J. F. M.; Nicklin, C.; Riede, M., *In Situ* Observations of the Growth Mode of Vacuum-Deposited *α*-Sexithiophene. *J. Phys. Chem. C* **2020,** *124*, 11863-11869.

80. Loi, M. A.; Da Como, E.; Dinelli, F.; Murgia, M.; Zamboni, R.; Biscarini, F.; Muccini, M., Supramolecular Organization in Ultra-Thin Films of α-Sexithiophene on Silicon Dioxide. *Nature Materials* **2005,** *4* (1), 81-85.
81. Lang, P.; El Ardhaoui, M.; Wittmann, J. C.; Dallas, J. P.; Horowitz, G.; Lotz, B.; Garnier, F.; Straupe, C., Substrate Dependent Orientation and Structure of Sexithiophene Thin Films. *Synth. Met.* **1997,** *84*, 605-606.
82. Dinelli, F.; Murgia, M.; Levy, P.; Cavallini, M.; Biscarini, F.; De Leeuw, D. M., Spatially Correlated Charge Transport in Organic Thin Film Transistors. *Phys. Rev. Lett.* **2004,** *92* (11), 11.
83. Liu, S.; Mannsfeld, S. C. B.; Wang, W. M.; Sun, Y. S.; Stoltenberg, R. M.; Bao, Z., Patterning of α-Sexithiophene Single Crystals with Precisely Controlled Sizes and Shapes. *Chem. Mater.* **2009,** *21* (1), 15-17.
84. de Bettignies, R.; Nicolar, Y.; Blanchard, P.; Levillain, E.; Nunzi, J. M.; Roncali, J., Planarized Star-Shaped Oligothiophenes as a New Class of Organic Semiconductors for Heterojunction Solar Cells. *Adv. Mater.* **2003,** *15* (22), 1939-1943.
85. Hörmann, U.; Wagner, J.; Gruber, M.; Opitz, A.; Brütting, W., Approaching the Ultimate Open Circuit Voltage in Thiophene Based Single Junction Solar Cells by Applying Diindenoperylene as Acceptor. *Physica Status Solidi RRL* **2011,** *5* (7), 241-243.
86. Horowitz, G.; Fichou, D.; Peng, X.; Xu, Z.; Garnier, F., A Field-Effect Transistor Based on Conjugated Alph-Sexithienyl. *Solid State Commun.* **1989,** *72* (4), 381-384.
87. Koch, N., Organic Electronic Devices and Their Functional Interfaces. *ChemPhysChem* **2007,** *8*, 1438-1455.
88. Kearns, P.; O'Brien, D.; Massari, A., Optical Interference Enhances Nonlinear Spectroscopic Sensitivity: When Light Gives You Lemons, Model Lemonade. *J. Phys. Chem. Lett.* **2016,** *7*, 62-68.
89. O'Brien, D. B.; Anglin, T. C.; Massari, A. M., Surface Chemistry and Annealing-Driven Interfacial Changes in Organic Semiconducting Thin Films on Silica Surfaces. *Langmuir* **2011,** *27*, 13940-13949.
90. Sohrabpour, Z.; Kearns, P. M.; Massari, A. M., Vibrational Sum Frequency Generation Spectroscopy of Fullerene at Dielectric Interfaces. *J. Phys. Chem. C* **2016,** *120*, 1666-1672.
91. Zhang, D.; Gutow, J.; Eisenthal, K. B., Vibrational Spectra, Orientations, and Phase Transitions in Long-Chain Amphiphiles at the Air/Water Interface: Probing the Head and Tail Groups by Sum Frequency Generation. *J. Phys. Chem.* **1994,** *98*, 13729-13734.
92. Pithan, L.; Cocchi, C.; Zschiesche, H.; Weber, C.; Zykov, A.; Bommel, S.; Leake, S.; Schafer, P.; Draxl, C.; Kowarik, S., Light Controls Polymorphism in Thin Films of Sexithiophene. *Crystal Growth Design* **2015,** *15* (3), 1319-1324.
93. Servet, B.; Ries, S.; Trotel, M.; Alnot, P.; Horowitz, G.; Garnier, F., X-ray Determination of the Crystal-Structure and Orientation of Vacuum-Evaporated Sexithiophene Films. *Adv. Mater.* **1993,** *5* (6), 461-464.
94. Louarn, G.; Buisson, J.; Lefrant, S.; Fichou, D., Vibrational Studies of a Series of α-Oligothiophenes as Model Systems of Polythiophene. *J. Phys. Chem.* **1995,** *99*, 11399-11404.

95. Albonetti, C.; Barbalinardo, M.; Milita, S.; Cavallini, M.; Liscio, F.; Moulin, J. F.; Biscarini, F., Selective Growth of α-Sexithiophene by Using Silicon Oxides Patterns. *Int. J. Mol. Sci.* **2011,** *12*, 5719-5735.
96. Ivanco, J.; Haber, T.; Krenn, J. R.; Netzer, F. P.; Resel, R.; Ramsey, M. G., Sexithiophene Films on Ordered and Disordered TiO_2(110) Surfaces: Electronic, Structural, and Mophological Properties. *Surf. Sci.* **2007,** *601*, 178-187.
97. Kearns, P. M.; Sohrabpour, Z.; Massari, A. M., Frequency Comb SFG: a New Approach to Multiplex Detection. *Opt. Express* **2016,** *24* (17), 19863-19870.
98. Yesudas, F.; Mero, M.; Kneipp, J.; Heiner, Z., Vibrational Sum-Frequency Generation Spectroscopy of Lipid Bilayers at Repetition rates up to 100 kHz. *J. Chem. Phys.* **2018,** *148*, 104702.
99. Stiopkin, I. V.; Jayathilake, H. D.; Weeraman, C.; Benderskii, A. V., Temporal Effects on Spectroscopic Line Shapes, Resolution, and Sensitivity of the Broad-Band Sum Frequency Generation. *J. Chem. Phys.* **2010,** *132*, 234503.
100. Lagutchev, A.; Hambir, S. A.; Dlott, D. D., Nonresonant Background Suppression in Broadband Vibrational Sum-Frequency Generation Spectroscopy. *J. Phys. Chem. C* **2007,** *111*, 13645-13647.
101. O'Brien, D. B.; Massari, A. M., Experimental Evidence for an Optical Interference Model for Vibrational Sum Frequency Generation on Multilayer Organic Thin Film Systems. I. Electric Dipole Approximation. *J. Chem. Phys.* **2015,** *142*, 024703.
102. Palik, E. D., *Handbook of Optical Constants of Solids*. Academic Press: San Diego, 1998; Vol. 1&2.
103. Okajima, T.; Narioka, S.; Tanimura, S.; Hamano, K.; Kurata, T.; Uehara, Y.; Araki, T.; Ishii, H.; Ouchi, Y.; Seki, K.; Ogama, T.; Koezuka, H., NEXAFS Spectroscopic Studies of Molecular Orientation in α-Sexithienyl Evaporated Thin Films on Metal Films. *J. Electron. Spectrosc. Relat. Phenom.* **1996,** *78*, 379-382.
104. Yoshikawa, G.; Kiguchi, M.; Ikeda, S.; Saiki, K., Molecular Orientations and Adsorption Structures of α-Sexithienyl Thin Films Grown on Ag(110) and Ag(111) Surfaces. *Surf. Sci.* **2004,** *559*, 77-84.
105. Wagner, T.; Fritz, D. R.; Zeppenfeld, P., α-6T on Ag(110): The Formation of the Wetting Layer. *Synth. Met.* **2011,** *161*, 2006-2010.
106. Casado, J.; Katz, H. E.; Hernandez, V.; Navarrete, J. T. L., Infrared Spectra of Two Sexithiophenes in Neutral and Doped States: a Theoretical and Spectroscopic Study. *Vib. Spectrosc* **2002,** *30* (2), 175-189.
107. Degli Esposti, A.; Fanti, M.; Muccini, M.; Taliana, C.; Ruani, G., The Polarized Infrared and Raman Spectra of α-T6 Single Crystal: an Experimental and Theoretical Study. *J. Chem. Phys.* **2000,** *112* (13), 5957-5969.
108. Lang, P.; Horowitz, G.; Valat, P.; Garnier, F.; Wittmann, J.; Lotz, B., Spectroscopic Evidence for a Substrate Dependent Orientation of Sexithiophene Thin Films Deposited onto Oriented PTFE. *J. Phys. Chem. B* **1997,** *101* (41), 8204-8211.
109. Nyquist, R. A.; Streck, R., Infrared and Nuclear Magnetic Resonance Spectra Structure Correlations for Alkyl Acrylates and Alkyl Methacrylates in Solution. *Spectrochim. Acta, Pt. A: Mol. Biomol. Spectrosc.* **1995,** *51* (3), 475-476.
110. Lovinger, A. J.; Davis, D. D.; Ruel, R.; Torsi, L.; Dodabalapur, A.; Katz, H. E., Mophology of Alpha-Hexathienyl Thin Film Transistor Films. *J. Mater. Res.* **1995,** *10* (11), 2958-2962.

111. Ruiz, R.; Papadimitratos, A.; Mayer, A. C.; Malliaras, G. G., Thickness dependence of mobility in pentacene thin-film transistors. *Adv. Mater.* **2005,** *17* (14), 1795-+.
112. Dodabalapur, A.; Katz, H. E.; Torsi, L.; Haddon, R. C., Organic Heterostructure Field-Effect Transistors. *Science* **1995,** *269* (5230), 1560-1562.
113. Rogers, J. A.; Bao, Z.; Baldwin, K.; Dodabalapur, A.; Crone, B.; Raju, V. R.; Kuck, V.; Katz, H.; Amundson, K.; Ewing, J.; Drzaic, P., Paper-Like Electronic Displays: Large-Area Rubber-Stamped Plastic Sheets of Electronics and Microencapsulated Electrophoretic Inks. *Proceedings of the National Academy of Sciences* **2001,** *98* (9), 4835-4840.
114. Sirringhaus, H.; Kawase, T.; Friend, R. H., High-Resolution Ink-Jet Printing of All-Polymer Transistor Circuits. *MRS Bull.* **2001,** *26* (7), 539-543.
115. Seung, H. K.; Pan, H.; Grigoropoulos, C. P.; Luscombe, C. K.; Frechet, J. M. J.; Poulikakos, D., All-Inkjet-Printed Flexible Electronics Fabrication on a Polymer Substrate by Low-Temperature High-Resolution Selective Laser Sintering of Metal Nanoparticles. *Nanotechnology* **2007,** *18* (34), 1-8.
116. Crone, B. K.; Dodabalapur, A.; Sarpeshkar, R.; Filas, R. W.; Lin, Y.-Y.; Bao, Z.; O'Neill, J. H.; Li, W.; Katz, H. E., Design and Fabrication of Organic Complementary Circuits. *J. Appl. Phys.* **2001,** *89*, 5125-5132.
117. Rotzoll, R.; Mohapatra, S.; Olariu, V.; Wenz, R.; Grigas, M.; Klaus, D., Radio Frequency Rectifiers Based on Organic Thin-Film Transistors. *Appl. Phys. Lett.* **2006,** *88*, 1-3.
118. Someya, T.; Kato, Y.; Sekitani, T.; Iba, S.; Noguchi, Y.; Murase, Y.; Kawaguchi, H.; Sakurai, T., Conformable, Flexible, Large-Area Networks of Pressure and Thermal Sensors with Organic Transistor Active Matrixes. *Proc. Natl. Acad. Sci. USA* **2005,** *102* (35), 12321-12325.
119. Brown, A. R.; Pomp, A.; de Leeuw, D. M.; Klaassen, D. B. M.; Havinga, E. E.; Herwig, P.; Müllen, K., Precursor Route Pentacene Metal-Insulator-Semiconductor Field-Effect Transistors. *J. Appl. Phys.* **1996,** *79*, 2136.
120. Brown, A. R.; Pomp, A.; Hart, C. M.; De Leeuw, D. M., Logic Gates Made from Polymer Transistors and Their Use in Ring Oscillators. *Science* **1995,** *270* (5238), 972-974.
121. Bhardwaj, B. S.; Sugiyama, T.; Namba, N.; Umakoshi, T.; Uemura, T.; Sekitani, T.; Verma, P., Orientation Analysis of Pentacene Molecules in Organic Field-Effect Transistor Devices Using Polarization-Dependent Raman Spectroscopy. *Scientific Reports* **2019,** *9*, 15149.
122. Dimitrakopoulos, C. D.; Brown, A. R.; Pomp, A., Molecular Beam Deposited Thin Films of Pentacene for Organic Field Effect Transistor Applications. *J. Appl. Phys.* **1996,** *80*, 2501-2508.
123. Jurchescu, O. D.; Baas, J.; Palstra, T. T. M., Effect of Impurities on the Mobility of Single Crystal Pentacene. *Appl. Phys. Lett.* **2003,** *84*, 3061-3063.
124. Bolognesi, A.; Berliocchi, M.; Manenti, M.; Di Carlo, A.; Lugli, P.; Lmimouni, K.; Dufour, C., Effects of Grain Boundaries, Field-Dependent Mobility, and Interface Trap States on the Electrical Characteristics of Pentacene TFT. *IEEE Trans. Electron Devices* **2004,** *51* (12), 1997-2003.

125. Kagan, C. R.; Afzali, A.; Graham, T. O., Operational and Environmental Stability of Pentacene Thin-Film Transistors. *Appl. Phys. Lett.* **2005,** *86*, 193505.
126. Westermeier, C.; Cernescu, A.; Amarie, S.; Liewald, C.; Keilmann, F.; Nickel, B., Sub-Micron Phase Coexistence in Small-Molecule Organic Thin Films Revealed by Infrared Nano-Imaging. *Nature Communications* **2014,** *5*, 4101.
127. Ruiz, R.; Choudhary, D.; Nickel, B.; Toccoli, T.; Chang, K.-C.; Mayer, A. C.; Clancy, P.; Blakely, J. M.; Headrick, R. L.; Iannotta, S.; Malliaras, G. G., Pentacene Thin Film Growth. *Chem. Mater.* **2004,** *16*, 4497-4508.
128. Ruiz, R.; Nickel, B.; Koch, N.; Feldman, L. C.; Haglund Jr., R. F.; Kahn, A.; Family, F.; Scoles, G., Dynamic Scaling, Island Size Distribution, and Morphology in the Aggregation Regime of Submonolayer Pentacene Films. *Phys. Rev. Lett.* **2003,** *91* (13), 136102.
129. Farina, L.; Brillante, A.; Della Valle, R. G.; Venuti, E.; Amboage, M.; Syassen, K., Pressure-Induced Phase Transition in Pentacene. *Chem. Phys. Lett.* **2003,** *375*, 490-494.
130. Kim, D. H.; Lee, H. W.; Yang, H.; Yang, L.; Cho, K., Tunable Crystal Nanostructures of Pentacene Thin Films on Gate Dielectrics Possessing Surface-Order Control. *Adv. Funct. Mater.* **2008,** *18*, 1363-1370.
131. Lee, H. W.; Kim, D. H.; Cho, J. H.; Hwang, M.; Jang, Y.; Cho, K., Effect of the Phase States of Self-Assembled Monolayers on Pentacene Growth and Thin-Film Transistor Characteristics. *J. Am. Chem. Soc.* **2008,** *130*, 10556-10564.
132. Bouchoms, I. P. M.; Schoonveld, W. A.; Vrijmoeth, J.; Klapwijk, T. M., Morphology Identification of the Thin Film Phases of Vacuum Evaporated Pentacene on SiO_2 Substrates. *Synth. Met.* **1999,** *104*, 175-178.
133. Shioya, N.; Murdey, R.; Nakao, K.; Yoshida, H.; Koganezawa, T.; Eda, K.; Shimoaka, T.; Hasegawa, T., Alternative Face-On Thin Film Structure of Pentacene. *Scientific Reports* **2019,** *9*, 579.
134. Drummy, L. F.; Martin, D. C., Thickness-Driven Orthorhombic to Triclinic Phase Transformation in Pentacene Thin Films. *Adv. Mater.* **2005,** *17* (7), 903-907.
135. Mayer, A. C.; Kazimirov, A.; Malliaras, G. G., Dynamics of Bimodal Growth in Pentacene Thin Films. *Phys. Rev. Lett.* **2006,** *97* (10), 105503.
136. Kiguchi, M.; Nakayama, M.; Shimada, T.; Saiki, K., Electric-Field-Induced Charge Injection or Exhaustion in Organic Thin Film Transistor. *Phys. Rev. B* **2005,** *71*, 035332.
137. Jentzsch, T.; Juepner, H. J.; Brzezinka, K.-W.; Lau, A., Efficiency of Optical Second Harmonic Generation from Pentacene Films of Different Morphology and Structure. *Thin Solid Films* **1998,** *315*, 273-280.
138. Mannsfeld, S. C. B.; Virkar, A.; Reese, C.; Toney, M. F.; Bao, Z., Precise Structure of Pentacene Monolayers on Amorphous Silicon Oxide and Relation to Charge Transport. *Adv. Mater.* **2009,** *21*, 2294-2298.
139. Minakata, T.; Imai, H.; Ozaki, M.; Saco, K., Structural Studies on Highly Ordered and Highly Conductive Thin Films of Pentacene. *J. Appl. Phys.* **1992,** *72*, 5220-5225.
140. Roberson, L. B.; Kowalik, J.; Tolbert, L.; Kloc, C.; Zeis, R.; Chi, X.; Fleming, R.; Wilkins, C., Pentacene Disproportionation During Sublimation for Field-Effect Transistors. *J. Am. Chem. Soc.* **2005,** *127*, 3069-3075.

141. Maliakal, A.; Raghavachari, K.; Katz, H.; Chandross, E.; Siegrist, T., Photochemical Stability of Pentacene and a Substituted Pentacene in Solution and in Thin Films. *Chem. Mater.* **2004,** *16*, 4980-4986.
142. Salzmann, I.; Nabok, D.; Oehzelt, M.; Duhm, S.; Moser, A.; Heimel, G.; Puschnig, P.; Ambrosch-Draxl, C.; Rabe, J. P.; Koch, N., Structure Solution of the 6,13-Pentacenequinone Surface-Induced Polymorph by Combining X-ray Diffraction Reciprocal-Space Mapping and Theoretical Structure Modeling. *Cryst. Growth Des.* **2011,** *11* (2), 600-606.
143. Pople, J. A.; Scott, A. P.; Wong, M. W.; Radom, L., Scaling Factors for Obtaining Fundamental Vibrational Frequencies and Zero-Point Energies from HF/6-31G* and MP2/6-31G* Harmonic Frequencies. *Isr. J. Chem.* **1993,** *33*, 345-350.
144. Wong, M. W., Vibrational Frequency Prediction Using Density Functional Theory. *Chem. Phys. Lett.* **1996,** *256* (4-5), 391-399.
145. Scott, A. P.; Radom, L., Harmonic Vibrational Frequencies: An Evaluation of Hartree-Fock, Møller-Plesset, Quadratic Configuration Interaction, Density Functional Theory, and Semiempirical Scale Factors. *J. Phys. Chem.* **1996,** *100*, 16502-16513.
146. Salzmann, I.; Opitz, R.; Rogaschewski, S.; Rabe, J. P.; Koch, N.; Nickel, B., Phase Separation in Vacuum Codeposited Pentacene/6,13-Pentacenequinone Thin Films. *Phys. Rev. B* **2007,** *75*, 174108.
147. Salzmann, I.; Duhm, S.; Opitz, R.; Rabe, J. P.; Koch, N., Impact of Low 6,13-Pentacenequinone Concentration on Pentacene Thin Film Growth. *Appl. Phys. Lett.* **2007,** *91*, 051919.
148. Hosoi, Y.; Okamura, K.; Kimura, Y.; Ishii, H.; Niwano, M., Infrared Spectroscopy of Pentacene Thin Film on SiO_2 Surface. *Appl. Surf. Sci.* **2005,** *244*, 607-610.
149. Guo, D.; Sakamoto, K.; Miki, K.; Ikeda, S.; Saiki, K., Orientation Control of Pentacene Molecules and Transport Anisotropy of the Thin Film Transistors by Photoaligned Polyimide Film. *Appl. Phys. Lett.* **2007,** *90*, 102117.
150. Koch, N.; Vollmer, A.; Salzmann, I.; Nickel, B.; Weiss, H.; Rabe, J. P., Evidence for Temperature-Dependent Electron Band Dispersion in Pentacene. *Phys. Rev. Lett.* **2006,** *96*, 156803.
151. Kim, Y.; Jeon, D., Real Time Monitoring of Ordering in Pentacene Films During Growth by Using in-Situ Infrared Spectroscopy. *Current Applied Physics* **2017,** *17*, 972-975.
152. Nakai, I. F.; Tachioka, M.; Ugawa, A.; Ueda, T.; Watanabe, K.; Matsumoto, Y., Molecular Structure and Carrier Distributions at Semiconductor/Dielectric Interfaces in Organic Field-Effect Transistors Studied with Sum Frequency Generation Microscopy. *Appl. Phys. Lett.* **2009,** *95*, 243304.
153. Cherchneff, I.; Barker, J. R.; Tielens, A., Polycyclic Aromatic Hydrocarbon Optical Properties and Contribution to the Acceleration of Stellar Outflows. *The Astrophysical Journal* **1991,** *377*, 541-552.
154. Azam, R. M. A.; Bashar, N. M., *Ellipsometry and Polarized Light*. North Holland Publishing Co.: Amsterdam, 1977.
155. Heavens, O. S., *Optical Properties of Thin Solid Films*. Dover Publications: New York, 1965.

156. Kelly-Gorham, M. R. K.; DeVetter, B. M.; Brauer, C. S.; Cannon, B. D.; Burton, S. D.; Bliss, M.; Johnson, T. J.; Myers, T. L., Complex Refractive Index Measurements for BaF_2 and CaF_2 via Single-Angle Infrared Reflectance Spectroscopy. *Opt. Mater.* **2017,** *72*, 743-748.
157. Bonnal, T.; Belarouci, A.; Orobtchouk, R.; Prud'homme, E.; Tadier, S.; Foray, G., How to Determine the Complex Refractive Index from Infrared Reflectance Spectroscopy. *SN Applied Sciences* **2020,** *2*, 2070.
158. Ulrich, R.; Torge, R., Measurement of Thin Film Parameters with a Prism Coupler. *Appl. Opt.* **1973,** *12* (12), 2901-2908.
159. Carlie, N.; Anheier, N. C.; Qiao, H. A.; Bernacki, B.; Phillips, M. C.; Petit, L.; Musgraves, J. D.; Richardson, K., Measurement of the Refractive Index Dispersion of As_2Se_3 Bulk Glass and Thin Films Prior to and After Laser Irradiation and Annealing Using Prism Coupling in the Near- and Mid-Infrared Spectral Range. *Rev. Sci. Instrum.* **2011,** *82*, 053103.
160. Bhattacharyya, D.; Dhar, P.; Liu, Y.; Djurovich, P. I.; Thompson, M. E.; Benderskii, A. V., Vibrational Sum Frequency Generation Study of the Interference Effect on a Thin Film of 4,4'-Bis(*N*-carbazolyl)-1,1'-biphenyl (CBP) and Its Interfacial Orientation. *ACS Appl. Mater. Interfaces* **2020,** *12*, 26515-26524.
161. Cotton, D. E.; Roberts, S. T., Sensitivity of Sum Frequency Generation Experimental Conditions to Thin Film Interference Effects. *J. Chem. Phys.* **2021,** *154*, 114704.
162. Knittel, Z., *Optics of Thin Films*. Wiley: New York, 1976.
163. Reinhardt, K. A.; Kern, W., *Handbook of Silicon Wafer Cleaning Technology*. 2nd ed.; William Andrew: Norwich, NY, 2008.
164. Kim, H. S.; Choi, S. M.; Pate, B. D.; G, P. P., Effect of Film Thickness on the Columnar Packing Structures of Discotic Supramolecules in Thin Films. *ChemPhysChem* **2009,** *10*, 2642-2646.
165. Li, L.; Gao, P.; Wang, W.; Müllen, K.; Fuchs, H.; Chi, L., Growth of Ultrathin Organic Semiconductor Microstripes with Thickness Control in the Monolayer Precision. *Angewandte Communications* **2013,** *52*, 12530-12535.
166. Diao, Y.; Lenn, K. M.; Lee, W. Y.; Blood-Forsythe, M. A.; Xu, J.; Mao, Y.; Kim, Y.; Reinspach, J. A.; Park, S.; Aspuru-Guzik, A.; Xue, G.; Clancy, P.; Bao, Z.; Mannsfeld, S. C. B., Understanding Polymorphism in Organic Semiconductor Thin Films through Nanoconfinement. *J. Am. Chem. Soc.* **2014,** *136*, 17046-17057.
167. Lucarini, V. Tools for Data Analysis in Optics, Acoustics, Signal Processing. MATLAB Central File Exchange (accessed March 4 2021).
168. D'Errico, J. fminsearchbnd, fminsearchcon. MATLAB Central File Exchange (accessed March 4 2021).
169. Lagarias, J. C.; Reeds, J. A.; Wright, M. H.; Wright, P. E., Convergence Properties of the Nelder-Mead Simplex Method in Low Dimensions. *SIAM J. Optim.* **1998,** *9* (1), 112-147.
170. Wang, Y.; Irene, E. A., Consistent Refractive Index Parameters for Ultrathin SiO_2 Films. *J. Vac. Sci. Technol., B* **1999,** *18* (1), 279-282.
171. Ekhoff, J. A.; Rowlen, K. L., Effect of Interfacial Refractive Index on Optical Molecular Orientation Measurements. *Anal. Chem.* **2002,** *74* (23), 5954-5959.

172. V, B. H.; Wiggers, F. B.; Gupta, A.; Nguyen, M. D.; Aarnink, A. A. I.; de Jong, M. P.; Kovalgin, A. Y., Intitial Growth, Refractive Index, and Crystallinity of Thermal and Plasma-Enhanced Atomic Layer Deposition AlN Films. *J. Vac. Sci. Technol., A* **2014,** *33* (01A111).
173. Kasikov, A.; Aarik, J.; Mändar, H.; Moppel, M.; Pärs, M.; Uustare, T., Refractive Index Gradients in TiO_2 Thin Films Grown by Atomic Layer Deposition. *J. Phys. D: Appl. Phys.* **2006,** *39*, 54-60.
174. Kalnitsky, A.; Tay, S. P.; Ellul, J. P., Measurements and Modeling of Thin Silicon Dioxide Films on Silicon. *J. Electrochem. Soc.* **1990,** *137* (1), 234-238.
175. Chang, H. S.; Yang, H. D.; Hwang, H.; Cho, H. M.; Lee, H. J.; Moon, D. W., Measurement of the Physical and Electrical Thickness of Ultrathin Gate Oxides. *J. Vac. Sci. Technol., B* **2002,** *20* (5), 1836-1842.
176. Cho, Y. J.; Lee, Y. W.; Cho, H. M.; Lee, I. W., Ellipsometric Examination of Optical Property of the Si-SiO_2 Interface using the *s*-wave Antireflection. **1999**.
177. Chen, Y.; Jin, G., Refractive Index and Thickness Analysis of Natural SIlicon Dioxide Film Growing on Silicon with Variable-Angle Spectroscopic Ellipsometry. *Spectroscopy* **2006,** *21* (10), 26-31.
178. Mutilin, S. V.; Khasanov, T., The Refractive Index of Homogeneous SiO_2 Thin Films. *Physical Optics* **2008,** *105* (3), 461-465.
179. Rivory, J., Characterization of Inhomogenous Dielectric Films by Spectroscopic Ellipsometry. *Thin Solid Films* **1998,** *313*, 333-340.
180. Van, V. N.; Brunet-Bruneau, A.; Fisson, S.; Frigerio, J. M.; Vuye, G.; Wang, Y.; Abelés, F.; Rivory, J.; Berger, M.; Chaton, P., Determination of Refractive-Index Profiles by a Combination of Visible and Infrared Ellipsometry Measurements. **1996**.
181. Kuo, M.-L.; Poxson, D. J.; Kim, Y. S.; Mont, F. W.; Kim, J. K.; Schubert, E. F.; Lin, S.-Y., Realization of a Near-Perfect Antireflection Coating for Silicon Solar Energy Utilization. *Opt. Lett.* **2008,** *33* (21), 2527-2529.
182. Lim, K. P.; Ng, D. K. T.; Pu, J.; Toh, Y. T.; Febiana, T.; Vivek, K.; Wang, Q., Graded-Index Thin-Film Stack for Cladding and Coupling. *Appl. Opt.* **2016,** *55* (24), 6752-6756.
183. Kitamura, S.; Kanno, Y.; Watanabe, M.; Takahashi, M.; Kuroda, K.; Miyata, H., Films with Tunable Graded Refractive Index Consisting of Spontaneously Formed Mesoporous Silica Nanopinnacles. *ACS Photonics* **2014,** *1*, 47-52.
184. Lee, C.; Bae, S. Y.; Mobasser, S.; Manohara, H., A Novel Silicon Nanotips Antireflection Surface for the Micro Sun Sensor. *Nano Lett.* **2005,** *5* (12), 2438-2442.
185. Zhu, J.; Hsu, C. M.; Yu, Z.; Fan, S.; Cui, Y., Nanodome Solar Cells with Efficient Light Management and Self-Cleaning. *Nano Lett.* **2010,** *10*, 1979-1984.
186. Snyder, P. G.; Xiong, Y. M.; Woollam, J. A.; Al-Jumally, G. A.; Gagliardi, F. J., Graded Refractive Index Silicon Oxynitride Thin Film Characterized by Spectroscopic Ellipsometry. *J. Vac. Sci. Technol., A* **1998,** *10*, 1462-1466.
187. Feller, M. B.; Chen, W.; Shen, Y. R., Investigation of Surface-Induced Alignment of Liquid-Crystal Molecules by Optical Second-Harmonic Generation. *Physical Review A* **1991,** *43*, 6778-6792.
188. Eisert, F.; Dannenberger, O.; Buck, M., Molecular Orientation Determined by Second-Harmonic Generation: Self-Assembled Monolayers. *Phys. Rev. B* **1998,** *58* (16), 10860-10870.

189. Wang, J.; Paszti, Z.; Even, M. A.; Chen, Z., Interpretation of Sum Frequency Generation Vibrational Spectra of Interfacial Proteins by the Thin Film Model. *J. Phys. Chem. B* **2004,** *108*, 3625-3632.
190. McGilp, J. F.; Tang, Z.-R.; Cavanagh, M., Resonance and Local-Field Effects in the Characterization of Molecular Monolayers by Optical Second-Harmonic Generation. *Synth. Met.* **1993,** *61*, 181-184.
191. Zhang, T. G.; Zhang, C. H.; Wong, G. K., Determination of Molecular Orientation in Molecular Monolayers by Second-Harmonic Generation. *J. Opt. Soc. Am. B* **1990,** *7* (6), 902-907.
192. Munn, R. W.; Shabat, M. M., Calculation of Linear and Nonlinear Optical Response of Model Langmuir-Blodgett Films. *J. Chem. Phys.* **1993,** *99* (12), 10059-10067.
193. Zheng, D.-S.; Wang, Y.; Liu, A.-A.; Wang, H.-F., Microscopic Molecular Optics Theory of Surface Second Harmonic Generation and Sum-Frequency Generation Spectroscopy Based on the Discrete Dipole Lattice Model. *Int. Rev. Phys. Chem.* **2008,** *27* (4), 629-664.
194. Krauss, T.; Barrena, E.; Zhang, X.; Oteyza, D.; Major, J.; Dehm, V.; Wurthner, F.; Cavalcanti, L.; Dosch, H., Three-Dimensional Molecular Packing of Thin Organic Films of PTCDI-C8 Determined by Surface X-ray Diffraction. *Langmuir* **2008,** *24*, 12742-12744.